Athermal micro-ablation of transparent materials by multiphoton absorption with an amplified Nd : Yag microchip laser generating green sub-nanosecond pulses

Taghrid Mhalla

Communauté
UNIVERSITÉ Grenoble Alpes

THÈSE

Pour obtenir le grade de

DOCTEUR DE LA COMMUNAUTÉ UNIVERSITÉ GRENOBLE ALPES

Spécialité : **physique des matériaux**

Présentée par

Taghrid MHALLA

Thèse dirigée par **Patrice BALDECK**

préparée au sein du **Laboratoire LIPHY**

dans **l'École Doctorale Physique**

Micro-ablation athermique de matériaux transparents par absorption multiphotonique avec une micro-puce laser amplifiée Nd:YAG à impulsions vertes sub-nanosecondes

Thèse soutenue publiquement le **02/10/2015**

Devant le jury composé de :

M Stéphane PAROLA

Professeur à l'université Claude Bernard à Lyon (Rapporteur)

M Omar ZIANE

Professeur à l'université HOUARI Boumediene en Algérie (Rapporteur)

Mme Patricia SEGONDS

Professur ph fourier à l'université Joseph Fourier (Membre et président)

M Patrice BADECK,

Directeur de recherche au CNRS- UJF de GRENOBLE (Membre)

Université Joseph Fourier / Université Pierre Mendès France /
Université Stendhal / Université de Savoie / Grenoble INP

Remerciements

Je souhaite remercier en premier lieu mon directeur de thèse, M. **Patrice BALDECK**, pour m'avoir encadré, orienté, aidé et conseillé. Je lui suis également reconnaissant pour le temps conséquent qu'il m'a accordé, sa franchise et sa sympathie. J'ai beaucoup appris à ses côtés et je lui adresse ma gratitude pour tout cela.

J'adresse mes sincères remerciements à toutes les personnes au laboratoire LIPHY Pour leurs gentillesse et leur soutien notamment **Jacques DEROUARD, Jessie SITBON, Marc JOYEUX, Michael BETTON, Yara ABIDINE**

Je voudrais remercier les rapporteurs de cette thèse **M. Omar ZAIANE**, Professeur à l'université HOUARI Boumediene en Algerie, et **M Stéphane PAROLA** Professeur à l'université Claude Bernard à Lyon, pour l'intérêt qu'ils ont porté à mon travail.

J'associe à ces remerciements Madame **Patricia SEGONDS**, Professeur de l'Université Joseph FOURRIER, pour avoir accepté d'examiner mon travail.

Je souhaite remercier spécialement mon mari SALMAN SHAHADEH pour son soutien et sa patience tout au long de la thèse

Je dois un *grand merci* à mes chères amies Hanna, Salma, Fatenah, Manar, Igraa, Ferial, Florance, Jamila…. . Pour leur sincère amitié et confiance, et à qui je dois ma reconnaissance et mon attachement

Enfin, je remercie mes frères et sœur, ainsi que mes parents, pour leur soutien au cours de ces années et sans lesquels je n'en serais pas là aujourd'hui.

Résumé

Micro-ablation athermique de matériaux transparents par absorption multiphotonique avec une micro-puce laser amplifiéeNd:YAG à impulsions vertes sub-nanosecondes.

Les micro-puces lasersà impulsions sub-nanosecondes (technologie grenobloise) sont des alternatives intéressantes aux lasers femtosecondes pour le micro-usinage par absorption multiphotoniquedes matériaux transparents. Ces lasers peuvent facilement générer les puissances crêtes nécessaires pour déclencher l'ablation plasma de tous les matériaux, y compris les diamants, les céramiques, les plastiques, et les verres. En outre, ils sont de faibles coûts avec un design compact et robuste.

Dans cette thèse, nous avons étudié les processus d'ablation plasma et évalué les processus thermiques résiduels liés à un nouveau type de micro-puces laser amplifiée. Nous avons réalisé des expériences de micro-gravure de matériaux typiques : verres optiques borosilicates(D263 etBK7), et un thermoplastique (SBS). Une résolution submicronique de marquage a étéobtenue avec peu d'effets thermiques résiduels à la surface des verres.Des canaux microfluidiques pour capteurs optiques ont été gravés à travers des guides d'onde optiques sur substrat BK-7. Des réseaux de micro-canaux denses ont fabriqués à la surface du thermoplastique SBS avec une zone affectée par les effets thermiques limitée à quelques micromètres. Les résultats expérimentaux sont expliqués par un modèle d'ablation plasma qui prend en compte la génération d'un plasma d'électrons par absorption biphotonique et avalanche, la forte absorption laser par ce plasma d'électron, le transfert d'énergie par couplage électron-phonon avec la création et l'explosion du plasma ionique, la dynamique temporelle des températures générées et du front de fusion dans le substrat.

Abstract

Athermal micro-ablation of transparent materials by multiphoton absorption with an amplified Nd:Yag microchip laser generating green sub-nanosecond pulses

The microchip lasers with sub-nanoseconds pulses (Grenoble technology) are interesting alternatives to femtosecond lasers for micromachining transparent materials by multiphoton absorption. These lasers can easily generate peak powers needed to trigger the plasma ablation of all the materials, including diamonds, ceramics, plastics, and glasses. In addition, they are low cost with a compact and robust design.

In this thesis, we have studied the plasma ablation process, and have evaluated the residual thermal processes related to a new type of amplified laser microchip. We have realized micro-ablation of typical materials: optical borosilicate glasses (BK7 and D263), and a thermoplastic (SBS). Submicron resolution marking was obtained with few residual thermal effects on the surface of the glasses. Microfluidic channels for optical sensors have been etched through optical waveguides on BK-7 substrates. Dense microchannel networks have been made of the surface of SBS thermoplastic with an area affected by the thermal effects limited to a few micrometers. The experimental results are explained by a plasma ablation model that takes into account the generation of an electron plasma by two-photon absorption and avalanche, the high laser absorption by the electron plasma, the energy transfer by electron-phonon coupling leading to the creation and the explosion of the ion plasma, the temporal dynamics of the generated temperature and the melting front in the substrate.

Introduction

Laser micromachining is emerging as a powerful manufacturing technique with the development of micro and nanotechnologies. It exploits the beam quality, and the power of laser pulses to precisely drill, weld, cut, shape, repair, and mark all kinds of materials, even the hardest and the most fragile. Application fields include microelectronics, photovoltaic, medical devices, sensors, printing, photonics and displays.

In these days, there is a surge of needs to process transparent materials, such as thin glass sheets for touch screens, sapphire wafers for LED technology, CVD diamonds for highly resistant micromechanical parts, and high-tech plastics for bio-medical and micro fluidic devices. All these transparent materials, hard or soft, are difficult to process using traditional mechanical tools, or photo thermal effects of lasers such as CO2. Now, diode-pumped solid-state lasers that deliver well-controlled femtosecond to sub-nanosecond pulses 24H 7/7 days with minimal maintenance are increasingly used by industry to precisely micro-machine these materials.

For ultra-short pulse widths, lasers remove the material by photo-ablation, a process that directly generates a plasma explosion by breaking the atomic bonds. The absorbed energy is carried away with the ejected material without significant thermal damage. This is different from thermal ablation that occurs when using long pulses or CW lasers. In this latter case, the material is heated by the laser absorption until its vaporization temperature is reached, leaving a heat-affected zone (HAZ).

For transparent materials, the initial material absorption of ultra short pulses is generally a multi-iphoton absorption process, which can only occur at laser intensities in the TW/cm² range. Until

recently, most researches have focused on using ultra short pulses from hundred femto seconds to a few picoseconds. It has been ascertained by the laser processing community that a pulse width of 15 picoseconds would mark the frontier between the cold ablation and the thermal ablation processes. Such landmark has triggered the development of industrial-grade ultrafast lasers that are mainly based on diode-pumped femtosecond/ picosecond oscillators and amplifiers, and ultrafast fiber lasers. These ultrafast lasers have excellent processing results, but with a technology cost that is an order of magnitude larger than for diode-pumped solid-state Q-switched nanosecond lasers.

For a long time, Q-switched lasers were known to have pulse widths as long as tens of nanoseconds, leading to significant thermal side-effects during micromachining. In the late 1990's, self-Q-switched microchip lasers with sub-nanosecond pulses, resulting from their sub-millimeter cavity length, have been developed at LETI-CEA (Grenoble). For many years, they have been used for diamond marking in India, without problematic thermal effects that could have been induced from the "long-time duration" of their pulses, in comparison with the 15 ps landmark. Now, these lasers are produced in Grenoble area by Teemphotonics. Recent products, integrate an amplification stage leading to sub-nanosecond pulses with 100kW peak powers at tens of kHz. Such type of sub-nanosecond lasers were developed just before the beginning of my PhD thesis with the perspective to develop a cost effective technology for micromachining applications that need better results than with nanosecond lasers, but which cannot support the higher cost of switching to ultrafast lasers.

The goal of my thesis is to study the photo-ablation processes that are generated with this type of sub-nanosecond pulses in transparent materials. In particular, my objective is to evaluate the

thermal induced effects that are generated in two types of typical glasses (BK-7 and borosilicate), and one type of particularly thermo sensitive polymers (thermo plastic SBS)

This thesis is organized in five chapters.

The first chapter gives a state of arte of laser ablation in transparent materials with long and short pulse duration.

Chapter2 presents the mechanism that leads to laser ablation of transparent materials and the difference between thermal and non thermal laser ablation.

Chapter3 presents the experimental set-up, the properties of transparent materials studied during my thesis, and the characterization tools of ablation results.

Chapter4 presents our results of micro ablation experiments on transparent materials. It describes our general methods to characterize the ablation threshold, the ablation volume, the ablation efficiency, the debris deposition, and thermal effects.

Chapter5 presents the results analysis by the model of free electron generation and the study of thermal effects in our materials.

Chapter 6 presents a general conclusion and perspectives.

Chapter1

State of the art of micro-ablation in transparent materials by multi-photon absorption with pulse lasers

1.1 Lasers and applications

Laser is one of the greatest innovations of 20th century. The principle of laser was first established by Einstein in 1917by introducing the concept of simulated emission(A.Einstein, 1917). The first experiment of stimulated emission has been reported by Rudolf Ladenburg in 1928(R.Ladenburg, 1928). In 1960 Maiman demonstrated the first Ruby laser (Maiman, 1960). As early in 1970, lasers have been considered as tools machining for cutting, welding, marking, etc. For example, Ford was cutting auto body parts with a CO2 laser as soon as 1975. In the 1980s, commercial solid-state laser Nd: YAG laser with 1KWstarted to compete with CO2 lasers for high temperature material processing. In 1990s, the pulse laser technology matured, and started to be transferred from laboratory research to industry applications for high precision ablation and thermal laser applications.

The principal types of lasers are:

1. Solid-state laser (Ruby,Nd:YAG, …)
2. Gas lasers (He-Ne, CO2,…)
3. Liquid dye lasers
4. Semiconductor diode lasers

5. Free electron lasers

Figure 1.1shows an overview of laser applications classified in low and high power applications(1, 1991) .

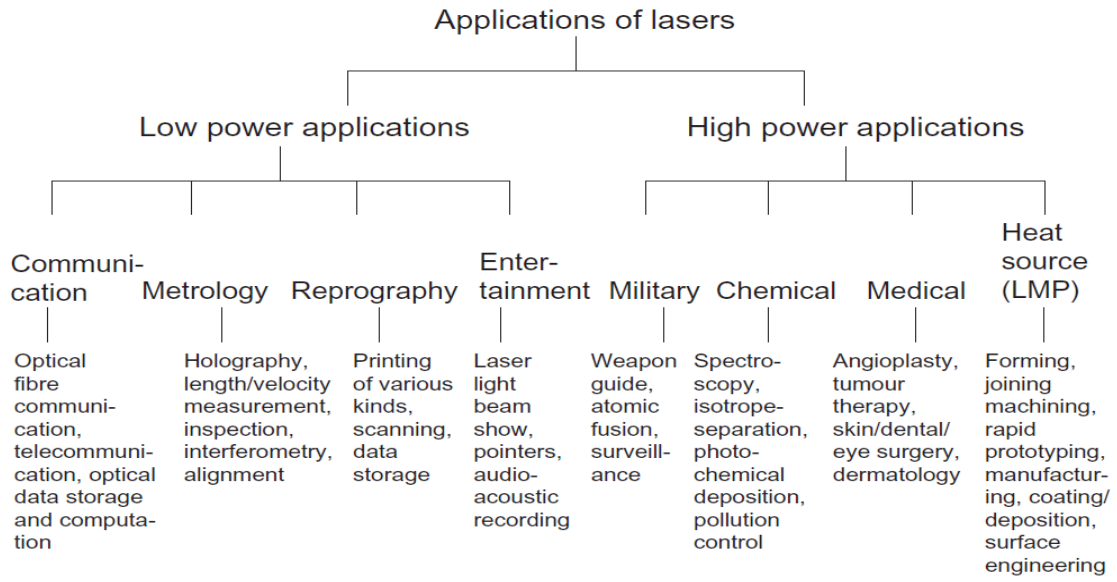

Figure 1.1: General applications of lasers(1, 1991)

1.2 Laser material processing

The early investigations of laser modification and structuration of materials started immediately after the invention of the laser in 1960. The advantages of laser machining materials are low cost, high speed, high quality, and minimum heat affected zone. Figure 1.2 shows a general classification of laser material processing. They are two principal groups. The first group target applications which require low power energy, and do not involve the changing of material state (phase). The second group required high energy to induce the phase transformation(MANNA, 2003). From the real application point of view, laser material processing can be divided into four general categories: forming, joining, machining, and surface engineering as shown in the lower half of the Figure 1.2.

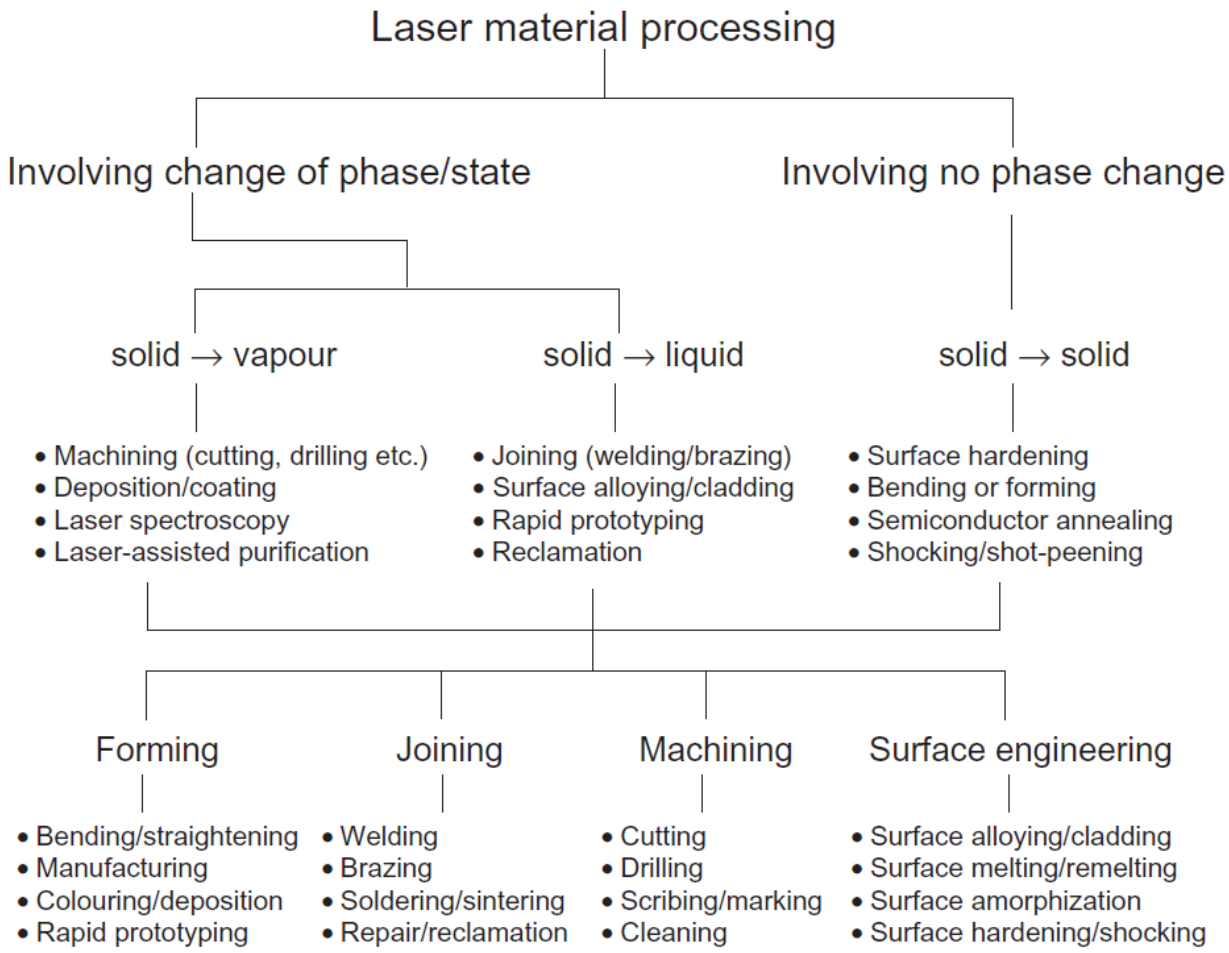

Figure 1.2: classification of laser material processing(MANNA, 2003)

1.2.1 Laser micro processing of transparent materials

In this study, we are interested in transparent materials such as glass micro–devices which have many applications in analytical chemistry, biotechnology and microelectronics. Different types of lasers are used for pattering and micromachining transparent materials. The laser is used as a powerful tool for micro- pattering and structuring of a wide of materials(D.Bauerle, 1996; J.C.Miller, 1994). Most of early studies were performed with CO2 laser by thermal melting/evaporation processes. Now, to overcome, side effects do to high temperature laser

processes, UV excimer, Nd:YAG and ultrafast laser “cold” irradiation of materials are preferred. Excimer lasers have high cost of operation and maintenance. The ultra-short pulse lasers, with Pico-second and femto-second pulse durations, have demonstrated excellent results in materials micro-processing, but until recently they had stability problems and high manufacturing costs.

1.2.1.1 CO2 laser processing of transparent materials and thermal effects

Buerhop and all in 1990(Buerhop, 1990)have observed the surface micro cracking of glasses when they have been irradiated by(TEA) CO2 and (CW) CO2 lasers using etching and dot write techniques. There are numerous studies on the thermal effects and cracking in CO2 laser irradiation of glass. For example, in 1995, Snelling and all(G. Allcock, 1995) have investigated the CO2 laser marking of soda lime and borosilicate glasses. Their results have shown the micro cracking of surfaces, because of the thermal stress induced after the laser heating (Figure1.3).

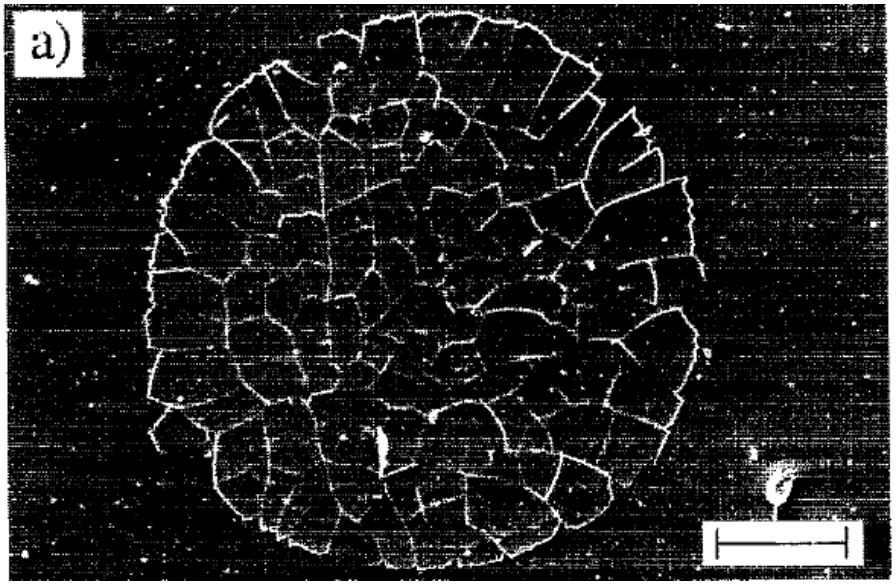

Figure 1.3:SEM micrograph of TEA CO2 laser irradiated sodalime glass at 15J/cm²(G. Allcock, 1995)

1.2.1.2 Femtosecond laser processing of materials:

Recently,femtosecond lasers haveopened a wide range of new “athermal” material processing applications. Theyare used in micro-machining of metals (S. Preuss, 1995,; K. Furusawa, 1999), semiconductors (Ihlemann, 1995; G. Herbst, 1996), in micro- processing of small and complex transparent materials for micro optic, opto-electronic, and optical fiber technology(J. Ihlemann, 1992; Kautek, et al., 1994; Kautek, 1996). The mechanism of laser matter-interaction of femtosecond lasers is different from CW of long nanosecond pulse lasers. Amplified, femtosecond pulses can easily induced high peak powers, which are enough for induced an instantaneous material ionization at the laser focus (P.S. Banks, 1999; A.V. Lugovskoy and I. Bray, 1999) . Figure 1. shows the dependence of the machining quality of fused silica with the pulse durations. Femtosecond lasers can easily, ablate materials with little or no thermal effects, but they are still very expensive to manufacture.

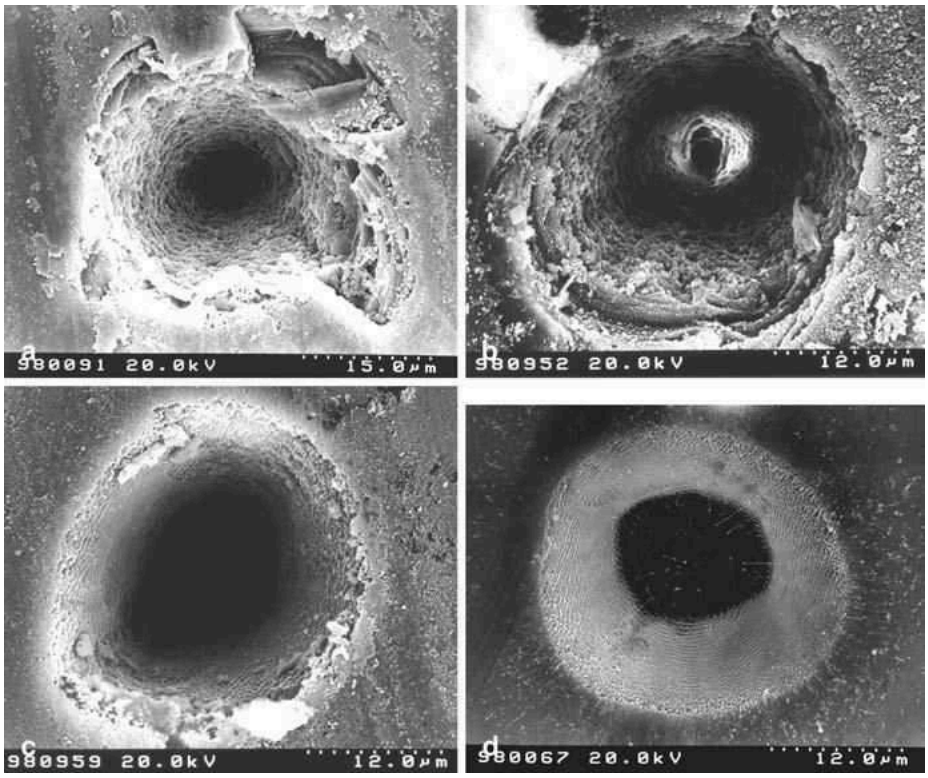

Figure 1.4: SEM micrographs of pulsed laser ablated of fused silica at 780nm, N=80 pulse atdifferents pulse duration (a) t=3ps,F=19.9J/cm²,(b) t=220fs,F=10.7, (c) t=20 fs,F=11,1 J/cm²,(d) t=5fs,F=6.9J/cm²(M. Lenzner, (1999))

1.2.1.3 The Microchip Lasers

The microchip lasers are compact solid-state diode-pumped passively Q-switched lasers with sub-nanosecond pulse duration, and multi kilowatt power at high repetition rates. In 1989 Dixon and all (G. J. Dixon, 1989) and Zayhowski and Mooradian(Mooradian, 1989)have proposed the concept of microchip laser. Figure 1.5 presents a general schematic of passive Q-switching microchip laser, generally the gain medium is Nd: YAG and the saturable absorber is Cr^{4+} : YAG.

Microchip lasers have many industrial applications such as:laser marking, environmental and medical applications, public works, and telecommunications .The main advantage of this laser is that it can be fabricated with collective fabrication processes with low cost.

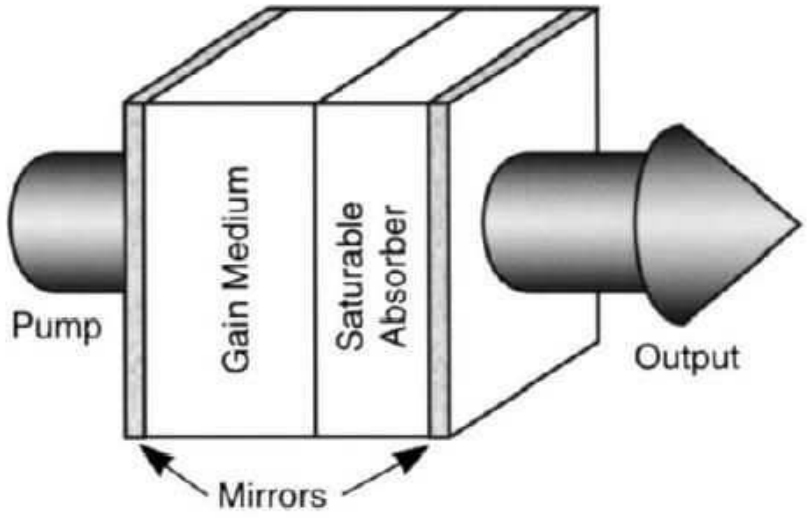

Figure 1.5:Schematic ofa passively Q-switched micro-laser system. The gain medium is usually Nd: YAG and the saturable absorber is Cr 4+: YAG(Zayhowski, 2000)

The passively Q-switched microchip laser at 1064 nm, has been used to mark different materialswith marking thresholds that are three times lower thanclassical nanosecond solid-state lasers(Molva, 1999). Figure 1.6 shows the micro-marking of lines on an aluminium plate.

igure 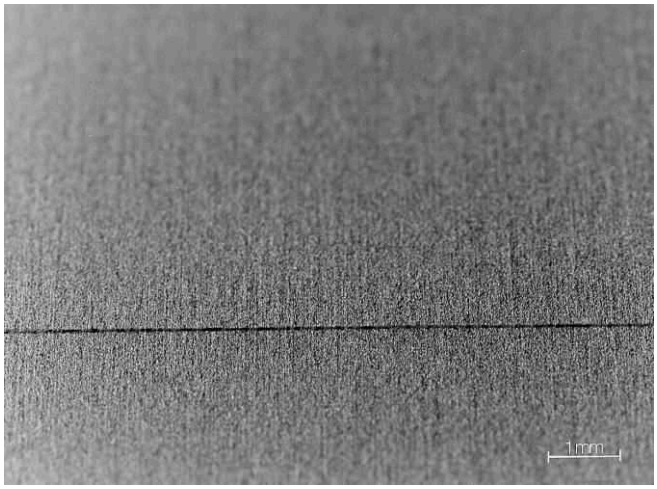

Figure 1.6: microchip laser micromarking on an aluminium plate(Molva, 1999)

Figure1.7, shows a hole drilling on copper by using a compact, and inexpensive fiber-amplified microchiplaser with a pulse duration of 100 ps, a repetition rate higher than 100 kHz, and a pulse energy up to 80 μJ. Experiments results show that the ablation rate follows the same logarithmic dependence on the incoming energy as observed for femtosecond laser experiments.The measurement of effective penetration depth, and energy thresholdsfor three materials (copper,carbon steel, andstainless steel)were foundconsistent with micromachining with sub-picosecond laser pulses.(Tünnermann, 2009)

Figure 1.7: SEM images of laser-trepanned holes on copper,(Tünnermann, 2009)

In this thesis we have used an amplified microchip laser Nd:YAG (Powerchip, Teemphotonics) at 532nm to test the micro-ablation, and thermal induced effects, of different types of transparent materials glass and thermoplastics. Such lasers are compact and low cost sub-nanosecond lasers with a 300-psec pulse duration, a pulse energy up to 40 microjoules, and a triggered repetition rate up to 1 kHz. High quality micro-size marking is demonstrated on the surface of borosilicate glass. Micro fluidic channels are engraved on BK-7 glass microchips with ion-doped waveguides. Arrays of dense micro-channels are fabricated at the surface of thermoplastics with a zone affected by thermal effects limited to the micron range.

Chapter2:
Mechanisms of laser ablation in transparent materials with pulse laser

In this chapter, we present an overview of the theoretical background for ultrafast laser ablation of transparent materials. This type of ablation process can be described in six sequential steps:

1) Multiphoton absorption and bond electron ionization (dielectric optical properties)

2) Avalanche ionization by free electron collision (from dielectric to plasma optical properties)

3) Electron plasma absorption

4) Energy transfer to ions

5) Material ejection by thermal and/or electrostatic mechanisms

6) Ablated substrate cooling

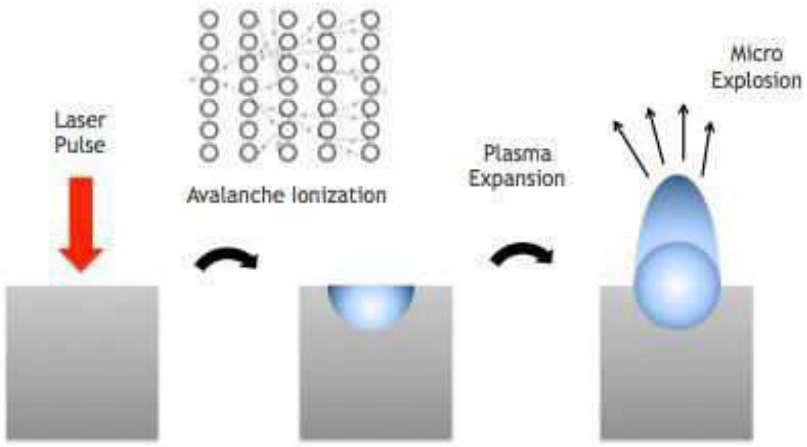

figure 2. 1: generation and expansion of plasma in pulsed laser ablation (Peatman, 2013)

1) Multiphoton absorption and bond electron ionization (dielectric optical properties)

The first step of pulse ablation for dielectric transparent materials is the multiphoton absorption and ionization of bond electrons. For materials which are transparent at visible laser radiation,

the photon energy is typically smaller than the band gap of the material. It is not sufficient to excite an electron from the valence band to conduction band, and the linear single photon absorption process cannot take place. The photon ionization of bond electrons is necessarily a multiphoton nonlinear process that can occur only if the material is exposed to high intensity laser pulses (N; Satuart BC, 1996; Lenznar M, 1998; Stoian R, 2002; DU D, 1994). The multiphoton photon energy must exceed the binding energy of electrons in the Coulomb potential of the material.

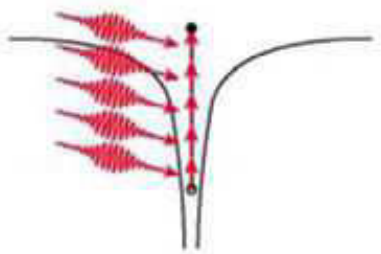

figure 2. 2 :: schematic of the photoionization mechanism by multiphoton absorption(C. B. Schaffer, 2001)

$P = \sigma I^k$ is the rate of free electron generation per unit volume and unit time in multi-photon ionization.

As the optical frequency is much larger than the tunneling frequency, the multi-photon ionization (MPI) coefficient σ is calculated from the simpler Kennedy approximation form (Kennedy, 1995; Keldysh, 1965)

$$\sigma = \frac{2w}{9\pi}\left(\frac{mw}{h}\right)^{3/2}\left(\frac{e^2}{16w^2 c\varepsilon_0 n_0 m\, Eg}\right)^k \exp(2K).\,\Phi\left[\left(2\mathrm{K} - 2\frac{\mathrm{Eg}}{\mathrm{hw}}\right)^{1/2}\right. \qquad (2, 2)$$

Where Φis the Dawson probability integral, k is the number of photons for MPI:

$$K = \left\langle \frac{Eg}{hw} + 1 \right\rangle \qquad (2, 3)$$

Eg is the energy band gap, *w, m, e* and ε_0 are the laser frequency, the effective mass of the electron and the quasi-free electron, the electron charge and the vacuum dielectric permittivity, respectively.

2) Avalanche ionization by free electron collision (from dielectric to plasma optical properties)

The second step is the electron plasma generation by avalanche ionization. Avalanche ionization involves free-carrier absorption followed by impact ionization. When free electrons are accelerated by the laser electric field, they can generate cascade free electrons by collision excitation of bond electrons (Fig. 2.3). Cascade electrons are produced with low kinetic energies, but they can get more energetic through free carried absorption until their impactscan ionize another valance band electrons. This process repeat itself. The free-electron density grows exponentially (avalanche ionization) until it reaches the critical free-electron density that characterize electron plasmas. At this step the material optical properties change from dielectric to plasma properties.

The plasma critical free-electron density can defined as $nc = mew^2/4\pi e^2$, where me is the electron mass and w is the laser frequency, this is the plasma density at which the plasma oscillation frequency equals the laser frequency, and the transparent material become totally opaque (X. Liu).

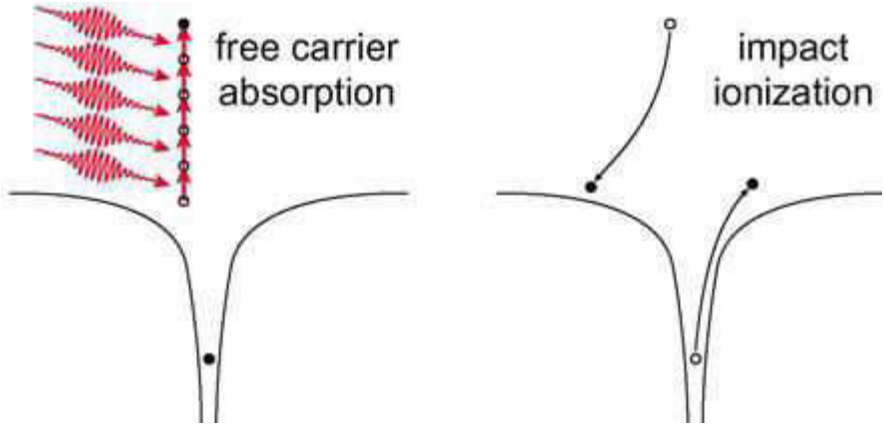

figure 2. 3 : schematic of avalanche ionization presented in reference (C. B. Schaffer, 2001)

The rate of free electrons generated per unit volume and per unit time in avalanche ionization is : **B=α_c I ρ**, where the avalanche ionization coefficient**α_c**is given by(Keldysh, 1965)

$$\alpha c = \frac{1}{w^2\zeta^2+1}\frac{e^2\zeta}{cn0\mathcal{E}0meEg} \qquad (2,4)$$

Where **ζ** = 1 fs is the electron - electron collision time

$\frac{1}{w^2\zeta^2+1}\frac{e^2\zeta}{cn_0\mathcal{E}_0 m_e} I_0$presents the rate of electron energy gain.

3) Electron plasma absorption

During plasma generation at the laser focus, the material optical properties change from dielectric to metallic. In particular, from transparent it becomes to be highly reflective and absorbing. Most of the incident energy is absorbed during this transition. The absorption properties (total absorbed energy and absorption depth) can be calculated from the Drude approximation for the dielectric function of plasma:

$$\mathcal{E} = 1 - \frac{{w_p}^2}{w^2+{v_{eff}}^2} + i\,\frac{{w_p}^2}{w^2+{v_{eff}}^2}\frac{v_{eff}}{w} = \mathcal{E}' + \mathcal{E}'' \qquad (2,5)$$

Where the plasma frequency is given by

$${w_p}^2 = \frac{4\pi e^2 n_e}{m*} \qquad (2,6)$$

4) Energy transfer to ion lattice, plasma expansion and material ejection

Once the laser energy has been absorbed by the free-electron plasma, it is transferred to ion lattice with atypical electron-photon coupling time of a few picoseconds. Then, there is an electron/ions plasma expansion that ejects the hot temperature material to let an ablation crater.

2.1 Time dynamics of ablation processes with ultra-short (100 fs) pulses:

Figure 2.4 shows the timescale and intensity ranges of phenomena and processes occurring during and after irradiation of a solid with pulsed laser of 100fs of pulse duration. Excitation of the solid occurs during the laser pulse, the melting occurs on a range of a few picoseconds to ten of picoseconds, and expansion and ablation of the material takes place of several nanoseconds.

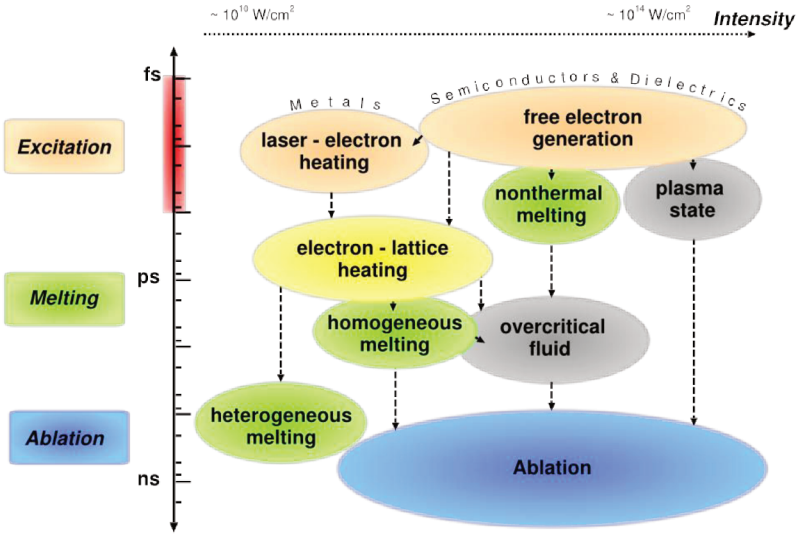

figure 2. 4 : typical timescale of ablation steps with 100 fs pulses (b. rethfeld1, 2004)

2.2 Ablation without or with thermal side effects depending on the pulse intensity(and time duration)

Ablation can occur by different processes than depend mainly on the peak pulse intensity at the laser focus:

1) In the range of 10^{14} W/cm², ionized atoms have enough energy to break their bonds (Coulomb explosion). There is an ultrafast explosion of anelectrons/ions plasma without any thermal transfer to the surrounding lattice.

2) In the 10^{12} W/cm², the electron plasma energy is transferred to the ion lattice in a few picoseconds creating the ion plasma (no thermal melting). The plasma expansion, in tens to hundreds picoseconds, lead to an ablation process without thermal side effects.

3) In the 10^{10} W/cm², below the threshold for avalanche ionization, the energy of hot electrons is gradually used to heat the ion lattice until melting, and evaporation. With long pulses (> tens of nanoseconds), this process time can be long enough to allow heat diffusion out of the focal point, and to affect the material properties.

In practice, the available intensity range depends on the laser pulse duration: 10^{14} W/cm² with femtosecond lasers, 10^{12} W/cm², with picosecond lasers, and 10^{10} W/cm² with nanosecond lasers. Thus, femtosecond and a-few picosecond pulses (ultrafast pulses) are used for non thermal ablation and nanosecond pulses are known to generate ablation with thermal effects.

Figure 2.5 compare the ablation properties that are obtained by ultrafast and long pulses, respectively. Clearly, ultrafast pulses lead to an ultraclean process, but with an expansive technology. However, thermal effects induced by long pulses leads to a more dirty process (heat affected zone, micro-cracks, surface ripples and redeposition debris), but at a much lower technology cost.

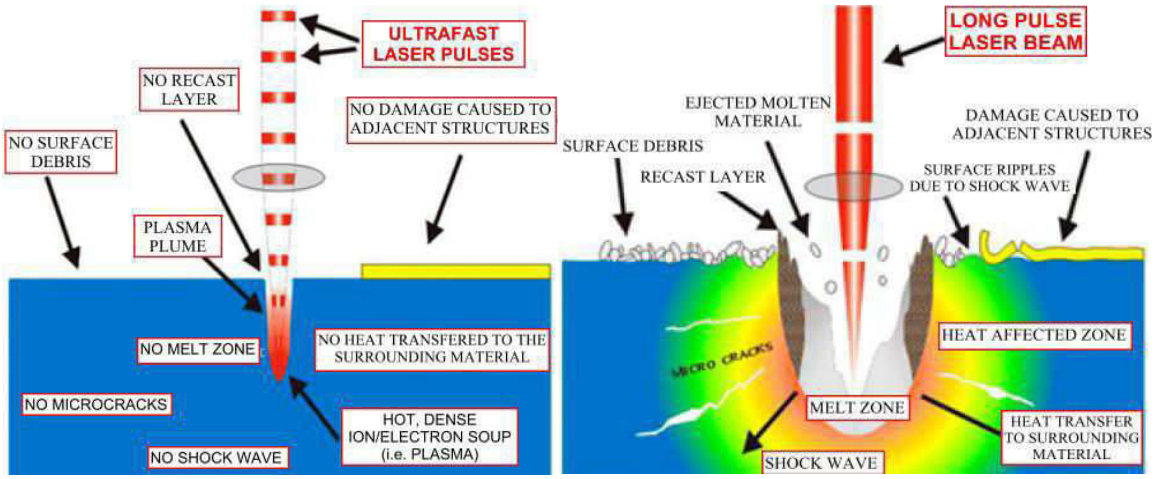

figure 2. 5:comparison of ablation properties with ultrashort pulses (left) and long pulses (right)(2010)

2.3 The methods used to characterize the ablation parameters

The characterization of laser ablation parameters comes from analyzing, the morphology of the marks generated on surfaces during laser ablation: thickness of molten layer, the melt lifetime, debris deposition, and determination of the ablation threshold, ablation volume and ablation efficiency en function of la pulse laser energies.

2.3.1 The laser ablation threshold

When a laser beam is focalized at the surface of a material, there is ablation only at locations for which the laser fluence is larger than the threshold fluence (Fig.2.6).

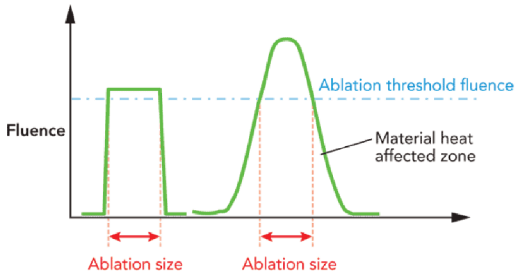

figure 2. 6 : schematic of ablation size depending on the ablation threshold fluence

Assuming a Gaussian beam profile, the relation between the crater diameter D and the threshold laser fluence can be written as (JM, 1982):

$$D^2 = 2w^2 \ln\left(\frac{F_0}{F_{th}}\right) \quad (2.7)$$

Equations are also similar for the pulse energies E_0 and E_{th}, and the laser intensities I and I_{th}:

$$D^2 = 2w^2 \ln\left(\frac{E_0}{E_{th}}\right) \quad (2.8)$$

$$D^2 = 2w^2 \ln\left(\frac{I_0}{I_{th}}\right) \quad (2.9)$$

In order to determine the ablation threshold of material, we have measured the crater diameter *D* of single–shot ablated craters for different pulse laser energies using AFM microscopy and then fitting the experimental data to the equation (2.8).

According to this equation an ablation of threshold energy E_{th} is obtained from a semi-logarithmic plot of the squared diameter of the ablated area D^2 vs pulse energy E.

2.3.2 Melt depth and melt life time .

For sub-nanosecond pulses, there is a little heat deposition in the material that is not ablated, which creates a heat affected zone that we target to evaluate in the thesis. Numerical simulations (F. Vidal, 2001) of the fluid and thermal dynamics of laser induced plasma on an aluminum target irradiated with 100 ps laser pulse shows that 70% of the absorbed energy is used by the expanding plasma to move the ambient gas. 20% of the absorbed energy is lost as radiation to the environment, ultimately leaving less than about 10% of the incident laser energy as heat inside the material. This thermal energy causes a thin layer of molten material to be formed immediately beneath the ablation crater.

We can calculate the average melting depth $h_m$from (A. Ben − Yakar, 2003):

$$hm = \frac{F}{T_m \rho C_p} \tag{2.10}$$

The lifetime of the molten layer (including both the melting and solidification processes time) depends on how quickly the energy gets dissipated into the bulk. This depends on the material thermal properties (thermal conductivity, specific heat, and density).One can estimate that the thick layer remains molten for about t (lifetime)

$$t_{(liftime)} = h_m{}^2/D \tag{2.11}$$

Where D is the thermal diffusivity,$D = K/\rho Cp$, k is the thermal conductivity, ρ is the density, C_p is the specific heat .

2.3.3 The rim formation:

During the melt lifetime there are two forces acting on the ablated surface to move the molten material from the center of crater to the edge, depositing a thin rim around the ablated area. The two forces that affect the surface of the molten layer are: 1) thermocapillary forces (Marangoni

flow)(T. Schwarz- Selinger, 1999), and 2) hydrodynamic forces exerted by the plasma above the surface(Vladimir N, 1999). Ben-Yakar et al (A. Ben-Yakar, 2003) show that the effect of the thermocapillary flow is negligible during a laser ablation of borosilicate glass, thus the melt flow in the borosilicate glass sample is caused principally by hydrodynamic forces due to the pressure gradient caused by the hot plasma sitting over the melt. The pressure gradient is extremely high at the edges of the ablated crater at the plasma/air interface. This results in some of the molten glass being ejected out of the crater over the edges of the crater. Rapid solidification results in the formation of a high rim surrounding the crater. The molten layer at the edge of the crater faces an extremely high pressure gradient at the interface between the plasma and air. This pressure difference pushes the melt over the crater surface very rapidly. The pressure driven flow time τ_p thus determines the elevation of the melt above the surface, or in other words, this time duration determines the height of the rim. The characteristic time scale for this pressure-driven melt flow is:

$$\tau_p \simeq \frac{\mu L^2}{P_0 h^2 m} \tag{2.12}$$

Where hm is the average melt depth, $P0$ is the average plasma pressure, μ is the viscosity, L is the craters width.

From the characteristic time scale, we can identify the parameters that effect the rim formation as the melt thickness,

Thus the rim height $\simeq \frac{P_0 h^2 m}{\mu L^2}$ (2.13)

Chapter 3
Experimental set-up and procedures:

In this chapter, we present the experimental set-up, the properties of transparent materials studied during the thesis, and the instruments that we have used to generate ablation and to characterize the results.

The micro-ablation set-up has been realized with a Nd:YAG microchip laser, generating green sub-ns pulses, coupled with an optical microscope. We have studied three materials: two glasses materials (D263borosilicate, and BK7 borosilicate), and a thermoplastic. The optical microscope was also used to inspect in real time the irradiated regions. A more detailed characterization of morphological changes was done with a scanning electron microscopy (SEM), and an atomic force microscope (AFM).

3.1 Experiment set up of micro-ablation:

The experiment set up is based on a Zeiss inverted microscop Axiovert 200M as shown in Fig.3.1. In this setup, a pulsed microchip laser Nd:YAG at 532 nm is used. The laser power is controlled by an acoustic optical modulator. The pulse energy is measured with a power meter. The pulse repetition rate (0-1KHz) is controlled by a TTL signal generator. The sample is fixed on a XYZ nano-positioning stage controlled by a computer. The desired structures are programmed using two in-house C++ softwares named “Simpoly”, and “single pulse test”.

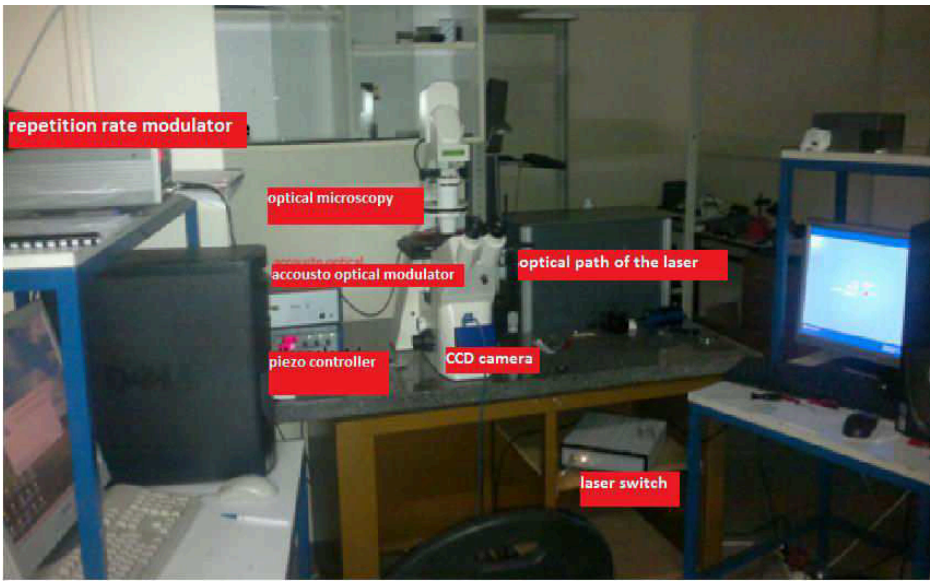

Figure 3.1:photograph ofthe main components of the micromachining system used in this study.

Figure 3.2 represents the schematic of the micro-ablation set–up based on an inverted microscope Zeiss Axiovert 200M.The Gaussian laser beam is expanded with a telescope to overfill (80% transmission) the objective pupil. The mirror pair aligns the laser beam with the microscope optics. The dichroic mirror is used to direct the laser on to the objective, and to collectmicro-ablation photoswith the camera.

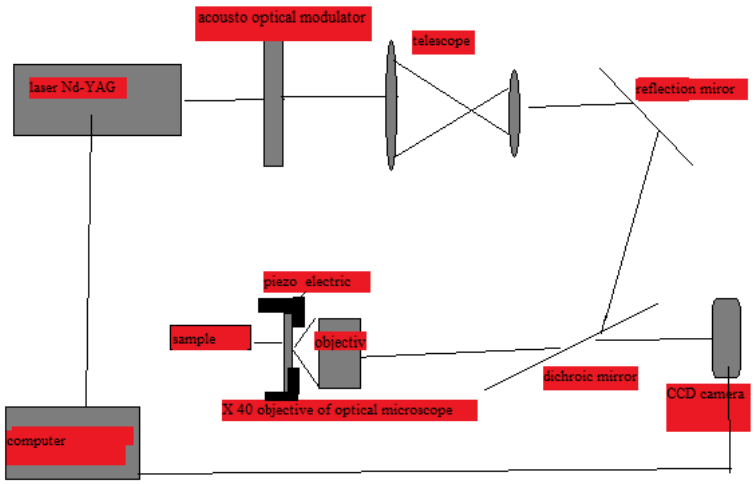

Figure 3. 2 schematic representation the micro ablation set –up

3.1.1 The microchip laser

The laser used in this thesis is an amplified passively Q-switched Nd:YAG laser, model Powerchip PNG-M of Teem Photonics France (Figure 3.1). Powerchip lasers generatesub-nanosecond pulses with high peak powers, and excellent beam quality.

The laser pulse characteristics are listed in Table 3.1.

Laser model	PNG-M02010
wavelength	532 nm
Repetition rate	1000Hz
Pulse energy	>20µJ
Short term pulse to pulse stability	<3% (1min,1σ)
Average power at max repetition rate	>20 Mw
Long term stability	<3% (6h)
Pulse duration	400 ps
Peak power	> 50KW
Polarization ratio	>100:1
Beam spatial mode	Gaussian TEM00
M^2	≤1.3
Beam roundness	≤1.3
Beam waist location	14±5 mm
Optical axis height	134 mm
Beam angular tolerance	±5 mrad

Table 3.1: characteristics of Powerchip laser used for ablation experiments

Figure 3.3:Q-Switched Nd: YAG Powerchip laser (PNG–M series).

This type of laser is commercialized by Teem Photonics for applications such as:

- Material processing
- Microdissection
- Laser induced fluorescence(LIF)
- Time Resolved Fluorescence
- Laser Induced Breakdown spectroscopy(LIBS)
- Light Detection and Ranging (LIDAR)

3.1.2 Power Meter

We have measured the laser average power with a Thorlabs PM100D power meter(figure 3.4). The curve Fig. 3.5 shows the calibration of the laser power (in mW) obtained at the output of the objective X 40 as a function of the acousto-optical modulator voltage (in volt).

Figure 3.4: compact power and energy meter

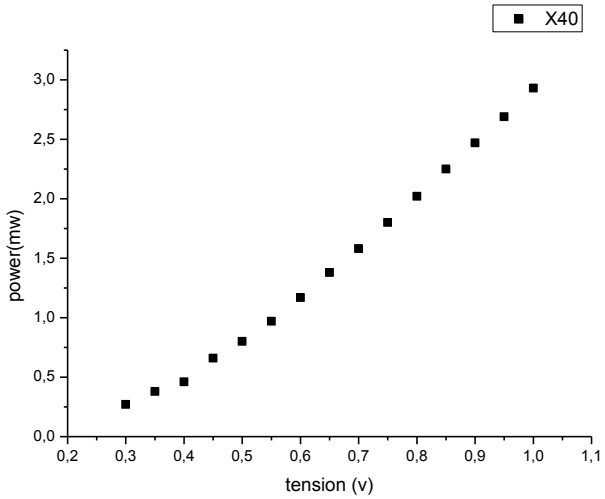

Figure 3.5: calibration curve of power at the microscope objective output as a function of the voltage applied on the acousto-optical modulator.

3.1.3 XYZ piezo stage

The sample movement during the micro-ablation process is generated with a piezo-positionnerP-611.3S Nano Cube XYZ from Physics Instrument (Figure 3.6). Is has a100x100x100 µm travel with a closed-loop resolution of 1 nm. It is driven with a bench-top amplifier and position servo-controller (E-664).

Figure 3. 6PI 611-3 piezoelectric nanocube and its E – 664 Controller

3.1.4 Softwares

The micro-ablation system is controlled by two softwares ("Simpoly" and "single pulse testing"). The software "Simpoly" can control the exposure time, laser power, and the geometry of structures as shown in Fig. 3.7. The "single pulse testing" softwarecan also control directly the number of pulses, and the time delay between pulses (Figure 3.8).

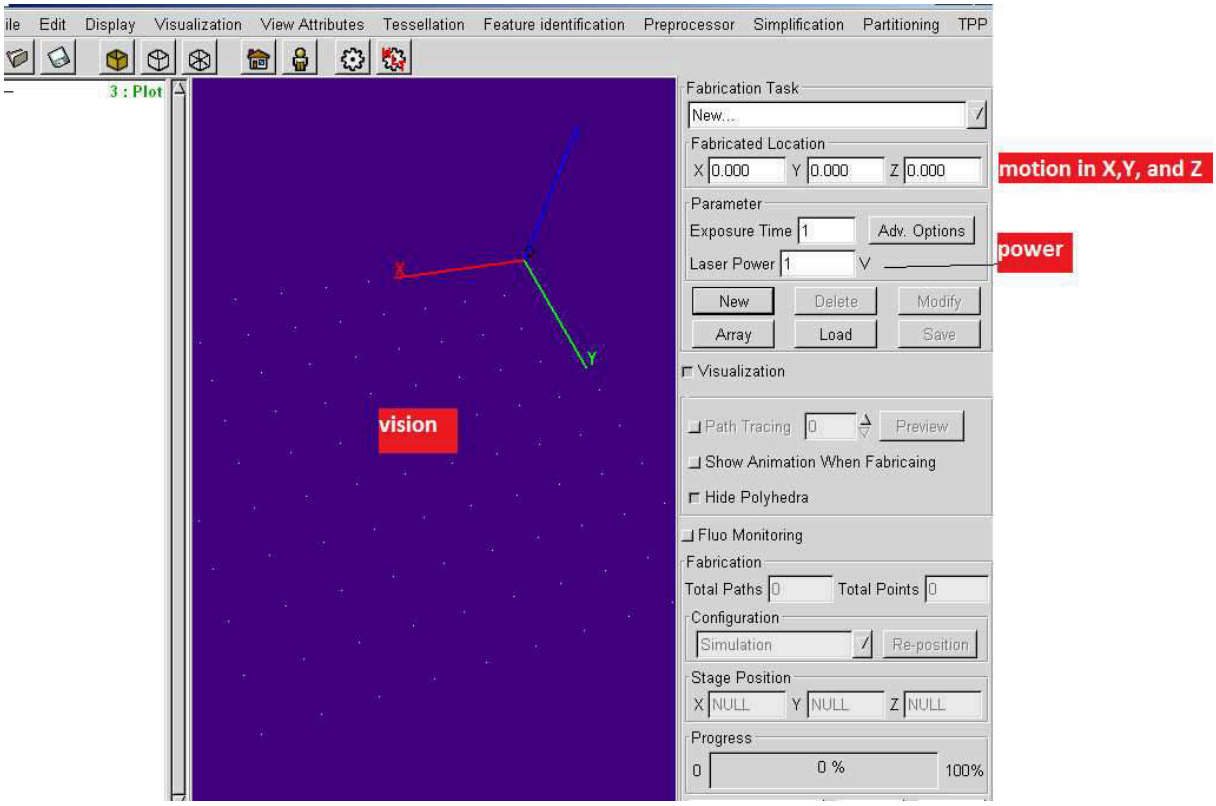

Figure 3. 7 image of software of microblation (simply)

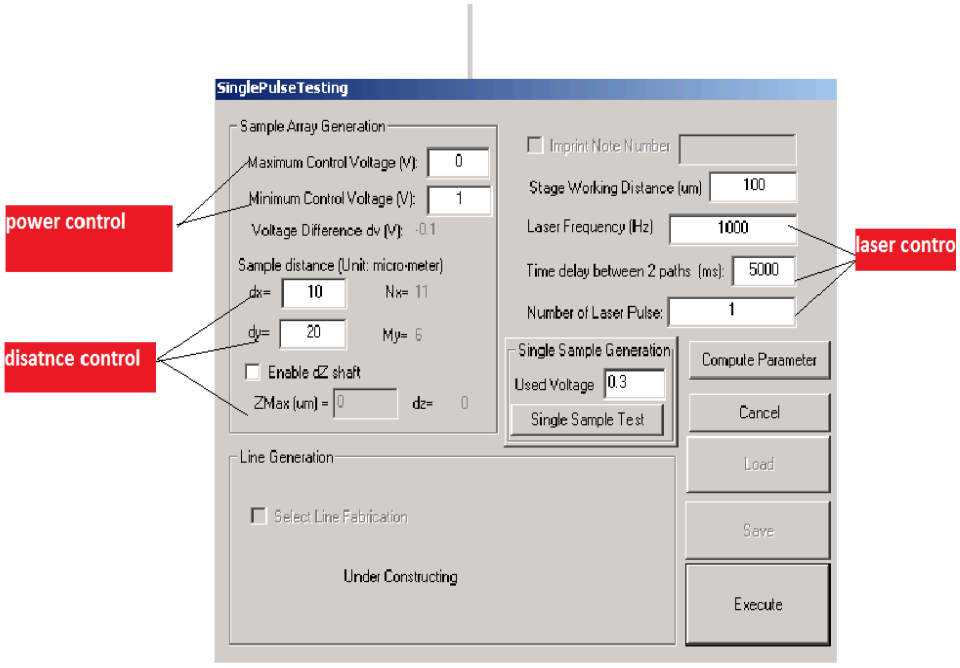

Figure 3. 8 image of software of micro-ablation (single pulse testing).

3.2 Properties of laser focalization

In this study, we have used the software "PSF lab" to estimate the laser spot characteristics at focus. For this calculation, we used the typical parameters of our experiments:

- Numerical aperture of the objective NA=0.65
- The cover slip (borosilicate D263 glass) has a thickness of 170 µm and its refractive index is 1.1515
- The laser wavelength is 532 nm
- The parameter β_G is the expanded beam transmission through the objective pupil. $\beta_{G=}0.5$
- The focused depth is 0 (at the ample surface)

The laser intensity distribution at the focal point is shown in Figure 3.10.The FWHM sizes of the beam are 0.455, and 3.29µm in x, and z directions, respectively.

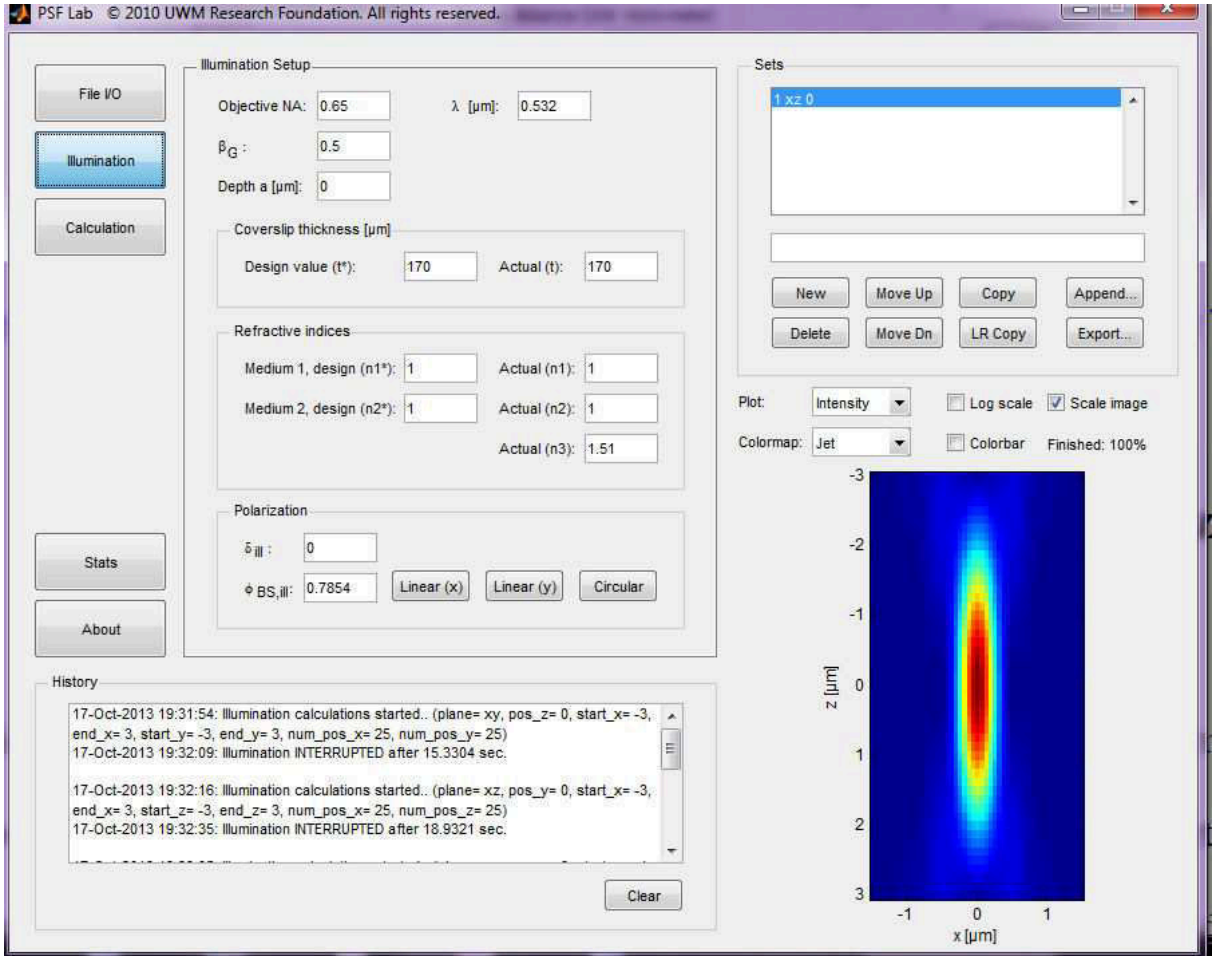

Figure 3. 9 Parameters used with "PSF lab" to calculate intensity distributions at focus.

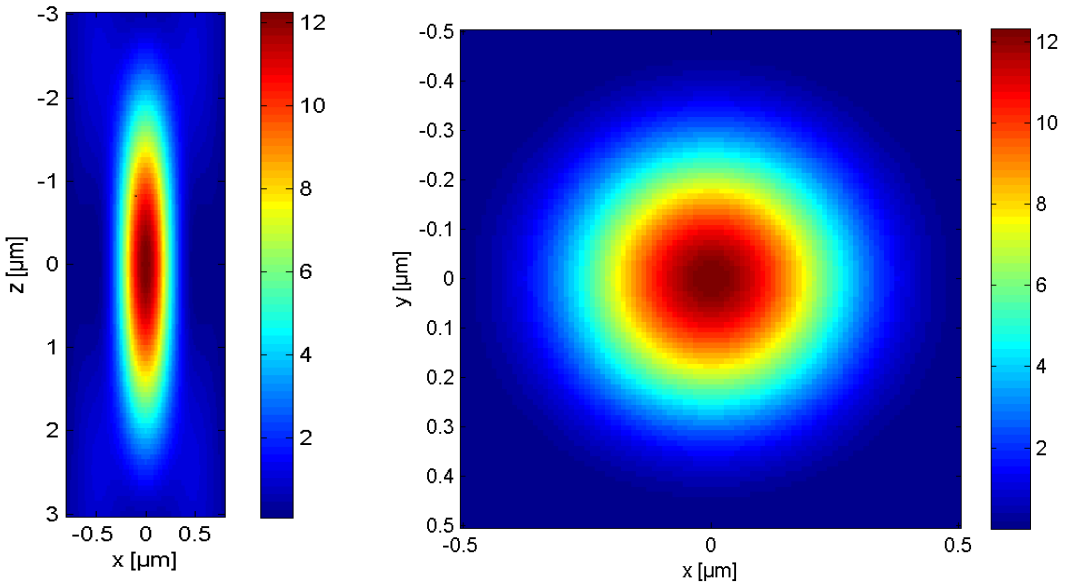

Figure 3. 10 The intensity distribution at focus calculated with the PSF Lab

The table 3.2 shows the calculation of focal area and volume, and the laser intensity pulse energy of 0.48µJ/pulse.

Symbole	Parameter	unit	value
τ_p	pulse width	ps	400
λ	wavelength	nm	532
n (D263,BK7)	refractive index	-	1.51,1.52
NA	numerical aperture	-	0.65
hv	Single photon energy at 532 nm	eV	2.33
FWHM (z)	Spot full width at half maximum along z axis	µm	3.288
FWHM (x)	Spot full width at half maximum along z axis	µm	0.444
$2W_0 = 1.699FWHM$	the full width of the beam at $1/e^2$	µm	0.754

			W_0=0.37
V_{foc}	The volume focal	µm^3	1.37
S_{foc}	The focal spot area	µm²	0.446
***I** (0.48µJ)*	The intensity results of the spot area for 0.446µm² at energy of 0.48µJ/pulse	w/cm²	0.7x10^{12}

Table 3.2:characteristics of laser spot at focus calculated with "PSF lab"

3.3 Materials properties

In this thesis, we have studied ablation of transparent materials. The laser radiation could not be absorbed by a linear single-photon-process; because of the band gap energies were larger than the photon energy. For example, the band gap of borosilicate glasses (BK7 and D263) is 4.7eV, and a two-photon excitation is needed when using a laser radiation at 532nm of 2.33 eV.

3.3.1 BK7 glass:

BK7 is a borosilicate optical glass. Its good physical and chemical properties make it widely used in visible and near IR range. Most of windows, lenses and prisms, which are used in lasers, and optical systems are made from BK7 glass. BK7 is used whenever the additional benefits of fused silica are not required. It is a relatively hard material with extremely low bubble and inclusion content, while providing excellent transmittance through-out the visible and near infrared spectra and down to 350 nm in the ultraviolet. The physical, chemical, thermal and mechanical properties of BK7 glass are listed in detail in Table 3.2.

Softening Point(°C)	**Density (g/cm^3)**	**Young's modulus**	**Thermal expansion coeff.**

		$E(10^3$ N/mm²)	10^{-6}/K	
615	2.51	82	7.1	

Composition

SiO_2	B_2O_3	BaO	Na_2O	K_2O
70%	11.5%	1.5%	9.5%	7.5%

Tableau 3.1: Physical, chemical, thermal, and chemical properties of BK7 glass

3.3.2 Borosilicate glass Schott D263 (KNITTEL Germany), i.e. microscope cover slips of 170µm thickness:

This glass is made of a colourless borosilicate glass with an optimum hydrolytic resistance. ThisD 263 cover slip is a low alkali borosilicate glass, which is produced by melting the purest raw materials. As such, it is very resistant to chemical attack. D 263 can be produced with a large range of different thicknesses with tight tolerances. It is for applications including: liquid crystal displays, optoelectronics, touch control panels, sensors, electroluminescent displays and solar cells. The thermal, mechanical, electrical and optical properties of the D263 Borosilicate glass are shown in Tableau 3.3, and Table 3.4 shows its chemical compositions.

Properties	Values
Density ρ(g/cm^3)	2.51
Specific heat c(J/gk) 20~100°C	0.82
Thermal conductivity K(J/s.cm.K)	0.0096
Thermal diffusivity α=K/Cρ (cm²/s)	0.0046

Coefficient of thermal expansion $\alpha_{(20\text{-}300°C)}$ in $10^{-6}\ K^{-1}$	7.2	
Melting temperature θ_m (°C)	1051	
Strain point ,temperature(°C) ,Viscosity log Ƞ [dPas]	529	14.5
Annealing point, temperature (°C) ,Viscosity log Ƞ [dPas]	557	13
Softening point, temperature (°C) ,Viscosity log Ƞ [dPas]	736	7.6
Young's modulusKN/mm²	72,9	
Poisson's Ratio	0.208	
Torsion Modulus (kN/mm ²)	30.1	
Knoop hardness HK_{100}	590	
Dielectric constant ε_r at 1 MHz	6.7	
Dielectrical loss factor tan δ at 1 MHz	$61 \cdot 10^{-4}$	
Refractive indicies n_e (λ = 546.1nm) , n_D (λ = 589.3nm):	1.525	1.523

Table 3.3 thermal properties of D263 borosilicate glass

SiO_2	BB_2O_3	AL_2O_3	Na_2O	K_2O	TiO_2	ZnO	Sb_2O_3
64.1%	88.4%	4.2%	6.4%	6.9%	4.0%	5.9%	0.1%

Table 3.4: the chemical composition of D263 borosilicate glass

3.3.3 SBS thermoplastic elastomers.

These thermoplastic elastomers are made up of a short chain of polystyrene, followed by a long chain of polybutadien, followed by another short chain of polystyrene Styrene-butadiene-styrene. Their block-copolymer structure combines the properties of hard-segment polystyrene blocks and the soft –segment polybutadiene blocks, resulting in ease of processing and excellent performance characteristics, the typical properties of SBS are listed in the Table 3.5.

Properties	Value
specific gravity at 73°F	0.908 to 1.11 g/cm^3
Density (200°C/5.0Kg)	0.0 to 21g/10min
Solution viscosity	400 to 4320 mPa.s
tensile strength,yield,73°F	624 to 3980 psi
Tensile elongation break 73°F	36 to770 psi
Tensile stress,73°F	102 to 355 psi
Durometer Hardness,73°F	40-76

Table 3.5: physical, and elastomers properties of SBS thermoplastic

3.4 Instruments used to characterize the ablation zone.

Various instruments were used for determining the topographical and morphological data of ablation results. Following laser processing, the sample ablation craters were systematically observed with an optical microscope (Zeiss Axiovert 200M). Some of the craters were also observed with a Scanning Electron Microscope (SEM), and an AFM microscope.

3.4.1 The optical microscope.

The micro-ablation process was realized by using a Zeiss Axiovert 200M inverted microscope. We have also used this microscope to measure the diameter of features fabricated by laser ablation of used materials. Figure 3.11shows a photo of the microscope set-up.

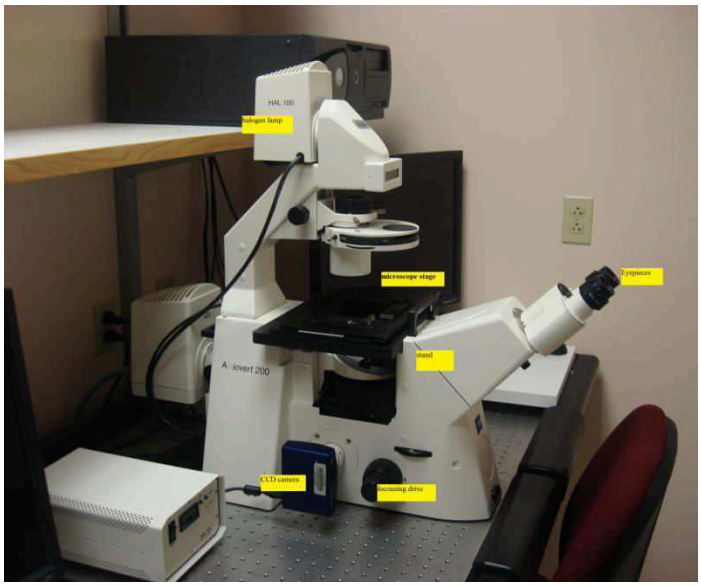

Figure 3. 11 image of a Zeiss Axiovert 200M inverted microscope

3.4.2 Scanning electron microscope.

A scanning electron microscope (SEM) is a type of electron microscope that images a sample by scanning it with a high-energy beam of electrons in a raster scan pattern. The electrons interact with the atoms that make up the sample producing signals that contain information about the sample's surface topography, composition, and other properties such as electrical conductivity. During the thesis, some of morphological data were performed with a scanning electron microscope *Zeiss -ULTRA plus* operating at about 1 kV accelerating voltage.(Fig. 3.12)

Figure 3.12.SEM microscope

3.4.3 3.4.2 AFM microscopy.

The crater morphology (diameter, depth, rim, and presence of debris) was studied in detail by using an Atomic Force Microscope (AFM) (JPK Instrument,nanowizerd Berlin) equipped with an inverted microscope (Zeiss, model D1, Berlin) for visualization as shown in Figure 3.12. All AFM topographic images are collected in the contact mode with a typical resonant frequency of 130 Hz.

Figure 3.13: image of AFM microscope

Chapter4
Experimental characterization of the short pulsed laser ablation of transparent materials:

This chapter presents our results of micro-ablation experiments on transparent materials. We report on the thesis results of laser ablation on D263 borosilicate glass, BK7 glass, and SBS thermoplastic with a green sub-nanosecond pulse laser.

4.1 Ablation of craters and lines at the surface of D263 borosilicate glass

In these experiments, we study the ablation of craters on the surface of borosilicate glass by single pulse irradiation with increasing energy.

4.1.1 Morphologies of ablation craters:

Figure 4.1. Shows a typical transmission image by optical microscopy of craters obtained by single shot irradiation with increasing energy from 1 to 3 micro-joules.

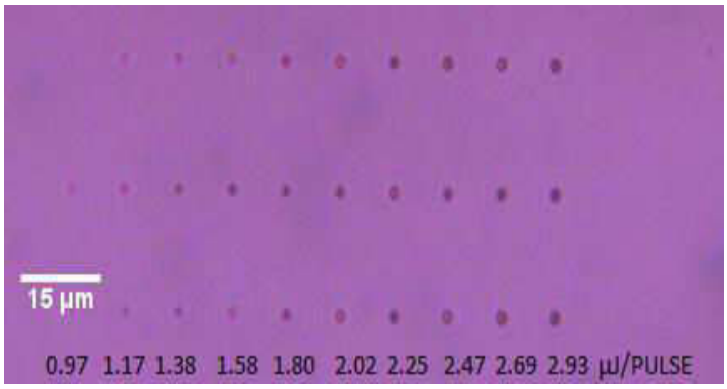

Figure 4.1: optical microscopy images of cratersobtained by single pulse ablationat the surface of D263 borosilicate glass for increasing pulse energy (same energy in the same Colum).

Scanning electron micrographs of ablation craters are shown on Fig. 4.2. Energy of 0.93 µJ was necessary to obtain the first craters. They are micron-size surrounded by a sub-micron rim that becomes important at 2.25 µJ until explosion at 2.9 µJ. We can distinguish a micron size heat affected ring for the lowest ablation energy. We can also observed projection debris on the surface

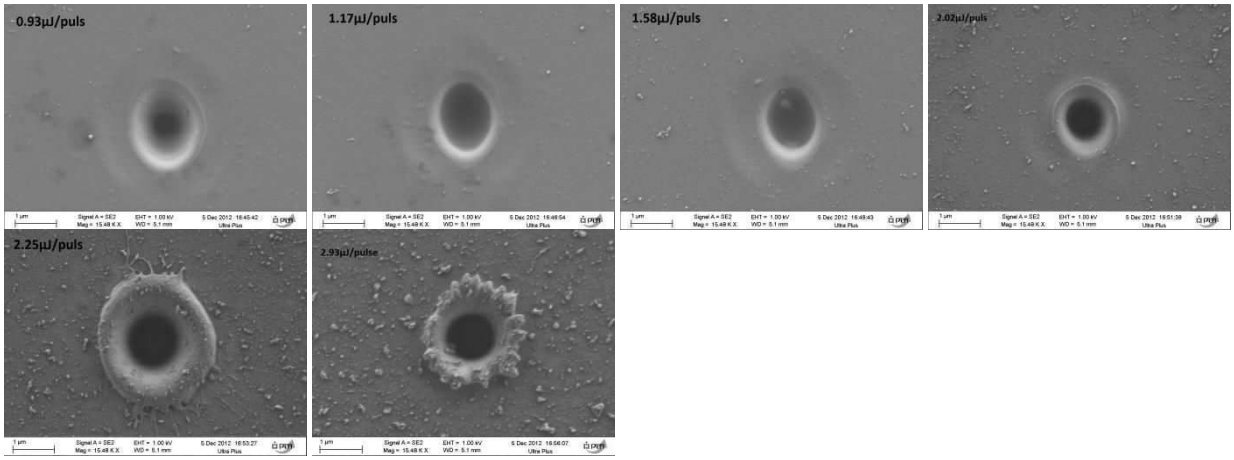

Figure 4.2 scanning electron micrographs of D263 borosilicate glass ablated by sub ns microchip laser at different pulse energies

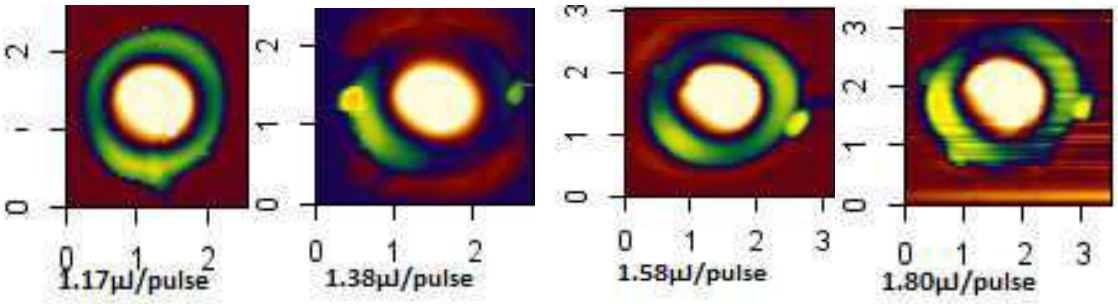

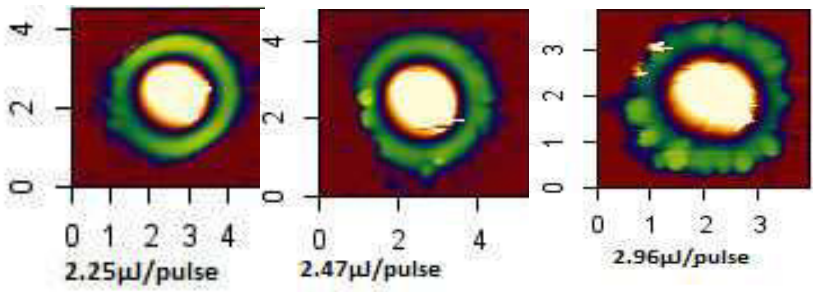

Figure 4.3 AFM images of D263 borosilicate glass ablated by sub ns microchip laser at different pulse energies

Quantitative characteristics of craters are obtained from AFM images (Fig. 4.4). Figure 4.5 shows the crater profile evolution with increasing the ablation energy. The profile asymmetry is an artifact resulting from the from the cantilever tip geometry as illustrated in Fig.4.6.

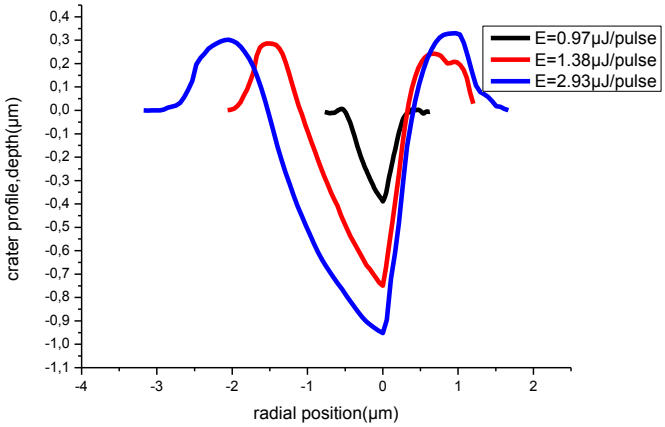

Figure 4.4 Profiles of single-shot ablation craters measured with an atomic force microscope.

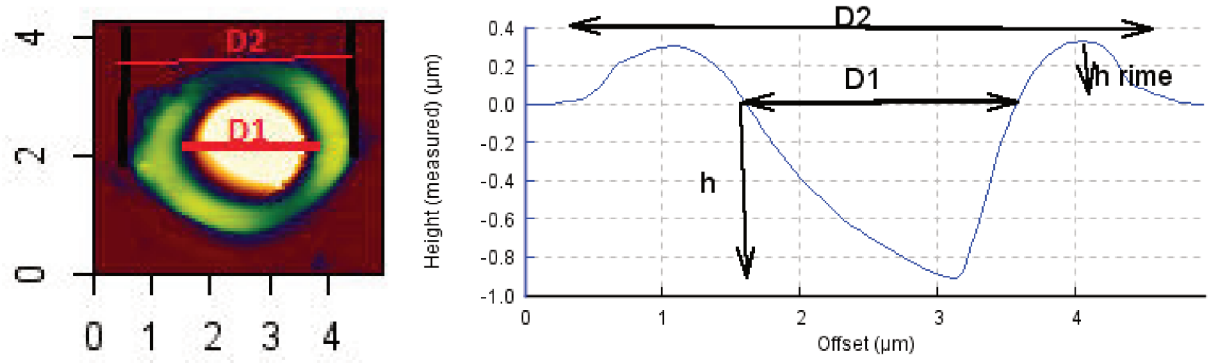

Figure 4. 5 AFM image and profile of the crater obtained on the surface of D263 borosilicate glass with a 2.93 µJ single-pulse.

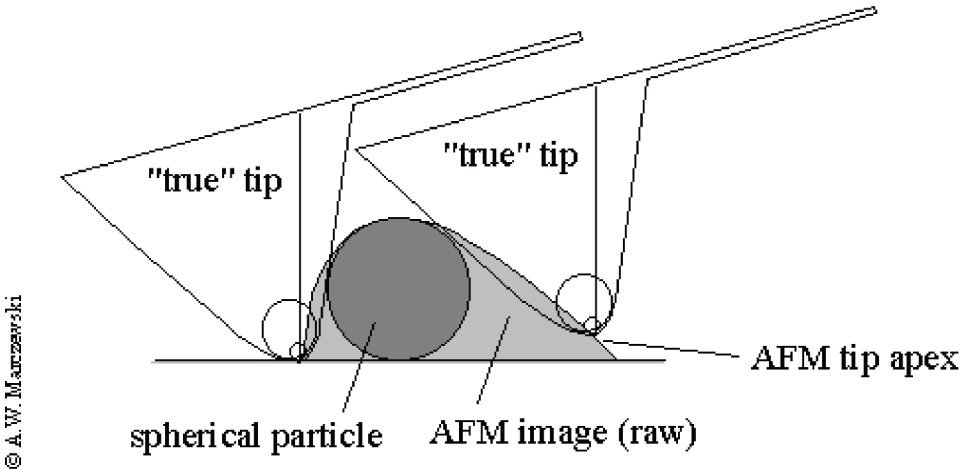

Figure4.6 AFM profile asymmetry due to the geometry of the AFM tip.(com21).

In Fig. 4.5 we define how we have measured the crater parameters from AFM profiles. Crater diameters D1 are defined at the surface level. The molten zone diameter D2 is defined as the external RIM diameter. The crater depths are defined as the lowest point measured by the AFM cantilever tip.

The crater diameter increases with the pulse energy from 0.7µm to a plateau maximum of 1.9 µm at about 2.5 µJ. The molten zone diameter increases more monotonously from 1 µm to 3.7 µm for pulse energies from 0.97µJ to2.93µJ, respectively (Fig. 4.7). The crater depth increases from 0.4µm for our lowest pulse energy of 0.97µJ until it also reaches a plateau depth of 1µm at about 2.25 µJ (fig.4.8).

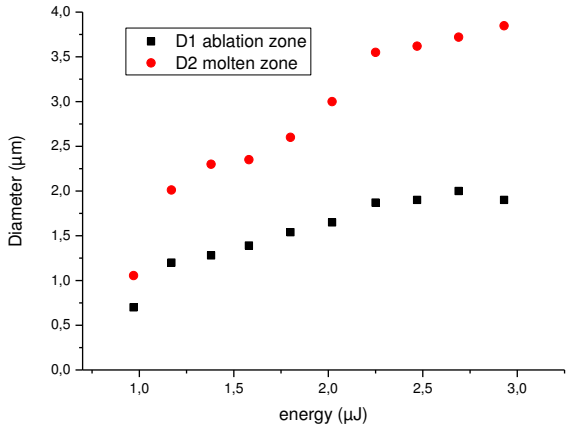

Figure 4.7Crater and molten zone diameters for increasing pulse energies

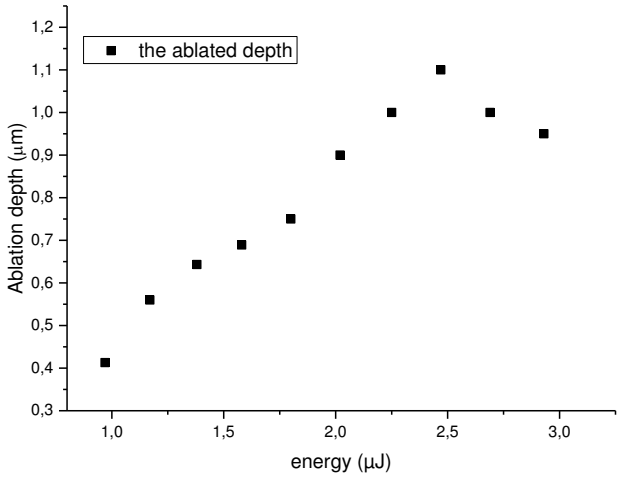

Figure 4.8 Ablation depths for increasing pulse energies

4.1.2 Determination of the ablation threshold for D263 borosilicate glass

As introduced in Chapter 2, the ablation threshold of Gaussian beam intensity can be determined from the equation that describes the diameter increase as a function of the pulse energy increase:

$$D^2 = 2w^2 \ln\left(\frac{E_0}{E_{th}}\right) \quad (4.1)$$

In Fig. 4.9 we have plotted the squared diametersas a function of the natural logarithm of the pulse energies. From the linear fit, the ablation threshold is E_{th}=0.80μJ for a fitted beam waist w = 1.24 μm.

In Chapter 3, we have estimated our beam waist to be 0.37 μm (from PSF lab software). If we have taken into account the beam quality we have find w_0=0.5μm. Thus, the fitted beam waist is about 3.2 times larger than what we expected. Considering that PSF lab software is known to be very precise for this type of calculation, and that we have evidence of thermal effects occurring during the ablation process, we conclude that crater diameters are larger than expected by a factor of 3.2 due to melting effects, i.e. the crater diameter is controlled by a melting threshold waist of 1.24 μm, and not by a cold plasma waist of 0.5 μm corresponding to the laser waist.

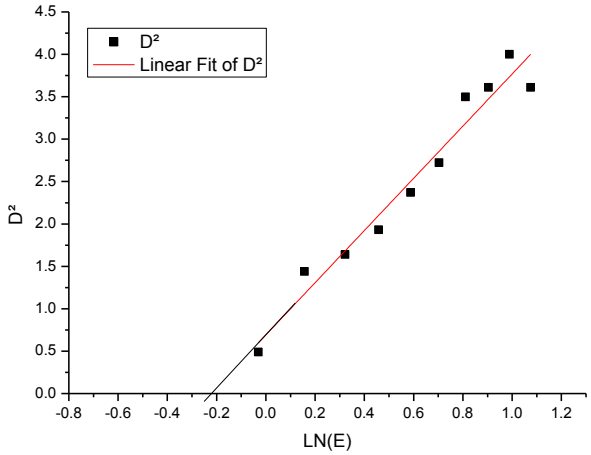

Figure 4.9 The squared diameterD^2 of the crater diameter versus the pulse laser energies in D263 borosilicate glass

4.1.3 The rim height

In our experiments a rim of material is rising above the surface. It results from the resolidification of molten glass on the edges (Chapter 2). The value of rim height increase when the laser pulse energies increase. The rim height is 6 nm for the pulse energy of 0.97µJ, and its value reaches a plateau at 330 nm for the largest energies (Fig. 4.10).

With increasing the pulsed laser energy, the plasma pressure and the melting material temperature increase. Both these factors contribute to decreasing the pressure-driven flow time, which in turn results in a higher rim. The saturation of the rim height at high pulse energies results probably from the increase of plasma reflection that limits the absorbed energy.

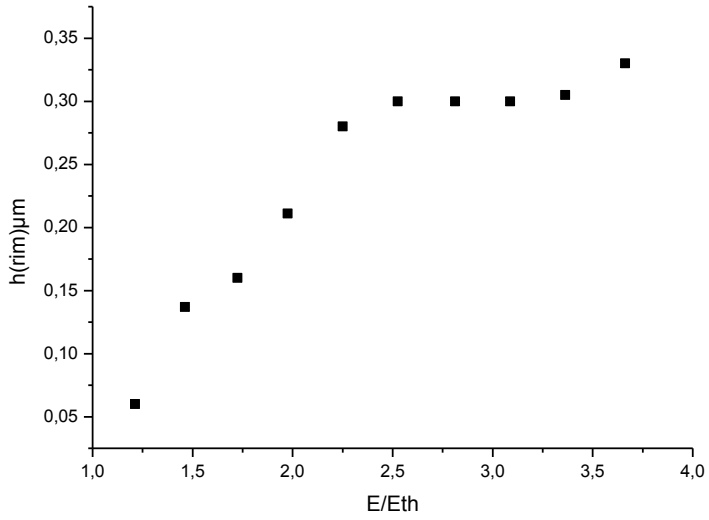

Figure 4.10: the rim height versus the pulse laser energy/threshold energy

4.1.4 Determination of ablation volume and ablation efficiency of D263 borosilicate glass:

For a micromachining point of view, it is important to know how much volume is ablated. The figure 4.11 presents the evolution of the ablation volume estimated using the frustum cone model therefore the ablated volume can be estimated using an approximation by a frustum volume for positions

$0 < z < ½$ h and by a cone volume for positions $½\ h < z < h$:

$$V = Vfrustum + Vcon = \frac{\pi h}{24}(D^2 + 2d^2 + Dd) \qquad (4.2)$$

Where D is the diameter of the crater (ablated zone), d is the diameter at the half depth of crater, and h is the crater depth

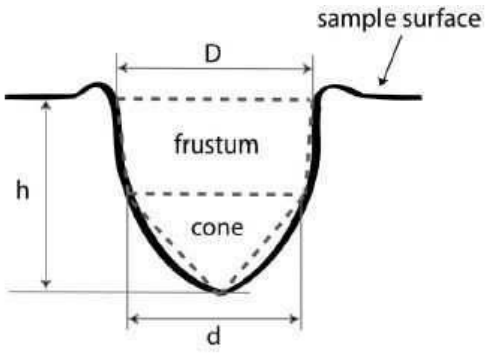

Figure 4. 11 Scheme for calculation of the crater volume by approximation by a frustum and a cone (von, 2009)

The ablation volume as a function of laser pulse energies is presented in the figure (4.12).

The data also shows that the maximum ablated volume is obtained at the incident pulse energy of 2.5µJ/pulse which corresponds to the value of $3E_{th}$. The maximum amount of material removal per unit energy is 1.26µm^{3}of the volume.

Then, we have defined the ablation efficiency η using the ratio of energy required to heat a unit volume to melting point to the energy required to ablated unit volume:

$$\eta = \frac{\rho c_p (T_m - T_0)}{E/V} \qquad (4.\ 3)$$

Where ρ is the density= 2.50Kg/m3, C_p= 820J/Kg K is the specific heat, T0=300K, T_m=1324 K is the melting temperature at which the glass can be easily formed. These results were plotted in the figure 4.13.

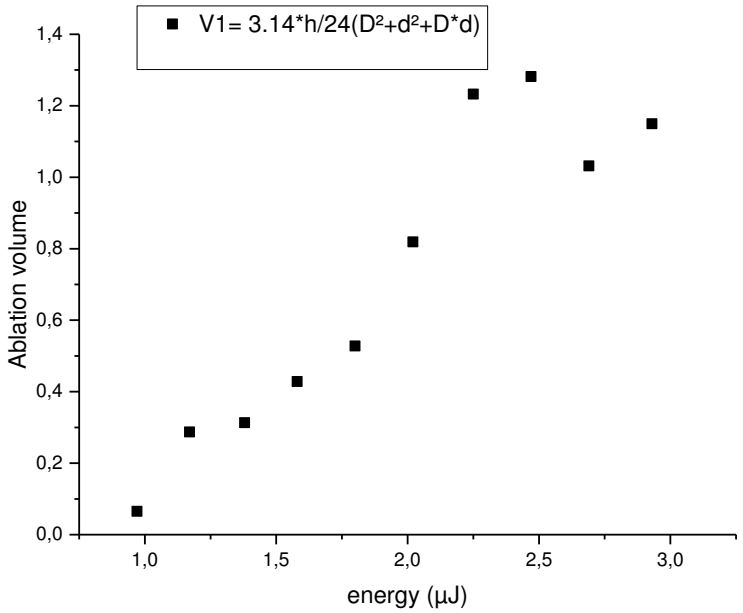

,

Figure 4.12: The volume of the ablated craters as afunction of laser pulse energies

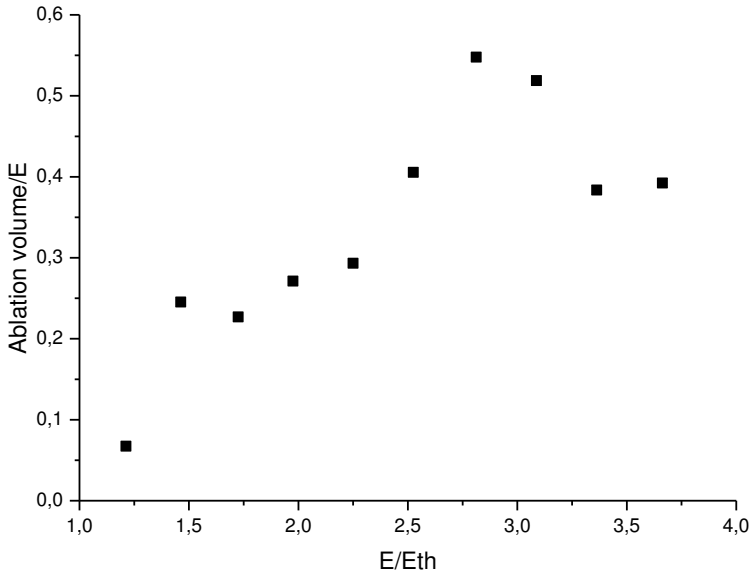

Figure 4.13 the volume per unit input energy (V/E) as function E/E_{th}

As Fig 4.14 shows, the value of ablation efficiency is $\eta \simeq 0.12\%$ at $E=3E_{th}$. Thus, only 0.12 % of input energy is used to melt the ablation volume. The energy required to melt $1cm^3$ of

D263borosilicate glass is approximately 2.2 KJ. In addition, the ablation efficiency is reduced when the irradiation energy is more than 3 times of the threshold energy. This is probably due to the increase of plasma reflectivity, when the glass is exposed to fluence above threshold(M.D.Perry, 1999). Thus, most of the incident energy is reflected back from the sample. Thus, there is an optimal fluence level (relative to the threshold fluence) for which the volume removal rate is the highest.

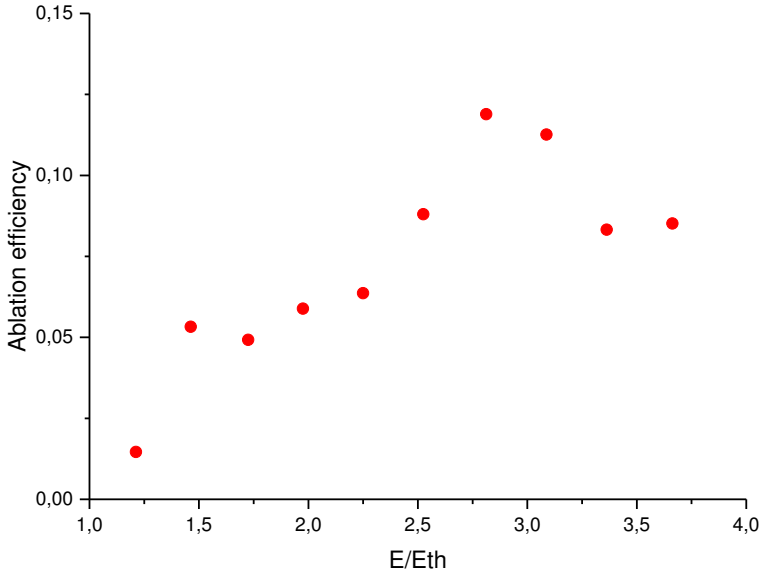

Figure 4.14 the ablation efficiency versus $E/_{Eth}$

4.1.5 Fabrication of ablation lines on the surface of D263 borosilicate glass.

In these experiments we have ablated lines at the surface of D263 borosilicate glass by scanning a pulsed laser beam with different laser pulse energies. We have performed this experiment with a single pass of laser pulses. They spatial distance between of single-sequential pulses was 40 nm, i.e. about 10% of the focal spot diameter.

4.1.5.1 Influence of the laser pulse energy on line morphologies

Figures 4.15 and 4.16 show the transmission optical microscope images, and AFM images of written lines in D263 borosilicate glass for various pulse energies. It is clear that the morphology of the written structures depends on laser pulse energies. We can observe that at 0.80µJ/pulse the fabricated line is not continuous, so the absorbed energy is not enough to ablate all the line.

The AFM profiles of ablation lines are shown on Figures 4.17 and 4.18. The increases of line widths and depths with increasing energy are plotted on Figures 4.19, and 4.20. The line width increases from1.6µm to 2.8 µm for pulse energies ranging from 0.80µJ to 2.93µJ/pulse. The line depths increase from 0.5µm to 2.80µm. The vertical error bars correspond to the deviation observed on AFM measurements of four cross-sections of crater along the ablated line. The ridges on both sides of the ablated lines is very small as shown is the fig 4.18, and also the heat affected zone have been found to be very small in comparison to the results in the ablated spots as shown in the Figures 4.1, 4.2, and 4.3.

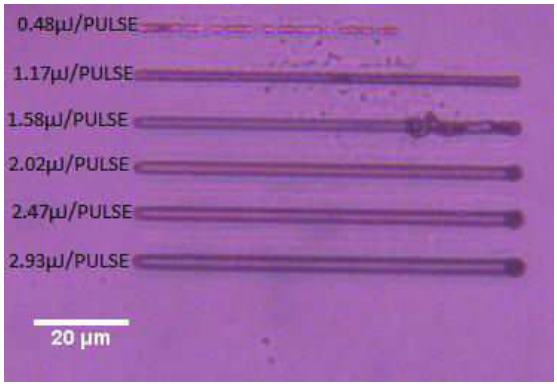

Figure 4.15 optical microscope images of lines fabricated at the surface of borosilicate glass with one pass

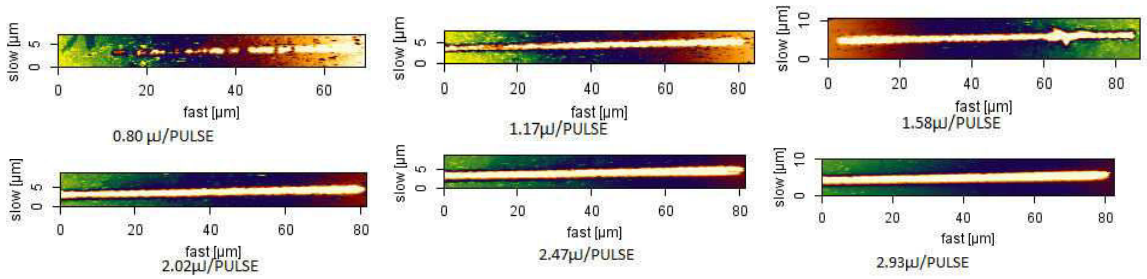

Figure 4.16:AFM images of lines fabricated at the surface of borosilicate glass

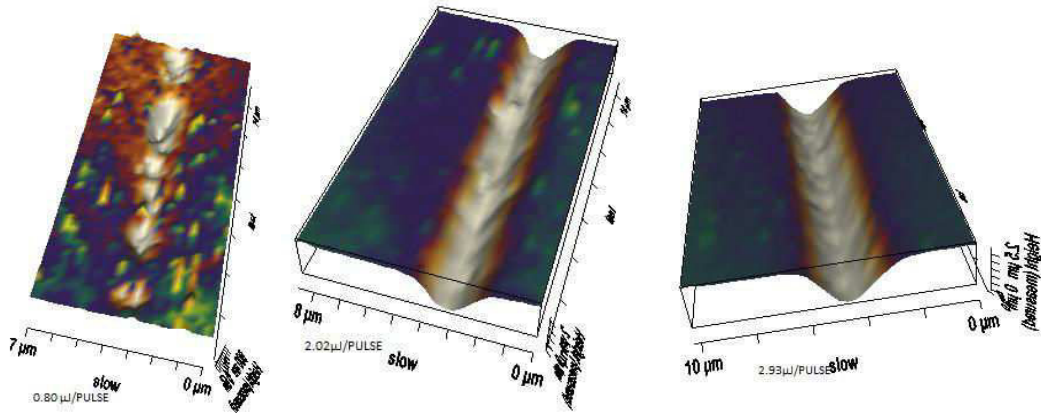

Figure 4.17: three-dimensional AFM images of lines craters ablated at the surface of D263 borosilicate glass with three different laser pulse energies, E=0.80,2.02, and 2.93µJ/pulse

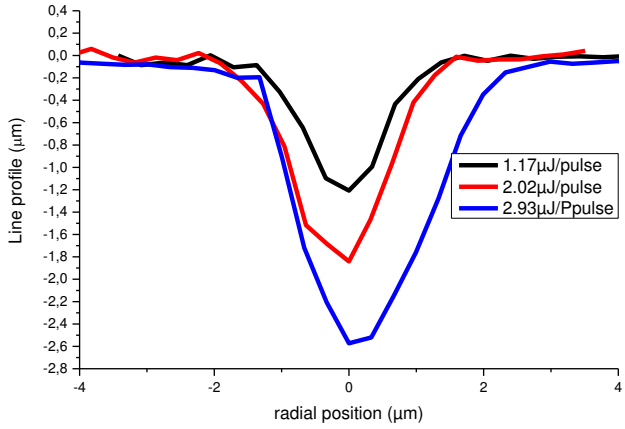

Figure 4.18:AFM line profiles

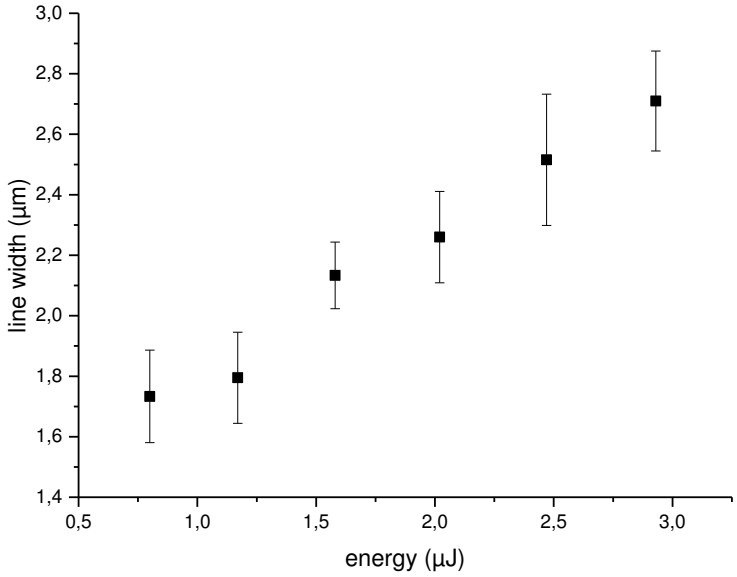

Figure 4.19:Line width as a function of the pulse energy

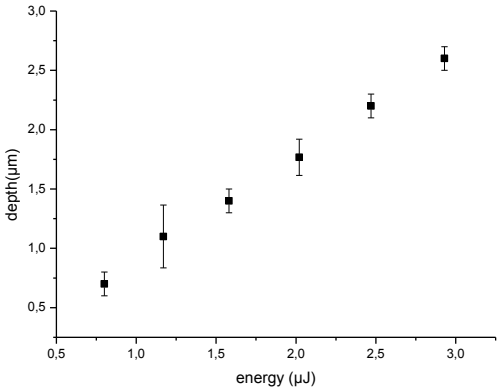

Figure 4.20 Line depth as a function of the pulse energy

4.2 Ablation of craters and lines at the surface of BK7 glass.

We have performed our experiments with a sample of BK7 glass which have regions with ion-doped (silver, thallium) waveguides on its surface. The transmission optical microscope images of craters are shown on Fig. 4.21.All the craters on each image have been obtained with single

pulses of the same energy. Some are on the ion-doped waveguide (vertical feature in the middle), the others are on the non-doped BK-7 surface (each sides of the vertical waveguide). We can clearly see that all the craters are surrounded by a heat affected ring (clearer ring around the dark crater). Its micron-size thickness (about 1 μm) does not seem to be very sensitive with the pulse energy.

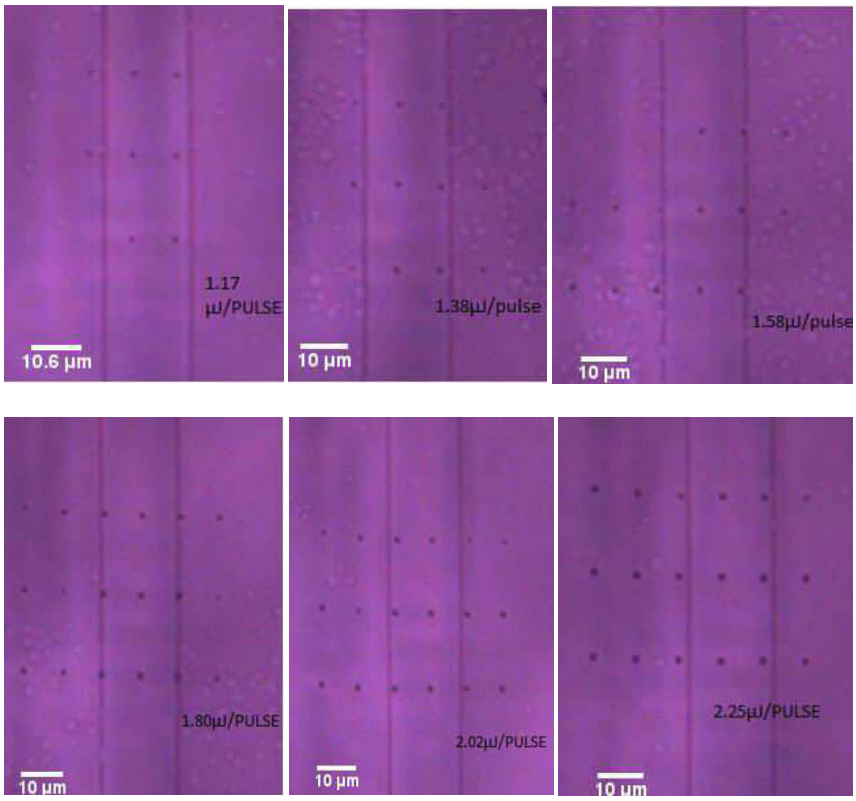

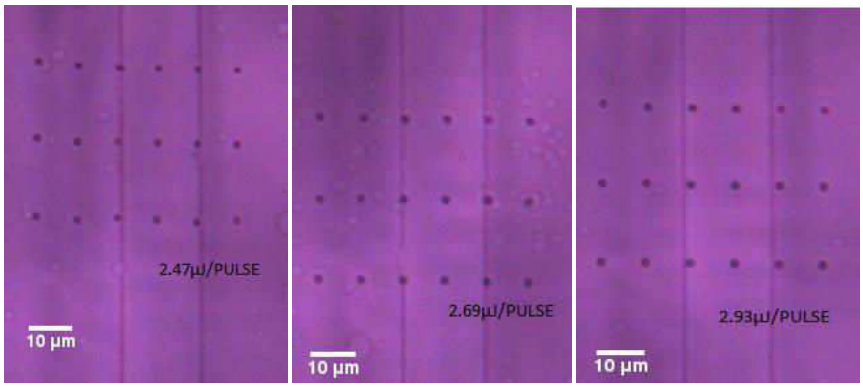

Figure 4.21: optical microscope images of craters fabricated on the surface of BK7 glass with a vertical ion-doped waveguide at the middle.

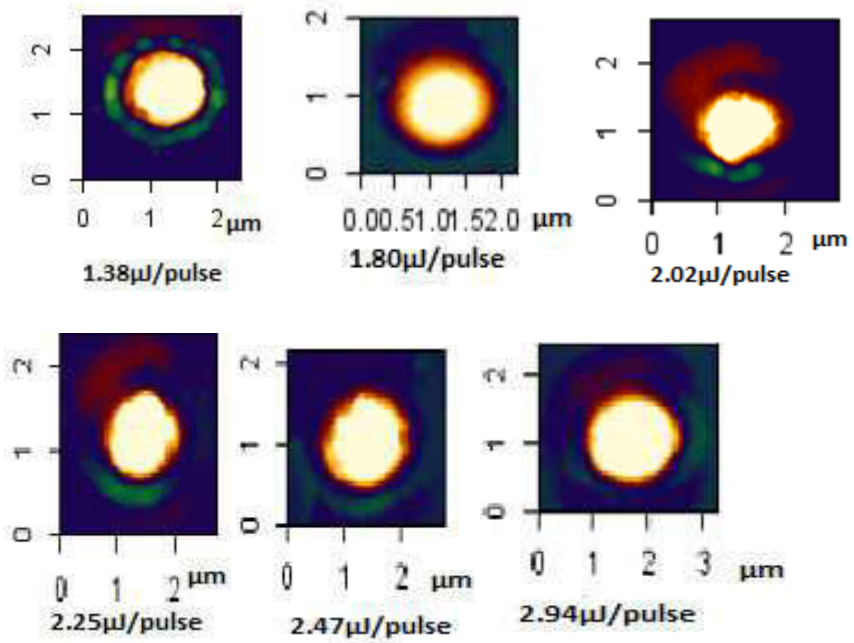

Figure 4.22: AFM images of ablation craters on the surface of non-doped BK7 glass

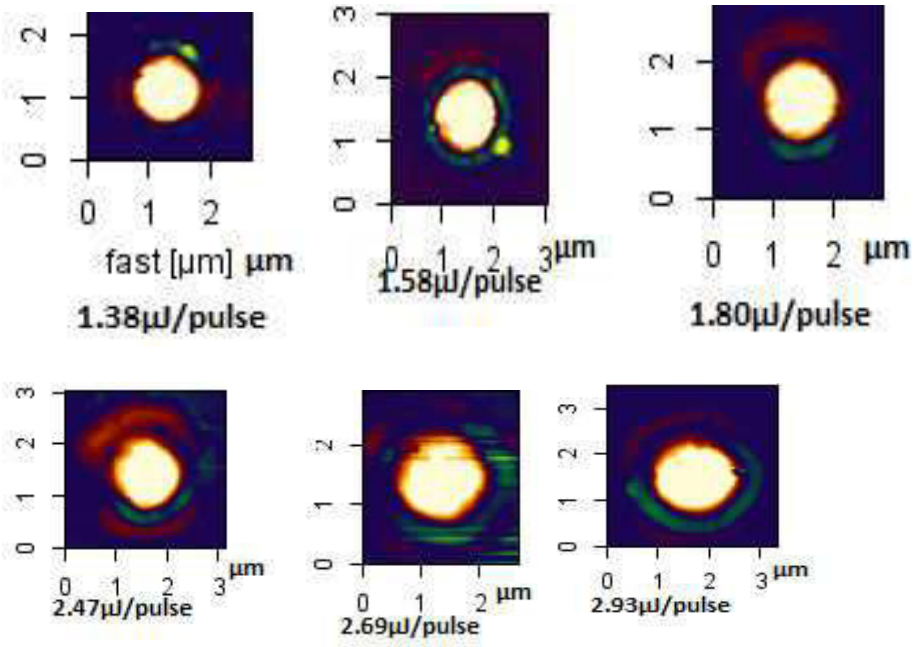

Figure 4.23: AFM images of ablation craters on the ion-doped waveguide surface.

Figure 4.24 shows the AFM images of plot fabricated on the surface of non-doped BK7 glass, and of plots fabricated on the ion-doped optical waveguide (pulse energy = 2.93 µJ). The corresponding profiles are on Fig. 4.25. The waveguide crater has about the same width, but has a deeper height than the non-doped crater. Also, it has an additional RIM.

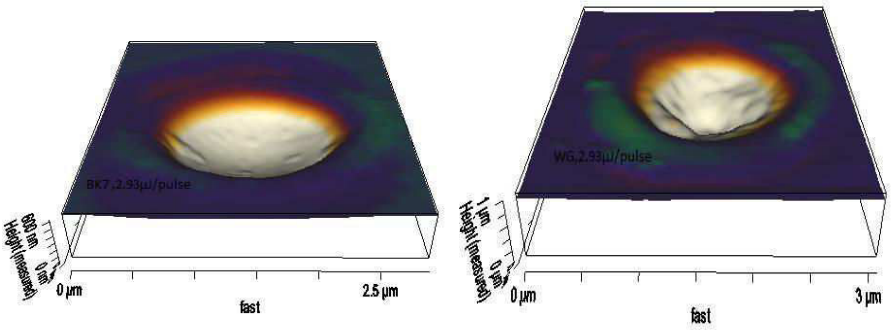

Figure 4.24: 3D image of ablation craters on non-doped BK7 (left) and on ion-doped waveguide (right) witha single-pulse energy of 2.93 µJ.

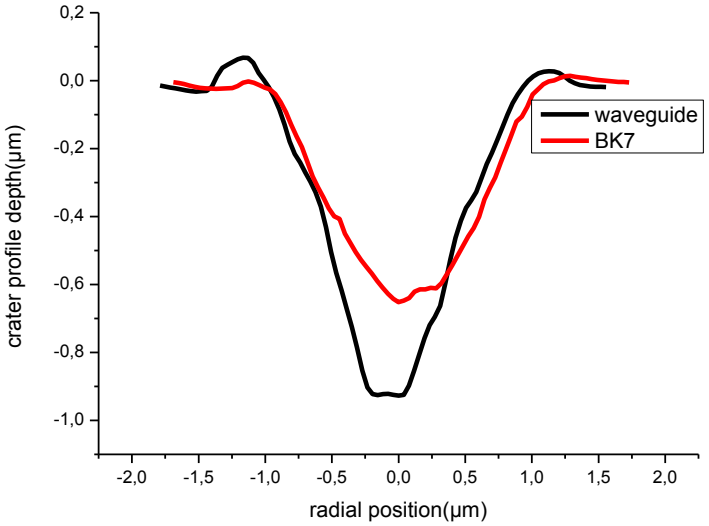

Figure 4.25: profiles of ablation craters on non-doped BK7 (left) and on ion-doped waveguide (right) witha single-pulse energy of 2.93 µJ.

Energy dependent measurements confirm the similar widths of craters and the deeper ablation at the same pulse energy on ion-doped waveguide (Fig.4.26 and 4.27). In addition, on non-doped surfaces, craters are smoother.

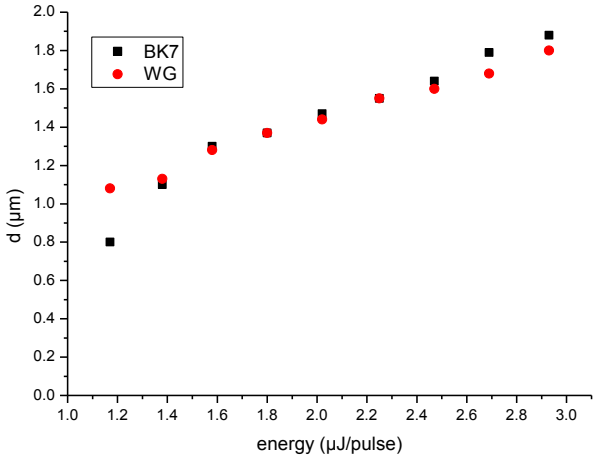

Figure 4. 26 crater width as a function of the pulse energy

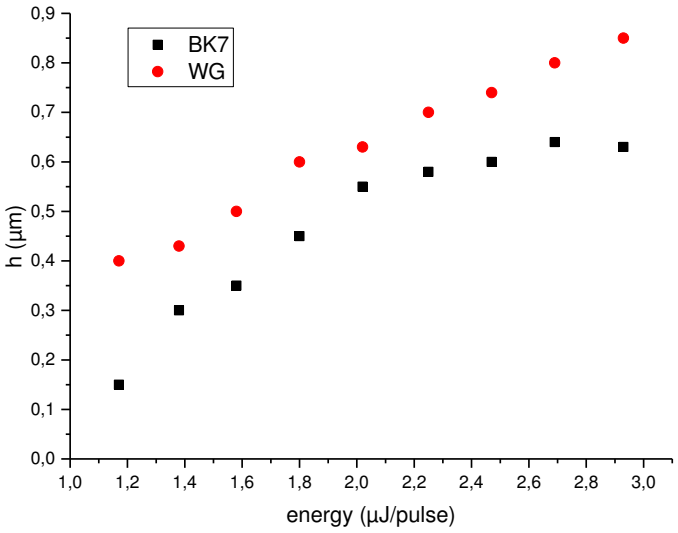

Figure 4. 27crater depth as a function of the pulse energy

4.2.1 Determination of the ablation threshold of non-doped BK7 glass

The ablation threshold measurements of BK7 glass are plotted on Fig. 4.28.There is a linear relation between the squared diameters and the natural logarithm of the pulse energies. From the

linear fit, we obtain a threshold energy of E_{th}=1.07µJ, and an effective threshold waist of w_0 = 0.934µm which is about 2.5 times more than the value obtained with PSF lab.

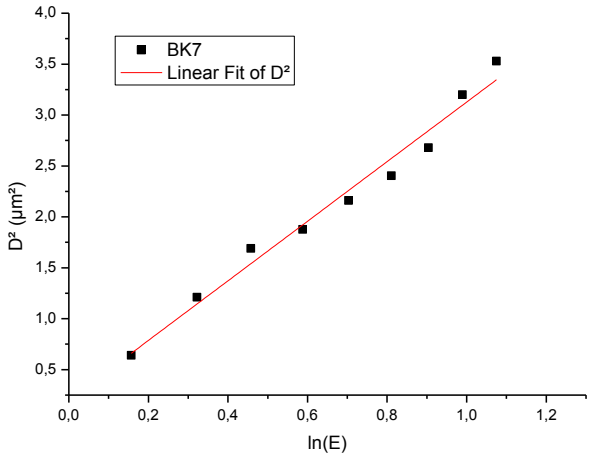

Figure 4.28 the squared diameters of craters measured by AFM profiles as a function of the pulse laser energy onnon-doped BK7 glass.

4.2.2 Determination of the ablation threshold on ion-doped BK-7 waveguides BK7/

The ablation threshold measurements on the ion-doped BK-7 surface isplotted on Fig. 4.29.From the linear fit, we obtain a threshold energy E_{th} = 0.75µJ which is significantly lower than the non-doped region (E_{th}=1.07µJ), and an effective ablation waist w_0 =1.049 that is slightly larger (w_0 = 0.934µm).

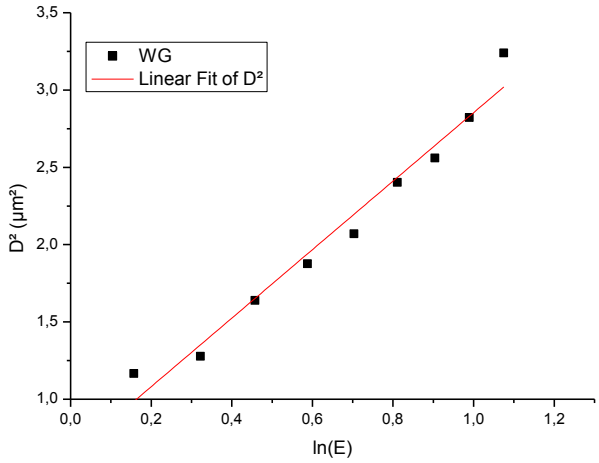

Figure 4.29: the squared diameters of ablation craters on the ion-doped BK-7 waveguide. as a function of the pulse energy.

4.2.3 Micro-channels fabrication at the surface of the ion-doped B7-7 waveguide

In this section, the goal was to engrave micro-(fluidics) channels perpendicular to the optical waveguide. We have investigated how the processing parameters such as the pulse energy, the pulse spatial separation, and the number of passages affect the micro-channel geometry.

Micro-channels were fabricated on one pass with single-pulse (1 ms between consecutive pulse) focalized at incremental spatial locations. Experiments were done with pulse spatial separations varying from 0.1 to 0.25 µm, to be compared with the size of focus spot: FWHM = 0.4 µm. Figures 4.30 and 4.31 show the AFM images of micro-channels obtained with a pulse energy of 0.48µJ.

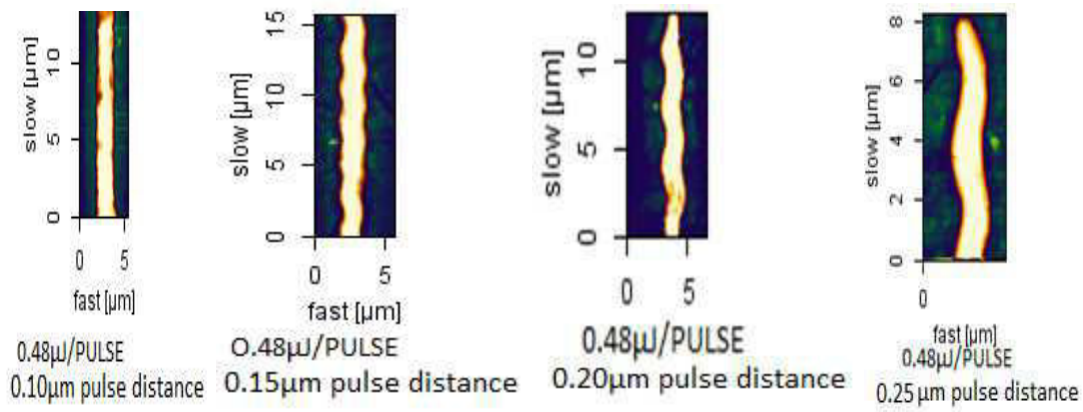

Figure 4. 30 the AFM images of single line writing on fabricated waveguide in BK7 sample after irradiation at 532nm, 0.48µJ/pulse at different pulse distance

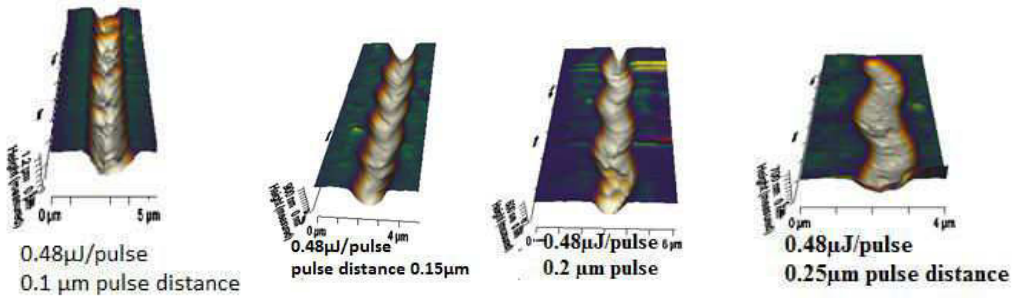

Figure 4. 31 3D images of ablated lines with 0.48µJ/pulse at different pulse distance

4.2.3.1 Influence of the pulse energy and of the pulse spatial separation on micro-channel profiles.

Figures 4.32 and 4.33 show the AFM images and profiles of micro-channels obtain with a fixed pulse spatial separation of 0.1 µm (25% of the FWHM spot size), and increasing pulse energy from 0.48 to 2.47 µJ. The channel widths and depths increase linearly from 1 to 3µm and from 1 to 4.7µm, respectively. There is no significant RIM formed on the micro-channel ridges.

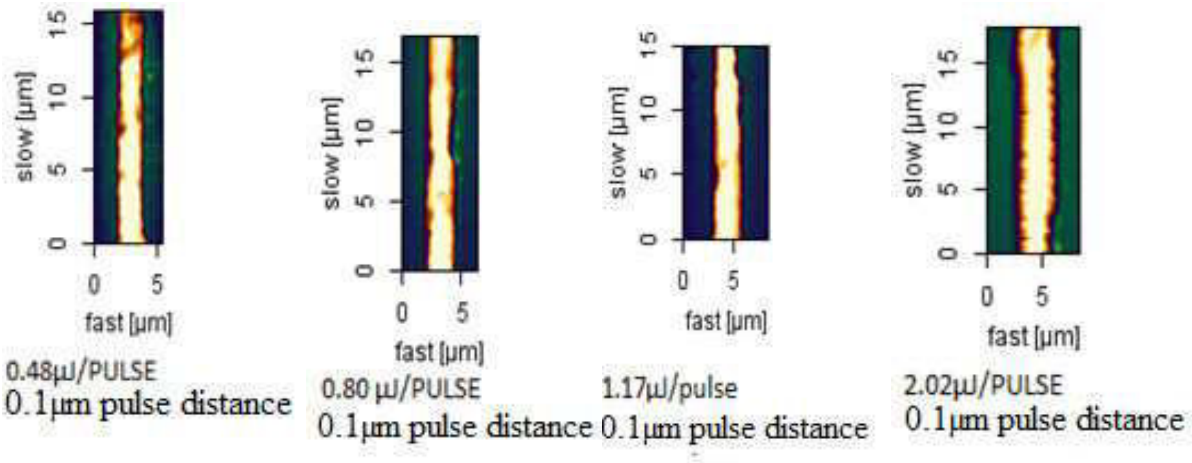

Figure 4. 32: AFM images of micro-channels on ion-doped BK-7 waveguides for various pulse energies and a pulse spatial separation of 0.1 µm.

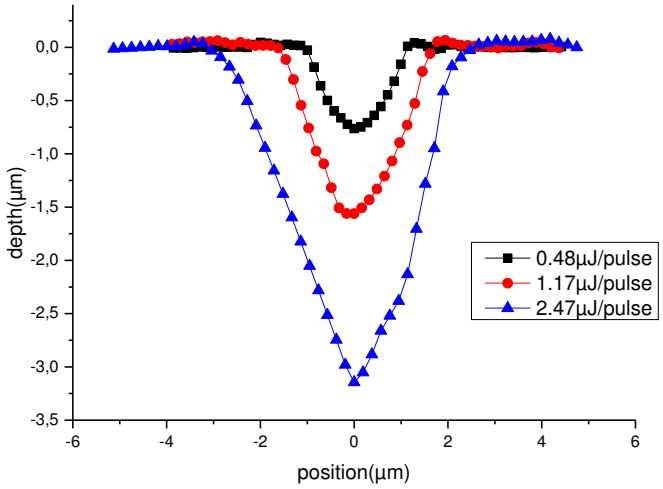

Figure 4. 33: 2D cross-section profiles micro-channels on ion-doped BK-7 waveguides for various pulse energies and a pulse spatial separation of 0.1 µm.

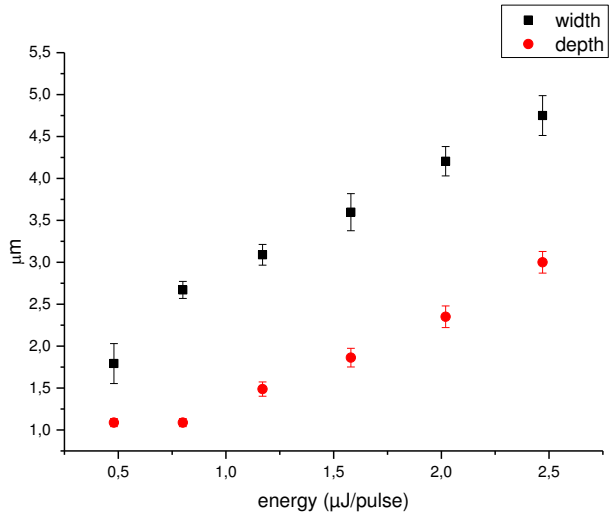

Figure 4. 34: widths and depths of micro-channels on ion-doped BK-7 waveguides for various pulse energies and a pulse spatial separation of 0.1 µm.

In Figures 4.35, we have plotted the influence of pulse separation on the profile characteristics of micro-channels obtained with pulse energy of 0.48 µJ. The micro-channel width does not change significantly with the pulse separation distance. However, its depth increases strongly with short distance which indicates a strong melting memory effect (1 ms between two pulses).

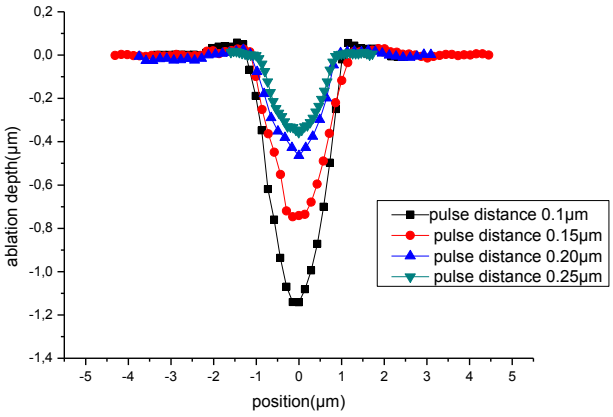

Figure 4. 35 2D groove cross- section profiles with 0.48µJ/pulse at different overlap distances

In Figures 4.36 and 4.37 we have plotted the simultaneous influences of pulse energy and distance on micro-channel widths and depths. These data confirm the trends observed previously of the width only sensitive with the pulse energy, and the depth strongly dependent with both parameters.

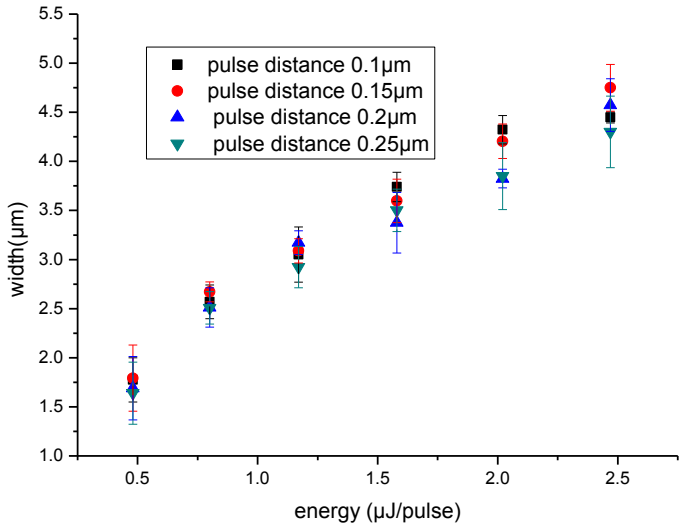

Figure 4. 36: Effects of pulse energy and pulse distance on micro-channel widths

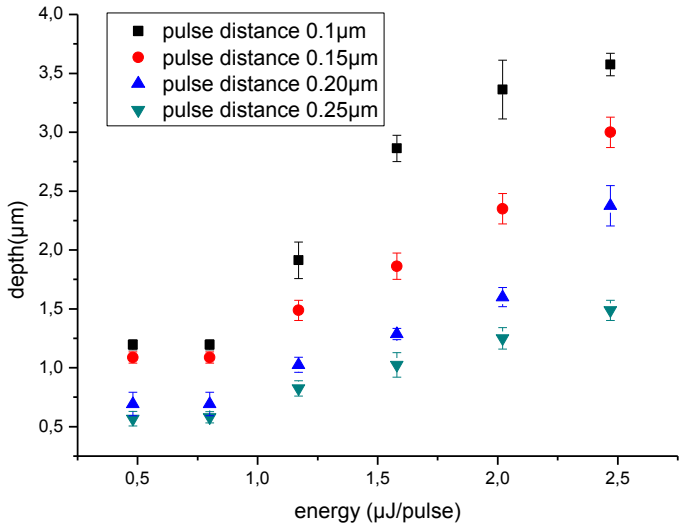

Figure 4. 37:Effects of pulse energy and pulse distance on micro-channel depths

4.2.3.2 Observation of spatial ripples along the micro-channel direction

Figures 4.38 and 4.39 show the AFM images of micro-channels obtained with different pulse energies (same pulse energy per image rows), and with different pulse distances (same pulse distance per image column). We can see that micro-channels are fabricated with unwanted ripples along their directions. The ripple amplitudes and periods depend on pulse energies and distances.

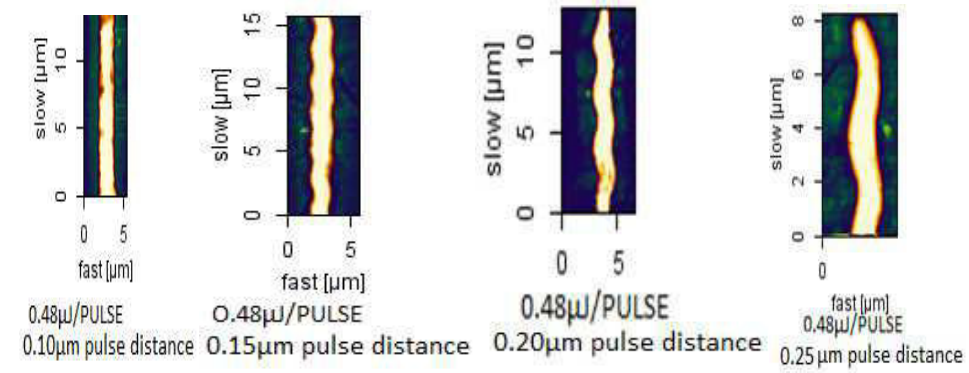

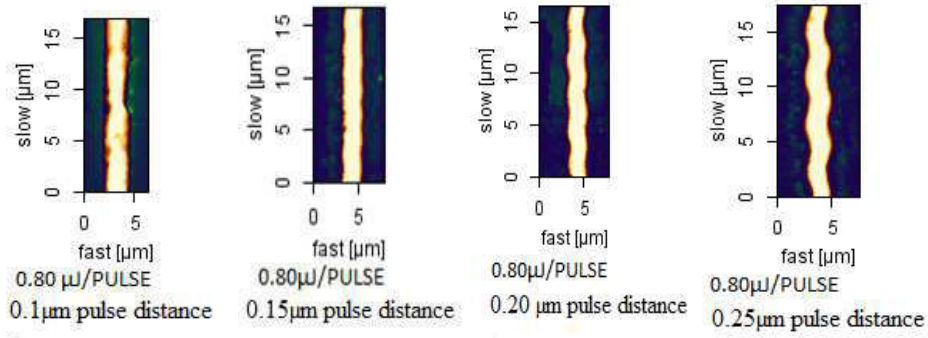

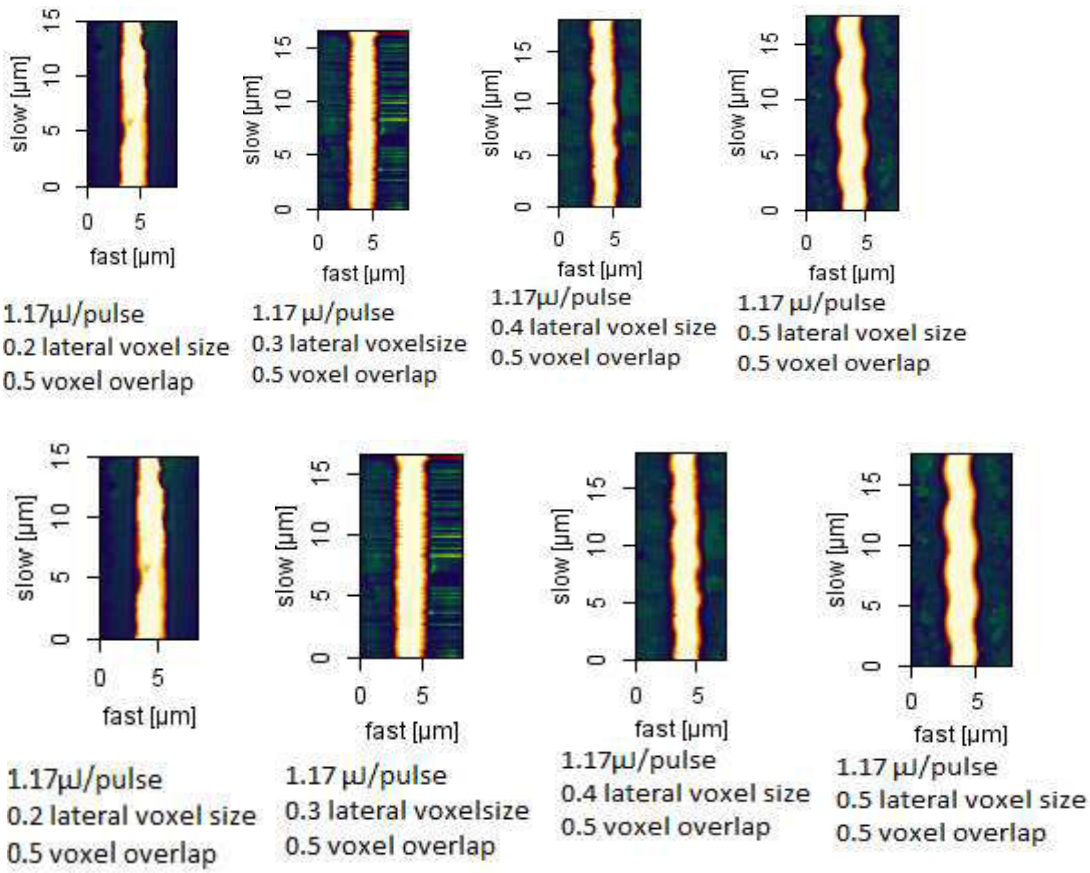

Figure 4. 38: 2D AFM images showing the effects of pulse energies and distances on the ripple amplitudes and periods.

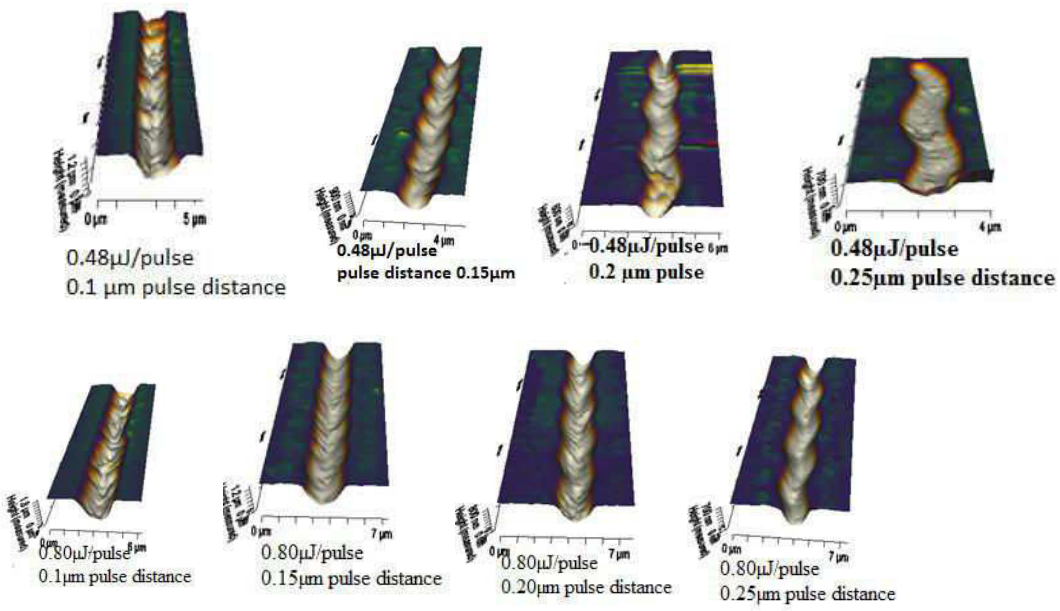

Figure 4. 39: 3D AFM images showing the effects of pulse distances on the ripple amplitudes and periods for pulse energies 0.48 and 0.8 J.

The ripple can be clearly seen with lower pulse energies and larger pulse distances. Their periods increase with the pulse distance, and decrease with the pulse energy (Fig.4.40 and 4.41). The physical relationship with the pulse distance is not obvious because the ripple period is an order of magnitude larger than the pulse distance.

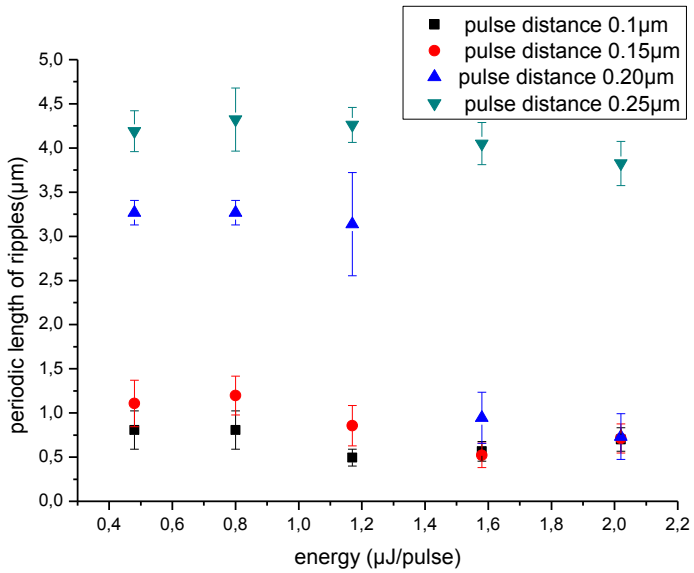

Figure 4. 40: Effect of pulse energy and distance on the ripple

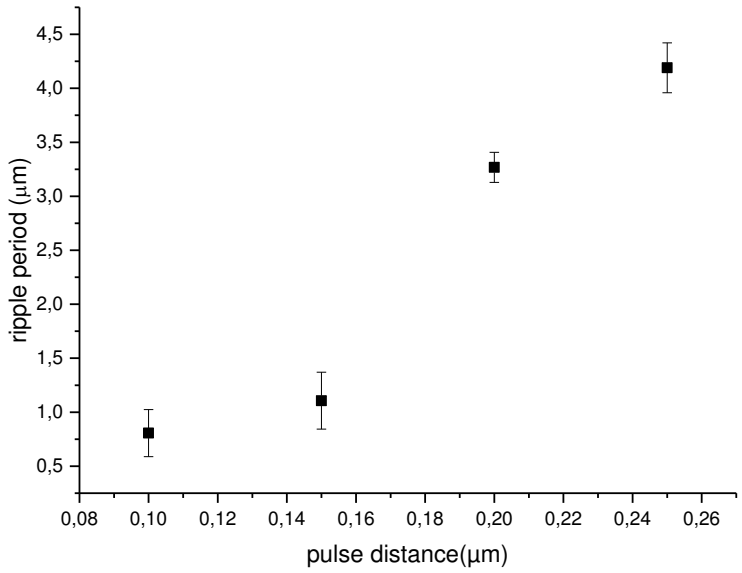

Figure 4.41: influence of the pulse distance on the ripple period for a pulse energy of 0.48µJ.

4.3 Ablation of craters and lines at the surface of SBS thermoplastics

In this sectionwe present the morphology of ablation craters and lines on the thermoplastic sample, which is a sensible material for the thermal effects. In this study the laser beam was focused using an objective X20 with a numerical aperture of0.45 (w_0 = 0.53 µm). The ablated spot are examined bytransmission optical microscopy.

4.3.1 Effect of laser pulse energies on crater diameter, and ablation threshold

Figure 4.42 shows optical transmission images of craters fabricated on the surface of SBS thermoplastic at different single-pulse energies from 1.7µJ to 3.35µJ. The crater diameters increase with pulse energies, from 2.5 µm to 5.5 µm as shown on Fig. 4.59. The vertical error bars correspond to the deviation observed on measurements from four experiments with the same conditions. One can note that craters are clearly deformed by thermal effects, a significant difference with ablation craters on glasses.

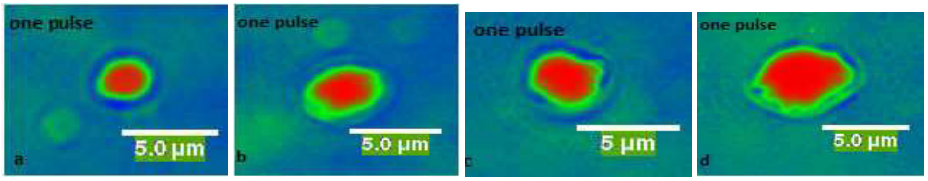

Figure 4.42: optical transmission images of craters on SBS thermoplastic surface after irradiation by single-pulse at energies a) 1.76 µJ, b) 2.25µJ, c) 2.81 µJ,d) 3.35µJ.

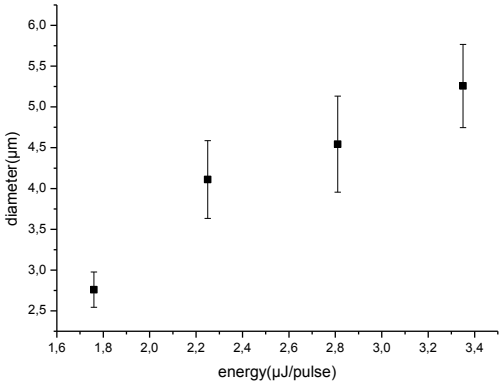

Figure 4.43:diameters of ablation craters on the surface of SBS thermoplastics at different laser pulse energies

The single-shot ablation threshold measurements on the SBS thermoplastic are plotted on Fig.4.44.It shows the linear relation between the squared diameters, and the natural logarithm of the laser pulse energies. From the linear fit of the equation 4.3, we obtain an ablation threshold E_{th} = 0.5µJ/pulse, and an effective ablation waist of w = 3.3µm.It is clear from these values that SBS thermoplastics has the lowest energy threshold, and the largest thermal effects.

.

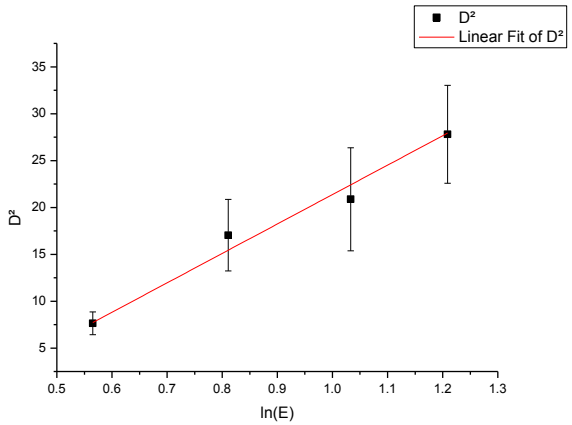

Figure 4.44: determination of ablation threshold for SBS thermoplastic

4.3.2 Effect of multiple pulses on ablation crater

Figure 4.45 shows images of obtained with sequences of pulses (1, 2, 5, 10, and 15) separated by a time delay of 1ms. The crater diameter increases with 2 and 5 pulses, but seems to reach a limit after 5 pulses.

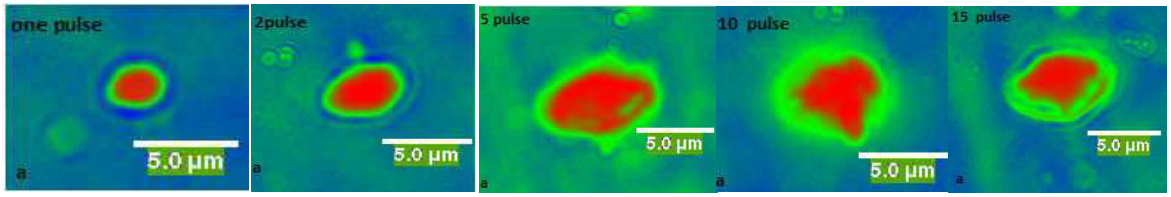

Figure 4.45: optical transmission images of ablation craters obtained on SBS thermoplastic surface after irradiation by multiple successive pulses (pulse energy = 1.76 µJ, time delay between pulses = 1ms)

4.3.3 Effects of the time delay between pulses to fabricate ablation lines

In this experiment, we study the parameters that control the fabrication of lines. At the difference with previous experiments with borosilicate and BK-7 glasses we have to take into account for the dynamics of thermal effects. Figure 4.46 shows the transmission optical images of lines fabricated with a pulse separation distance of 1µm for increasing pulse energies (0.8, 1.06, 1,28, and 1.7 µJ), and time delay between pulses (100 ms, 500 ms, 1 sec, 2 sec, and 5 sec).One can see strong deformations induced by thermal effects with 100 ms, and 500 ms delays. However, they are non-significant for delays larger than 1sec.

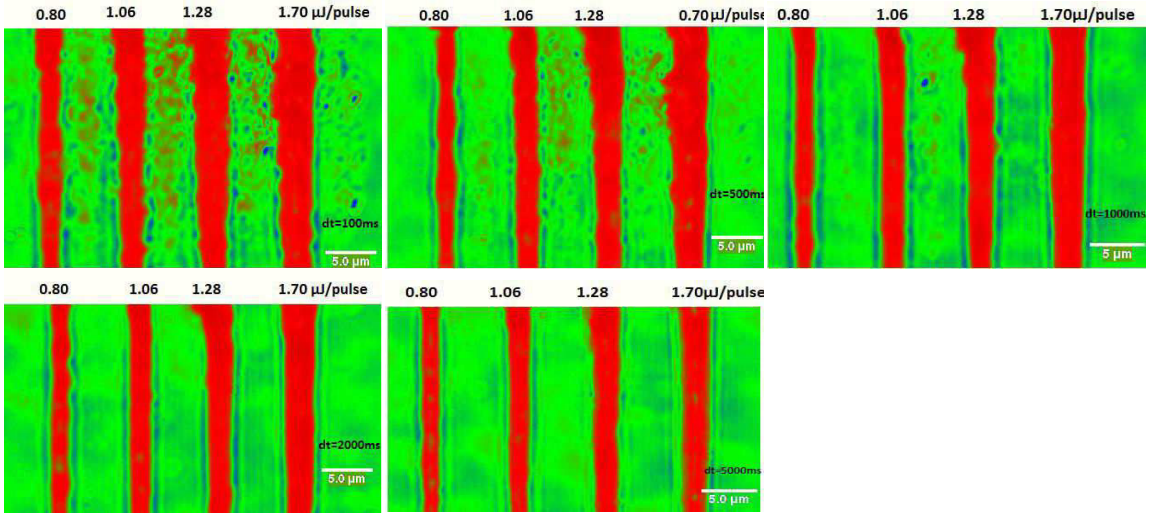

Figure 4.46: transmission optical microscopy images of fabricated lines on SBS thermoplastic with different laser pulse energies, and different time delay between the pulses.

The influences of pulse energies and pulse delays on the line widths are plotted in Fig. 4.47 and 4.48, respectively. Line widths are larger with smaller pulse delay which confirms the contribution of thermal effects on ablation (melting and material evaporation). Line widths do not change with delays larger than 1000 ms.

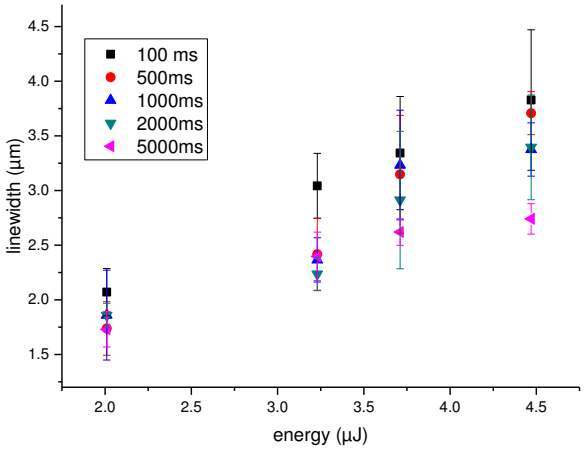

Figure 4.47: line widths as a function of pulse laser energies for different time delay between pulses.

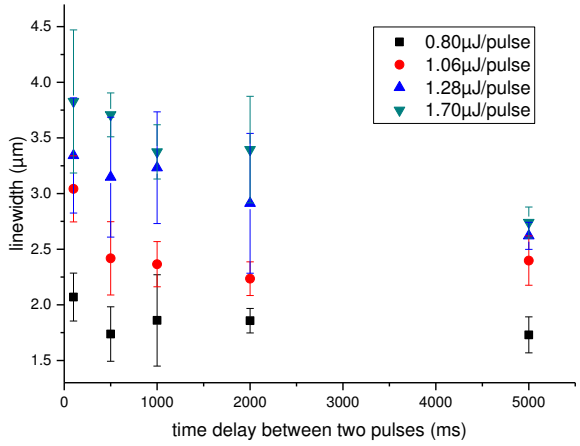

Figure 4.48: line widths as a function of the time delay between pulses for different pulse energies.

4.3.4 Influence of the separation distance between pulse on the line fabrication

In this experiment, we change the separation distance between consecutive pulses during the fabrication of ablation lines on SBS thermoplastics. Figure 4.49 shows the images of results obtained with separation distances varying from 1 to 10 µm, and for pulse energies from 1.28 to 3.35 µJ. Continuous lines with minimal thermal effects are obtained for all pulse energies when the pulse separation distance is optimum. Larger pulse energies need larger pulse separations, and leads to larger line widths.

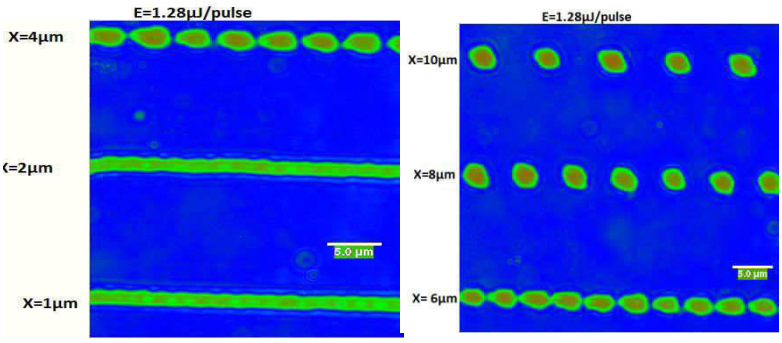

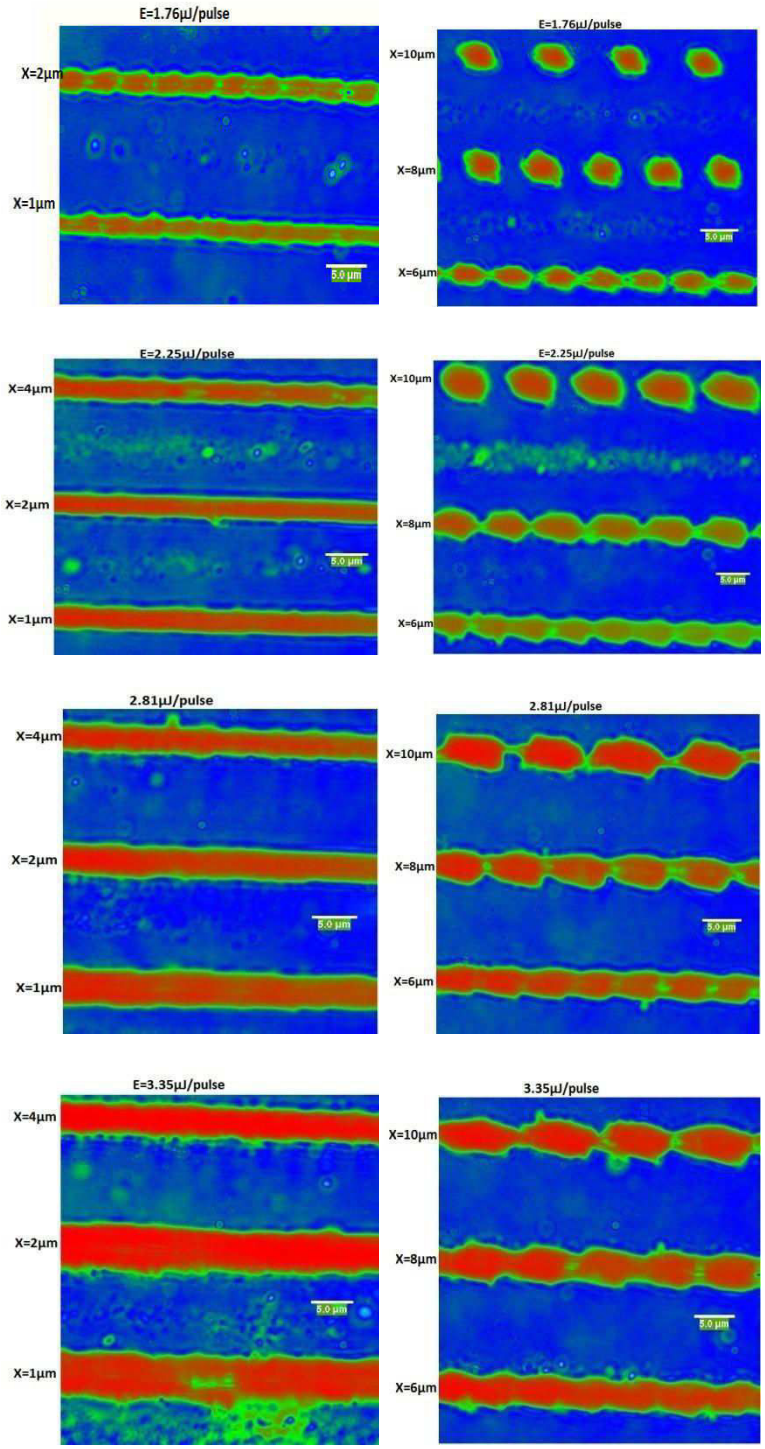

Figure 4.49: Transmission optical microscopy images of for various pulse separation distances, and increasing pulse energies.

4.3.5 Minimum distance between parallel lines without significant thermal deformations

In this experiment we have fabricated parallel lines with a pulse energy of 1.28µJ, a pulse separation distance of 1µm, and a time delay between pulses of 5s.The laser was focalized with an oil immersion objective with a numerical aperture of 1.3.The distance between the parallel lines have been tested from 3µm to 15µm (Fig. 4.50). For this pulse energy, strong thermal effects deform the lines only when the line distances is smaller than 5 micron.

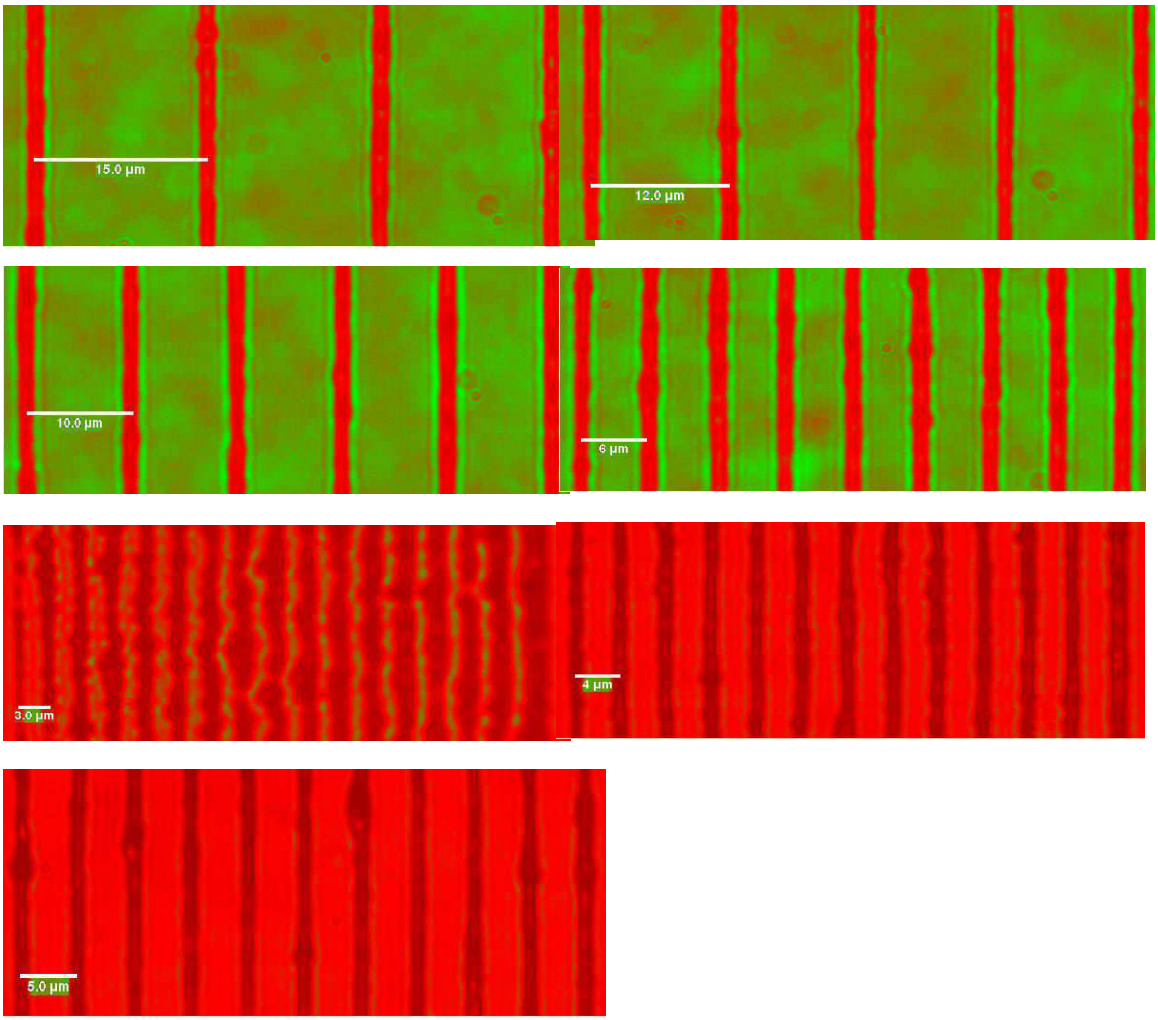

Figure 4.50: Optical microscopy images of parallel lines fabricated by laser ablation on SBS thermoplastic for different distances between the lines.

4.5 Conclusion

In this chapter, we have presented our ablation results with an amplified self-Q switched micro-chip laser with sub-nanosecond pulses. We have tested three very common dielectric materials: two type glasses, and a thermoplastic.

The threshold of laser ablation for these three materials has been determined with the extrapolation of the linear relationship between the square of crater diameter and logarithm of laser energy, the results show that there are a thermal factor that affects the diameters of craters fabricated in these materials, and this factor is biggest in the thermoplastics. The results show that the ablation threshold in glasses materials is in order of TW/cm^2.

The volume of the ablated craters and the energy efficiency of sub-nanosecond pulsed laser ablation of D236 borosilicate glass have been calculated. The maximum amount of material of removal energy is about 1.26 μm^3 when the incident energy reaches the level $E=3E_{th,}$ and also the highest ablation efficiency is at this level of energy and then the ablation efficiency decreases 50%

The results of micro-channel scribing in BK7 with ion (silver, thallium) doped optical waveguide glass and the effects of pulse distance, pulse energy, and the number of passage on groove geometry and the surface morphology have been investigated.

- With increasing the pulse distance the width doesn't change until 0.2µm, then decreases, the depth decreases with increasing the pulse distance, while the periodic ripples length increases, thus the pulse distance can be used to control the geometry of the micro-channel fabricated.

- The width and depth of ablated lines increase with increasing the pulse energies, which is the result of increasing the amount of absorbed energies with increasing the pulse energies. But the periodic length of ripples decreases until the pulse energies of 1.17μJ/pulse then it increases.
- Wider and deeper lines can be scribed at two and three passages

The results of SBS thermoplastic show that, the width increases with increasing the pulse energies and number pulse until 5pulse then decreases with increasing the number pulse. In addition, the width of fabricated structures inside the SBS thermoplastic is affected by the time between the pulses and the distance between the spots and lines. The width of fabricated lines decreases with increasing the time between pulses until 1s, unchanging after this value. Also, we have obtained good structure without thermal effects when we have used the time of 0.5s.The effects of distance between the spots and the structure on the morphologies have been also investigated at various pulse energies. When the pulse energies is less than $5E_{th}$ the width increases with increasing the distance until 8μm then it decreases with larger distance, while it decreases with increasing the distance when the pulse energies is more than $5E_{th}$ unchanging after the distance of 8μm. Thus we can control the processing parameters to fabricate good structure without thermal effect by increasing the time between the pulses and the distance between the structures for eliminate the effect of thermal diffusion which is the result of high thermal diffusivity of thermoplastic materials.

Chapter 5
Results analysis

In this chapter we identify and calculate the initial steps of laser ablation of transparent materials, and we study the thermal effects in sub-nanosecond laser ablation of transparent materials versus the properties of materials and the focal depth.

5.1 Photo-ionization induced by multi-photon absorption

This step is the beginning of free-electron generation by two-photon absorption. The material keeps its dielectric optical properties. We have calculated the two-photon ionization coefficient.

To calculate the photo-ionization absorption we have used the generic form of the temporal evolution of free-electron density ρ(Y. R. Shen, 1984; Kennedy, 1995; B. C. Stuart, 1996.):

$$\frac{\partial \rho}{\partial t} = \sigma I^k + \alpha_c I \rho - \eta_{rec} \rho^2 - \eta_{diff} \rho \qquad (5.1)$$

In our study we have taken into account the electron-phonon coupling rate, thus we have added the 1/(tcoupling)ρ to the equation

$$\frac{\partial \rho}{\partial t} = \sigma I^k + \alpha_c I \rho - \eta_{rec} \rho^2 - \eta_{diff} \rho + \eta_{(\text{coupling})} \rho \qquad (5.2)$$

In our materials the number of photons k=2

P= σ I^k is the rate of free electron generation per unit volume and unit time in multi-photon ionization, where σ is the two-photon ionization coefficient, and k=2 for two-photon absorption is given by:(Kennedy, 1995; Keldysh, 1965)

$$\sigma = \frac{2w}{9\pi}\left(\frac{mw}{h}\right)^{3/2}\left(\frac{e^2}{16w^2 c\varepsilon_0 n_0 m\, Eg}\right)^k \exp(2K).\,\Phi\left(2\mathrm{K} - 2\frac{\mathrm{Eg}}{\mathrm{hw}}\right)^{1/2} \qquad (5.3)$$

5.2 Avalanche ionization by free electron collision

This step is the electron plasma generation by avalanche ionization. The material changes its optical properties from dielectric to plasma.

When free electrons are accelerated by the laser electric field, they can generate cascade free electrons by collision excitation of bond electrons and the rate of free electrons generated per unit volume per and unit time in avalanche ionization is : $\mathbf{B=\alpha_c I \rho}$, where $\boldsymbol{\alpha_c}$ is the avalanche ionization coefficients given by:

$$\alpha c = \frac{1}{w^2\zeta^2+1}\frac{e^2\zeta}{cn0\mathcal{E}0meEg} \tag{5.4}$$

We have calculated the MPI coefficient σ, and the cascade ionization coefficient α_c for the three materials, and the results are shown in the table 5.1and we have find that the three types of materials have similar coefficients.

mateeriel	Band gap energy (eV)	Photon energy ev	K number of photons	σ (MPI coefficient) [$cm^{-3}.ps^{-1}$.$(cm^2/TW)^2$]	α_c(cascade ionization coefficient)[cm^2 /Tw .ps]
thermoplastic	3.44	2.3	2	7X 10^{20}	19.3
Borosilicate D263	3.7	2.3	2	4.8X 10^{20}	18
BK7	4.28	2.3	2	20 X 10^{20}	8.9

Table 5. 1 the calculated values of MPI and cascade -ionization coefficient for the three materials used in this study

5.3 Evaluation of E-e Recombination and diffusion effect

The recombination dynamics of laser-induced free-electrons in glass depends on the elEectron lifetime tr which depends on the electron density, $tr = 1/\eta_{rec}\rho$, The two-body recombination coefficient in glass doesn't measured, it has taken as μ_{rec}=1x10^{-10}cm^3/s from(Mingying Sun, 2012)

The diffusion rate per electron explains the decrease in the electron density in the focal volume by diffusion. The diffusion coefficient is given by:(Kennedy, 1995)

$$\eta_{diff} = \frac{\zeta E_{av}}{3m} k\left(\left(\frac{2.4}{W_0}\right)^2 + \left(\frac{1}{Z_R}\right)^2\right) \quad (5.5)$$

Where, $E_{av} = \frac{5}{4} Eg$ is the average free electron energy and ZR is the Rayleigh length of laser beam. We have calculated the diffusion for BK7 glass ηdiff = 16.3E-3 (ps^-1)

We have taken the electron phonon coupling time is t (coupling) =3.5 ps

5.4 Dynamics of free electron density during the pulse duration

At the beginning we have calculated the temporal of free electron density during the pulse width in BK7 glass at different laser intensities without taking into account the diffusion, recombination and coupling effects. The results are plotted in the figure 5.1

Where the laser intensity at the pulse duration (FWHM) is given by :

$$I(t) = I_0 \exp\left(-4ln2 \frac{t^2}{tp^2}\right) \quad (5.6)$$

tp is the pulse duration= 400 ps . We can see from the figure 5.1 that the avalanche ionization at the critical density $\rho_{crit} = w^2 m_e \varepsilon_0 / e^2$ =1.9E21 (plasma generation) happens at low intensity (0.002TW/cm²) in the middle of the pulse duration

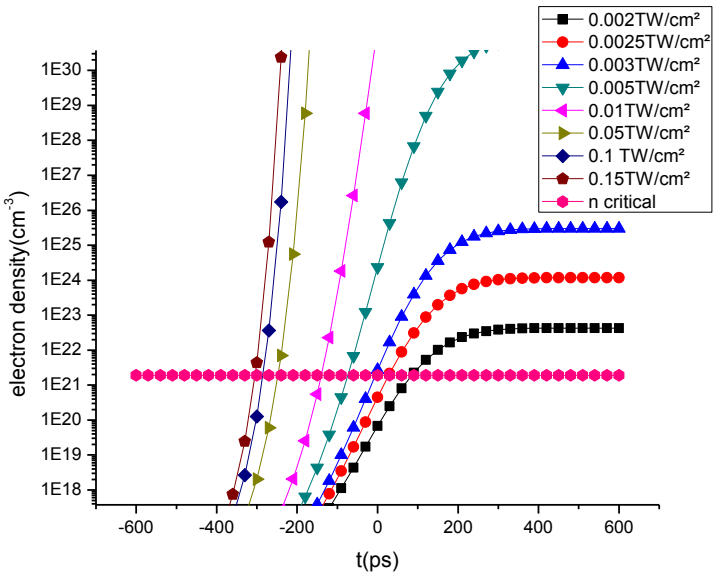

figure5. 1 the temporal evolution of free electrons density in BK7 at tp= 400Ps, and at different laser intensities and negligible recombination, diffusion and coupling rate.

We have plotted the results of free electron density using the generic form with taking into account the diffusion and recombination rate in the figure 5.2. From this figure we have found that the threshold of plasma generation is 0.03TW/cm², we find that the intensity required to induce the avalanche ionization is 15 time bigger than that without taking into account the recombination and diffusion rates.

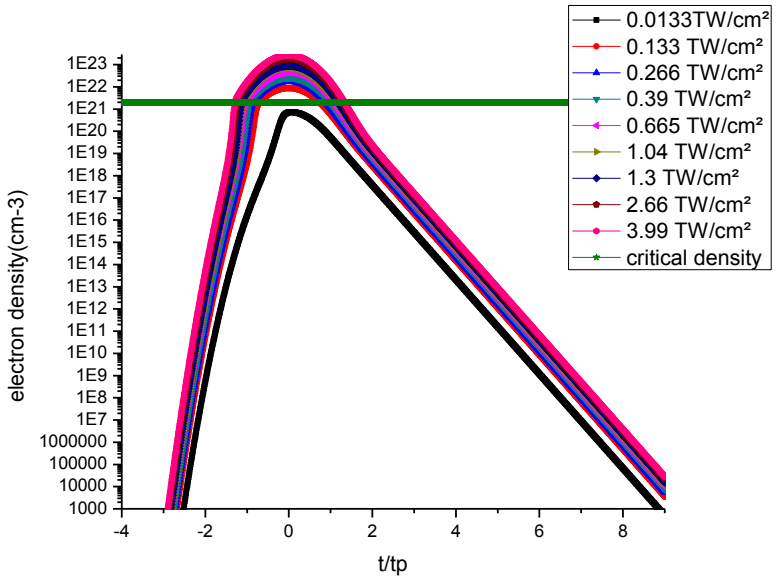

figure5. 2 the temporal evolution of free electrons density in BK7 at tp= 400Ps, and at different laser intensities with taking into account the recombination, diffusion rate .

In our study the pulse duration is long, therefore we have added a term to the generic equation which explain the decrease of the electron density caused by the electron – phonon coupling. We have assumed that the electron –phonon coupling time is 4.3ps (as in the soda lime glass) (Mingying Sun, 2012) . The results of the free electron density with adding the electron phonon coupling rate are plotted in the figure 5.3 From this figure ,we find the first intensity that lead to avalanche and electron plasma generation is 0.08TW/cm²which is 6 times more than that without taking into account the electron-photon coupling time .From this figure we find that at low intensities we have only multi-photon ionization and the electron density doesn't reached the critical electron density ionization that occurs when the plasma oscillation frequency equals to the laser frequency $\rho_{cri} = w^2 m_e \mathcal{E}_0 / e^2$ = 1.9E21cm-3, At 0.08 TW/ cm² the electron density reaches the critical electron density for avalanche ionization at this value the optical property change from transparent dielectric to plasma absorption , and at high densities the electron

density reaches the critical density at the beginning of pulse the max electron density almost the same (of 1E22 to 1E23)

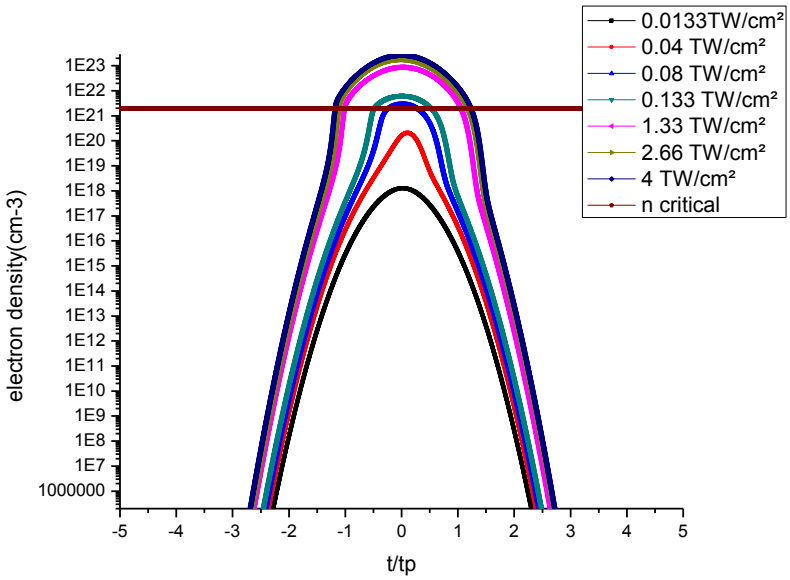

figure5. 3 the temporal evolution of free electrons density in BK7 at tp= 400Ps, and at different laser intensities with taking into account the recombination, diffusion rate

5.5 Calculation of absorbed energy and volume by the electron plasma

For calculate the absorbed energy, we calculate the optical properties of electron plasma (absorption length and the reflection) for different electron density.

5.5.1 Absorption Coefficient and Absorption Depth in Plasma

When the ionization is completed early in the puls, the formed plasma in the focal volume will has a free-elecrns density of about $10^{22}cm^{-3}$comparable to the ion density (Juodkazis, 2006). In this case the interaction with the plasma occurs in the remaining part of pulse duration. The dielectrics function of plasma has been described in the Drude approximation when the ions are considered as a neutralizing background (L.D. Landau and E.M. Lifshitz, 1984)

$$\mathcal{E} = 1 - \frac{{w_p}^2}{w^2+{v_{eff}}^2} + i\,\frac{{w_p}^2}{w^2+{v_{eff}}^2}\frac{v_{eff}}{w} = \mathcal{E}' + \mathcal{E}'' \tag{5.7}$$

W_p is the electron frequency plasma, ${w_p}^2 = \frac{4\pi e^2 n_e}{m*}$, m* is the electron effective mass, we can estimate that the optical parameters of the plasma ,assuming that the effective collision frequency v_{eff} is approximately equal to the plasma frequency wp

$$\mathcal{E}' = \frac{w^2}{w^2+{wp}^2},\ \mathcal{E}'' = \frac{wp}{w}\left(1+\frac{w^2}{{wp}^2}\right)-1 \tag{5.8}$$

We have plotted the $\mathcal{E}$' and $\mathcal{E}$'' en function of the electron free density in the figures 5.4, and 5.5

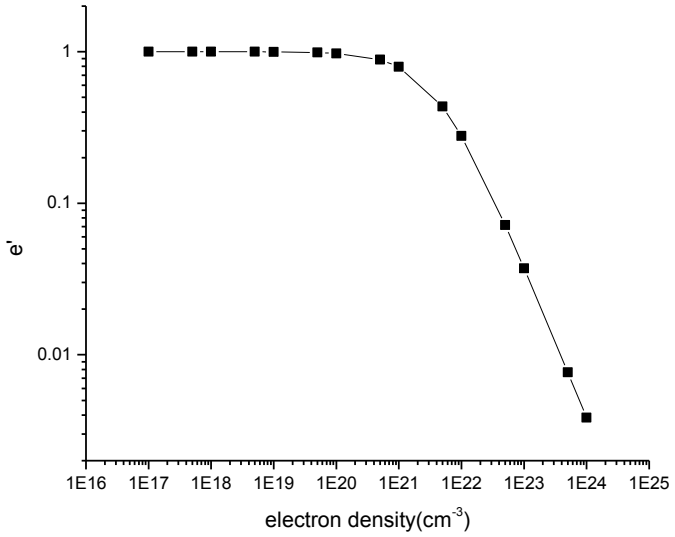

figure5. 4 $\mathcal{E}$' en function of the free electron density

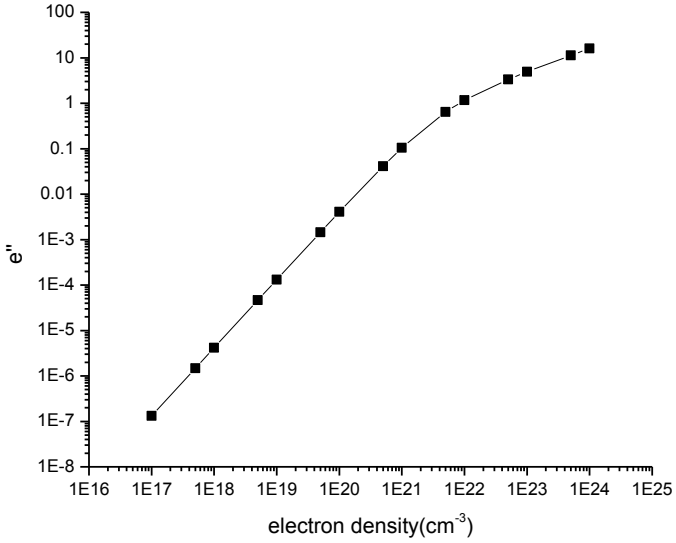

figure5. 5 $\mathcal{E}$'' en function of the free electron density

$1 = A + R + T$ Where A is the absorption, R is the reflection, and T is the transmission.

$$R = \frac{(n-1)^2+K^2}{(n+1)^2+K^2} \tag{5.9}$$

And $T = \exp\left(-\frac{z}{ls}\right)$ (5.10)

where ls is the effective optical penetration depth

$$k = \sqrt{\frac{\sqrt{\mathcal{E}'^2+\mathcal{E}''^2}-\mathcal{E}'}{2}} \quad \text{and} \quad n = \sqrt{\frac{\sqrt{\mathcal{E}'^2+\mathcal{E}''^2}+\mathcal{E}'}{2}} \tag{5.11}$$

Using the last equation we have plotted the absorption and reflection en function of the free electron density in the figures 5.6, and 5.7.

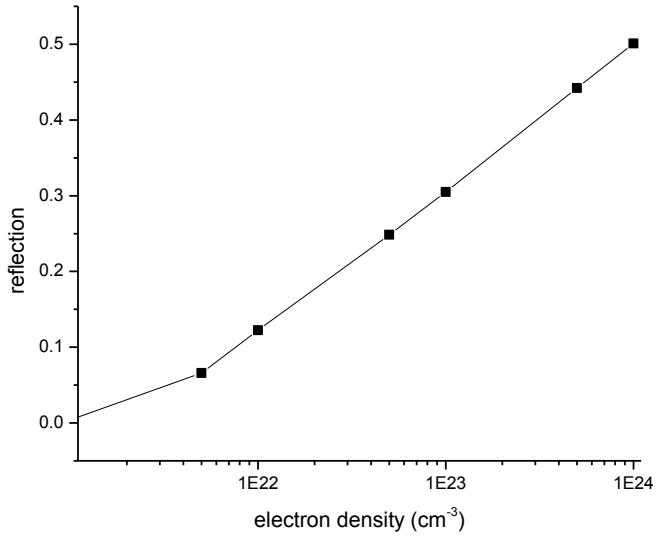

figure5. 6 The reflection in plasma en function of the free electron density

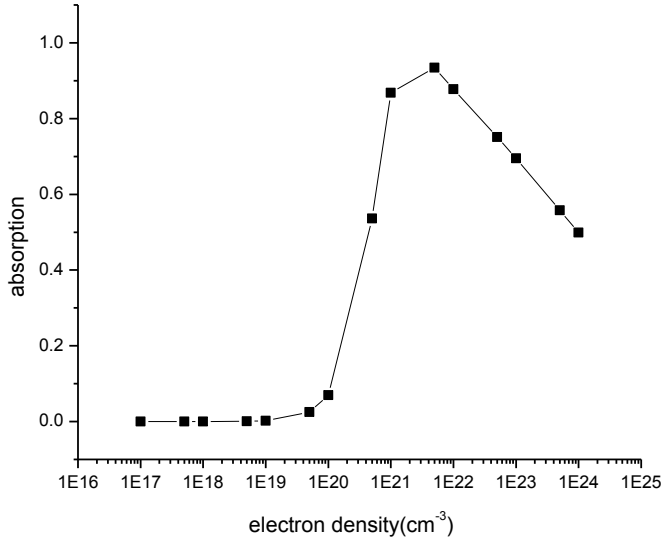

figure5. 7 the absorption in the plasma en function of the free electron density.

From the figure 5.7, we can see that the absorption starts at the free electron density of 1E20 cm^{-3} and very rapid until the max value at 5E21cm^{-3}, then it decreases. We have also l_s penetration depth in plotted the effective optical penetration depth in the plasma as the following in the figure 5.8

Where $ls = \frac{C}{WK}$ where c is the speed of light, and w is the laser frequency

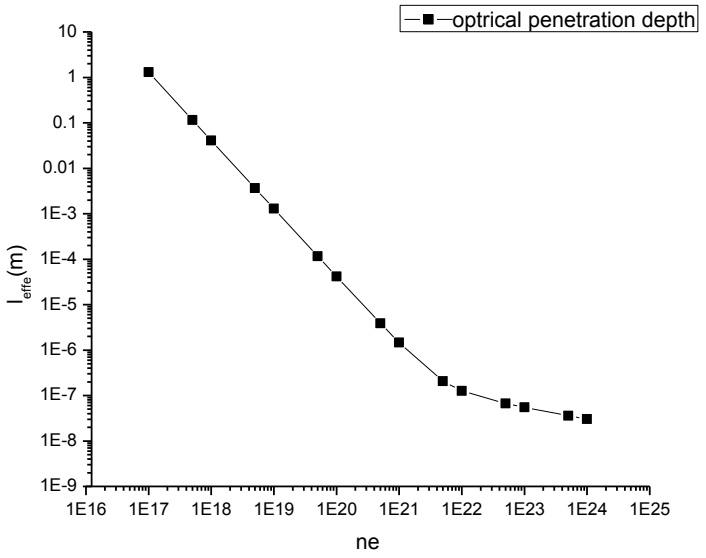

figure5. 8 the effective optical penetration depth en function of the free electron density

From the figure 5.8 we can see that, at the critical density of electrons of plasma formation, the optical penetration depth is ls= 0.35µm

5.6 Calculation of absorbed volume and energy by the electron plasma

In the next we have calculated the absorption volume in the plasma and the absorbed energy at different laser intensities. For a Gaussian beam the effective focalization surface is given by: ½ π w_0^2, thus the absorption volume is a cylindrical volume defined by the effective surface * the effective optical penetration depth L_s of the laser in the material, the absorption volume can be given as:

V absorption = ½πw_0^2 x L_s = 0.21x0.35= 0.076 µm^3

We have calculated the absorbed energy using the free-electron density calculated previously as a function of intensity and time-interval of avalanche ionization.

5.6.1 Absorbed laser energy for the theoretical threshold of plasma formation in BK7 glass

The absorbed energy at the laser intensity of 0.08 TW/cm² is showed in the figure 5.9.

From this figure we can note that the avalanche doesn't start at the beginning of the pulse, and the absorption coefficient at the max electron density is 90% of the absorbed energy by the electrons between (t=-100 and t= +127) = 13.7 J/cm² which is 30% of the incident energy. When we take into account the absorbtion coefficient 0.90% at the electron density of 2.6 E21 cm-3, the absorbed energy in the plasma is 0.90µ*13.7 = 12.28J/cm² which correspond the absorbed energy of 0.027µJ.

We can note that, at low laser intensities, the absorbed energy in the plasma is 0.27% of the incident energy.

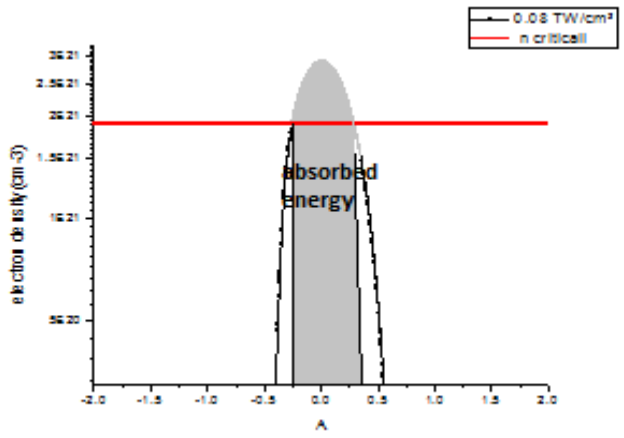

figure5. 9 the absorbed energy at 0.08 TW/cm²

5.6.2 The absorbed energy at 1.33TW/cm²

The figure 5.10 shows the absorbed energy at the high laser intensities. it is clear from the figure 5.10 that the avalanche ionization starts at beginning of the laser pulse ,that means that almost 95% of the incident energy is absorbed by the electron ,and at the electron density of 2E23 cm-3

the absorption coefficient in the plasma is 70% of absorbed energy by the electron , thus at 1.33TW/cm² the absorbed energy is $F_{(absorbed)}$ = 0.70* 558= 390 J/cm² which correspond to the absorbed energy E=0.838µJ

We can note that, at high laser intensities the absorbed energy is almost 0.665 of the incident energy. These results have good agreements with the numerical simulation in(F. Vidal, 2001)(Adela Ben-Yakar and Robert L. Byer Anthony Harkin, 2003). When 100ps pulsed laser have been irradiated on an aluminum sample ,about 70% of absorbed energy is used to expanding plasma, about 20% of absorbed energy is loss in radiation and it remains only 10% for heating the target.

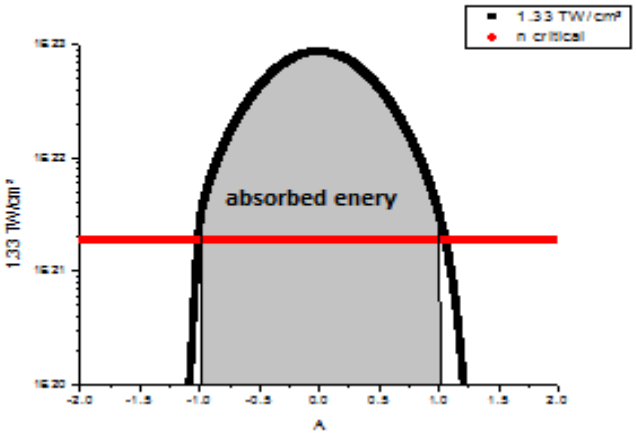

figure5. 10 the absorbed energy at 1.33 TW/cm².

In the result we can say that at low intensities<= 0.1 TW/cm² the absorbed energy in the plasma in BK7 glass is almost 0.27% of the incident energy , and at high energies > 0.1 TW/cm² the absorbed energy in the plasma is 0.665% of the incident energy.

5.7 Threshold of laser ablation

Laser ablation in transparent materials occurs when the fluence is higher than a certain value at a given pulse width. In 1995 Stuart et al (B.C. Stuart, 1995) have reported the damage thresholds of fused silica and calcium fluoride at 526, and 1053 nm for pulse duration ranging from 270 fs to 1ns, the results show that the damage threshold continues to decrease with decreasing the pulse duration , and they show that for pulse duration of few tens of picoseconds, the damage occurs via the heating of the conduction- band electrons by the incident laser and transfer this energy to lattice, this model predicts dependence of the threshold damage fluence a $\zeta^{1/2}$, whereas for the pulse width below 10Ps, the optical breakdown is a non thermal process and there is a strong deviation from the $\zeta^{1/2}$ scaling of fluence threshold in these materials.

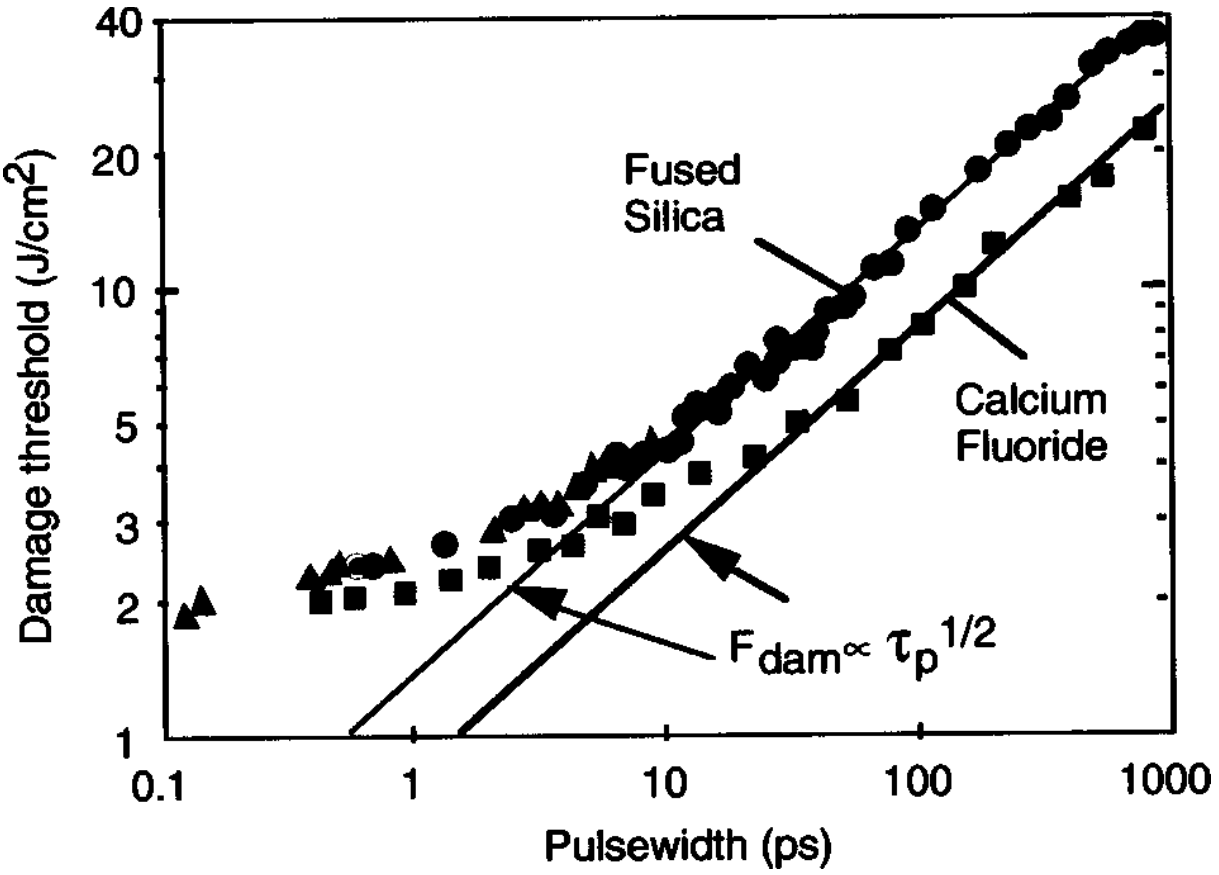

figure 2.7the damage threshold for fused silica at 1053 nm and calcium fluoride at 532nm (B.C. Stuart, 1995)

5.7.1 The experimental results for the ablation threshold and the intensity threshold of plasma generation

We have reported our results for the three materials in the table 5.2, the results show a different in the value of W_0 measured of the ablation model and the value of W calculated from the psf lab, we can explain this because of the thermal effects, this factor W (experimental)/ $W_{0(psf\ lab)}$is of 2 for the BK7, 3 for the borosilicate, and 6 for the thermoplastic. Thus , we have calculated the intensity threshold using the value of the Psf lab of our results the thermal effects in thermoplastic and the borosilicate glass D263 are more evident of that in the BK7 glass which

have the smallest factor, from these results,. In our results we have found that the threshold ablation from the depth is less than that from the D², and we have also find that the same effective optical penetration depth in BK7 and D263 borosilicate glass, and equal 1.65 of the theoretical value.

material	Borosilicate D263	BK7	thermoplastic
W_0 (psf lab)µm	0.5	0.5	0.6
Et_h of D² µJ	0.80	1.07	0.5
LS (experiment)µm	0.58	0.57	
Ls (theory)	0.35	0.35	
Ith(plasma formation) TW/cm²	0.08	0.08	0.08
Ith(complete ionization at ne= 2E22cm^{-3} TW/cm²	0.37	0.37	0.37
I_{th} *from D² TW/cm²*	0.57	0.6	0.5

Table 5. 2 the results of ablation thresholds for the three materials

Using the last results for the absorbed energy, we find that, at the intensity threshold of BK7 glass from D² (0.5 TW/cm²), The intensity for plasma formation at the electron density of 1.9E21cm^{-3} is 0.08 TW/cm² , but for having a complete ionization the electron density must reach to E22 cm-3 comparable to ion density and from the figure 5.3, we find that at the electrons density of 3E22 cm^{-3}, the incident laser intensity is 0.4 TW/ cm² which almost corresponds to the our experimental ablation threshold intensity (0.5TW/cm²).

In comparison to our result of threshold of laser ablation in BK7 glass, we find that the ablation threshold of our experiments is almost equal to the theoretical ablation thresholds.

We can conclude that the ablation in our experiments is an ablation by the plasma not by the thermal model.

For comparison our results to the results in the publications, we have find that most of publications have taken into account the ablation threshold in the femtosecond laser ablation of transparent materials for example; in fused silica the threshold of ionization have been reported to be 1.2 x 10^{13} W/cm²(D. Arnold and E. Cartier, 1992). in(K. Sokolowski-Tinten, 1998) ,the plasma threshold of BK7 glass at 100fs and 620nm have been calculated as 2.8x 10^{13}W/cm². whereas, the measurement of single shot ablation threshold of boeosilicate glass with 200fs and 780 nm Ben-Yakar et al (Adela Ben-Yakara, 2004) is 2.6J/cm² which corresponds 1.3 x10^{13} W/cm², similar experiment have been reported that the breakdown thresholds when a 120 fs, 620 nm laser irradiated in MgF2, sapphire, and fused silica is in a range of (1 to 2.8) x 10^{13}W/cm². The experimental data for laser ablation infused silica at different wavelength from the references (B. C. Stuart, 1996)and (M.D.Perry, 1999) are collected in the (E. G. Gamaly, (2002)) as shown in the figure 5.1. They have been found that the threshold fluence in fused silica glass for long pulse regime from 10 ps to 1ns the can be estimated as (E. G. Gamaly, (2002)): $F_{th} = 1.29 \left[\frac{J}{cm^2}\right] x(t_p[ps])^{1/2} \pm 15\%$ (5.12)

Assuming that the number density, the binding and the ionization energy in the BK7 glass target are the same as in fused silica (E. G. Gamaly, (2002)) we can estimate the threshold fluence of laser ablation of fused silica at 400 ps from the above expression: F_{th}=22.34J/cm²±15% which correspond to the thermal ablation threshold not to the ablation with laser induced plasma.

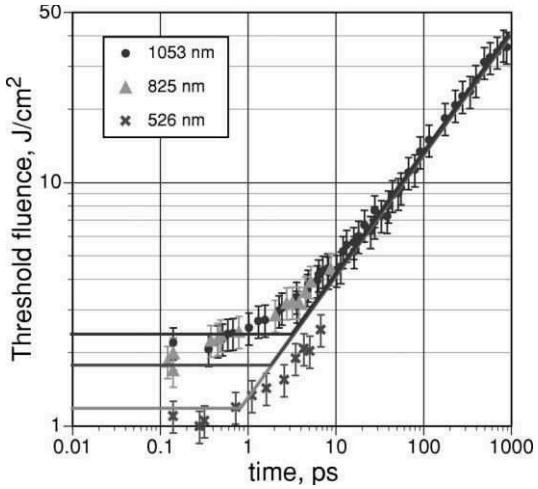

figure5. 11 Threshold laser fluence for laser ablation of fused silica versus laser pulse duration. The experimental data have taken from the refs(M.D.Perry, 1999)and (B. C. Stuart, 1996).(E. G. Gamaly, (2002))

Of the other hand ,the experiments which predicate the pulsed laser ablation of SBS thermoplastic didn't found, but we have found the ablation threshold for other thermoplastics as PMMA and Pc in (David Go´mez, 2006),in this ref, they have reported the single pulse laser threshold of PC and PMMA, with 400nm wavelength and 90 Fs, they have found that the threshold fluence is 0.20 ± 0.02 and 0.57 ± 0.04 J/cm², respectively which correspond to the intensity of 2.2 to 5.5 TW/cm² respectively .In other publication(J. Krüger, 2005), the single pulse ablation threshold in PMMA at 780nm wavelength,1KHz, and 30 fs ,and at 1064 nm,10Hz of repetition rate, and 6ns, have been found as 0.9/cm² and 0.1 respectively, which corresponds to the intensity of 3x 10^{13} and 0.03x 10^{12} respectively. From these studies we can see the effects of pulse duration, material properties, and wavelength in the ablation threshold, in our experiments; we have 400 ps and 0.5 TW/cm² which is between the two values .

5.8 Electron Temperature and Pressure

In hot plasma, the electron-to-ion energy transfer time and the heat conduction time is in a range of picoseconds (Juodkazis, 2006). Therefore, for our pulse duration of 400ps the electrons will

transport their energy to ions during the pulse energy thus Te=Ti, but in the femtosecond range of pulse duration the ion remains cold, the max electron temperature at the end of pulse can be estimated by:

$$T_e = \frac{AFP}{labs\ ce\ ne}, \tag{5.13}$$

where C_e=3/2 for ideal plasma, $n_e \approx 7 \times 10^{22}$ cm^{-3}, l_s=0.35µm, A=0.65, E (p) = 0.8 µJ/pulse (the energy threshold in laser ablation of BK7 glass),T_e =410eV= 492.753x10^4Kwhich correspond to the thermal pressure $P_e = n_e T_e$= 47.60Mbar= 4.76x10^{12} pa =4760Gp ›› 72Gp (young module),and the value of electron temperature is bigger than the energy band gap 4eVand ionization potential 13.6EV, which is an additional energy that the electron must have to drag the ion out of the target.

From the simple form of energy conservation law the electron temperature due to absorption in skin layer can be taking the next equation:(Tikhonchuk, 1988)

$$T_e = \frac{AFP}{labs\ ce\ ne} \exp(-\frac{2z}{labs}) \tag{5.14}$$

we have plotted the temperature in plasma at different incident energy en function of depth using the last equation .for ablation the dielectrics materials, the electron temperature must exceeds the energy band gap $\mathcal{E}$b+ the ionization potential Ji,

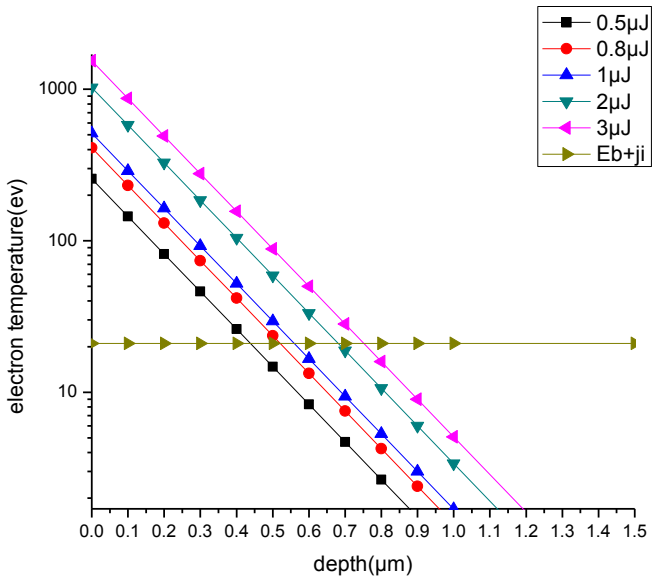

figure5. 12 the temperature in plasma at different incident pulse laser energies

From the figure 5.12 at the electron temperature above to $\mathcal{E}$b+Ji , we have different depths from to 0.45 to 0.8 μm at different pulsed laser energies , which have accords with ours experimental results

5.9 Electron-to-ion Energy Transfer

In hot plasma the electrons to ion energy exchangeven is expressed in accordance with landau(L.D. Landau and E.M. Lifshitz, 1984) as $ven = \frac{me}{mi}\ vei$:, where vei is the electron- ion collision rate in ideal plasm $vei = 3x10 - 6\ ln\Lambda\frac{neZ}{Tev3/2}$. Here Z is the ion charge and lnΛ is the coulomb logarithm.

AT the incident energy of 0.8μJ, Te=410 eV, n_e=7x10^{22}cm-^{3} lnΛ=3.7, Z=1,(mi)a=20 .the time of energy transfer from electron to ion in plasma is $t_{en}=(v_{en})^{-1}$ = 450 picoseconds which is longer than the pulse duration 400ps.Thus the electron have no time to transfer its energy to ion during the laser pulse duration, which means that the density of target doesn't change during the laser

pulse duration. Hydrodynamics motions from focal volume to surrounding materials start after the energy transfer to ions.

The three following processes are responsible for the energy transfer from electrons to ions 1)recombination, electron-to-ion energy transfer in Coulomb collisions,2) ion acceleration in the field of charge separation gradient of electronic pressure, and 3)electronic heat conduction.

5.9.1. Electron-to-ion energy transfer by Coulomb collisions

TheCoulomb force dominate the interaction between plasma particles, we can characterize the plasma state by the parameter number of the Debye sphere ND (1988) :

$$ND = 1.7x10^{9}\left(\frac{Te^{3}}{ne}\right)^{1/2} \quad (5.16)$$

If ND>> 1 the coulomb terms can be neglected, using the last estimation we find that , at the incident energy of 0.8µJ, the max electron temperature is 410 eV , ne =210^{22}, and ND≈54 >>1

5.9.2. Ion acceleration by the gradient of the electron pressure

Assuming that the energy transfer from electrons to the cold ions due to the action of electronic pressure

$$pe = ne\,Te \quad (5.17)$$

The Newton equation for ions as following:

$$\frac{\partial(m_i n_i u_i)}{\partial t} \approx -\nabla Pe \quad (5.18)$$

$$Zni = ne \quad (5.19)$$

The kinetic velocity of ions is:

$$Ui \approx \frac{ZTet}{m_i\, l_{abs}} \quad (5.20)$$

For defined the time for the energy transfer from electron to ions the ions kinetic energy must be comparable to the electron density , $\frac{1}{2} mi\ ui^2 \sim Te$ (5.21)

From the last equation, we can obtain the energy transfer time as:

$telst \sim \frac{labs}{Z}\left(\frac{2mi}{Te}\right)^{1/2}$ (5.22)

Generally this time is in order of a few ps

5.9.3 Electronic Heat Conduction and shock wave formation:

After energy transfer to ions, a heat wave will propagate outside the heated zone before the emerging of shock wave. The cooling of heated volume of plasma is described by (Raizer, 2002)

$\frac{\delta T}{\delta r} = \frac{\delta}{\delta r} r^2 DT^n \frac{\delta T}{\delta r}$ (5.23)

D is the thermal diffusion coefficient can be defined by:

$D = \frac{l_e v_e}{3} = \frac{ve^2}{3v_{ei}}$; the cooling time can be defined as follows: $tcool = labs^2/D$ (5.24)

l_e Is the electron mean free path, ve is the velocity, and vei is collision rate. The can be expressed by the temperature at the end of laser pulse

$D = D0\left(\frac{T}{T0}\right)^{5/2}$ (5.25)

$D_0 = \left(\frac{2T_0}{3m_e\, v_{ei}(T_O)}\right)$ (5.26)

Where T, is the cooling temperature T_0 is the initial temperature for cooling, n=5/2 for ideal plasma .

D_0 at 0.8µJ and T0=410 is5.7x 10^3cm²/s,

$t_0 = w_0^2/D_0$ (5.27)

t_0e time for travel the heat wave the distance w_0 is 0.42ps , thus the shock wave leave the heat wave behind at the time of electrons transfer their energy to ions (450 PS). The temperature and heat penetration distances can be expressed in a compact form as a function of the initial temperature

$$rth = r_0(\frac{t}{to})\text{^}\frac{1}{2+3n} \tag{5.28}$$

$$T = T_0(\frac{t}{to})\text{^}\frac{3}{2+3n} \tag{5.29}$$

Taking n= 5/2 in the last equation we obtainthat the shock wave emerges at r_{shock} = 2.12 r0 whiletemperature decreases to Tshock = 0.09 T0. Correspondingly, the pressure behindthe shock equals Pe = 0.09 P0 = 4.28 Mbar = 4.28 x10^{11} Pa. This pressure considerably exceeds the cold glass modulus which is in the order of P0 ~ 10^{10} Pa. Therefore, a strong shock wave emerges, which compresses the material up to a density

$$\rho = \frac{\rho 0(\gamma+1)}{\gamma-1} = 2\gamma \tag{5.30}$$

γ Is the adiabatic constant for cold glass, in this high pressure, the material behind the shock wave front can be transformed to another phase state. Then after unloading, the shock affected material can be transformed to the final state at the normal pressure, and this final state may be having properties different from the initial state.

5.9.4 Shock wave expansion and stopping

The shock wave propagating into the material loses its energy due to dissipation, and it gradually transforms into the sound wave. The shock-affected area can be defined by the distance at which the shock stops. This distance can be estimated from the condition that the pressure behind the

shock equals the so-called cold pressure (Ya.B. Zel'dovich and Yu.P. Raizer, 2002) And can be estimated by the initial mass density and the speed of sound Cs as the flowing:

$$p_0 = \rho cs^2 \tag{5.31}$$

The distance where the shock stops, is expressed by the radius, where the shock

Initially emerges via the energy conservation condition

$$r_{stop} = r_{shock}\sqrt[3]{\frac{P_{shock}}{P0}} \tag{5.32}$$

At the condition of r_{shock}=0.78µm, and pshock=4.76x10^{12}erg cm^{-3}, P0=0.26x10^{10} erg cm^{-3}, rstop= 9.5µm for a single pulse.At this point the shock wave converts into a sound wave, which propagates further into the material without inducing any permanent changes to a solid.

5.9.5 Shock and Rarefaction Waves: Formation of Void

At high energy density, hollow or low-density regions within the focal volume have been observed (E.N. Glezer, 1996). This phenomenon can be understood from the simple reasoning. The strong spherical shock wave starts to propagate outside the center of symmetry compressing the material, at this time, behind the shock wave; a rarefaction wave propagates to the center of the sphere, creating a void. The mass conservation law can be applied to estimate the density of compressed material. The void formation inside a solid is only possible if the mass initially contained in the volume of the void was pushed out and compressed. Thus after the micro explosion the whole mass initially confined in a volume with radius r_{stop}resides in a layer in between $r_{stop}$and r_v, the radius of this void can be expressed through the compression ratio c

$c = \left(\frac{1}{1-\delta}\right)\text{^} - 1/3$and the radius of laser affected zone r_{stop}

$$rv = r_{stop}/c \tag{5.33}$$

For δ=2, r_v=7.5µm. This radius is a void size immediately after the interaction; the final void forms after the reverse phase transition and cooling.

5.10 The thermal effects in laser ablation of transparent materials:

In this study we have investigated the temperature distribution in the glass material and thermal effects in laser ablation of the three materials by the properties of these materials and by the effects of focal depth inside the material

5.10.1 The temperature distribution during the laser ablation of glass solid

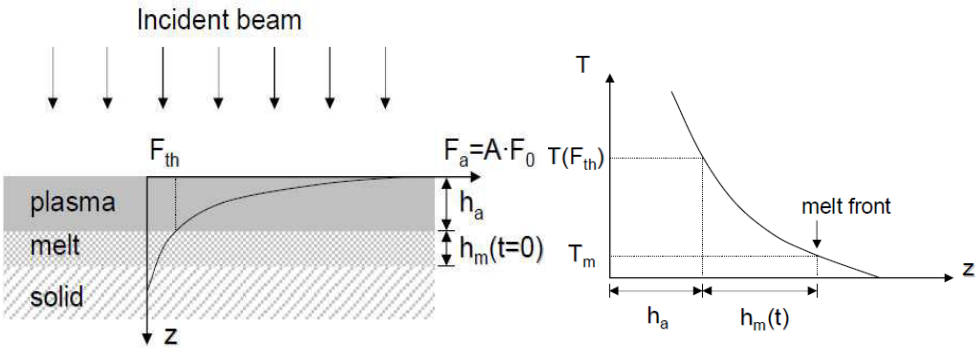

figure5. 13 the initial temperature distribution in the material

The attenuation of the absorbed laser fluence as a function of depth is given by:

$$F = A\,F_0 \exp\left(\frac{-z}{ls}\right) \qquad (5.34)$$

The figure 5.13 shows the exponential decay of the laser fluence with depth for an incident laser beam. There are three different layers for the absorption depth. 1) the ablation region with ablation depth of (h_a), in this region we have a high temperature and pressure plasma .2) The molten region below the plasma region.3) The solid region.

We have calculate the temperature distribution after the end of the pulse in the glass materialas showing in the figure 5.14, We find that at the end of pulse of 0.8µJ, the ablation depth is 0.5µm and the melting depth is 1µm.

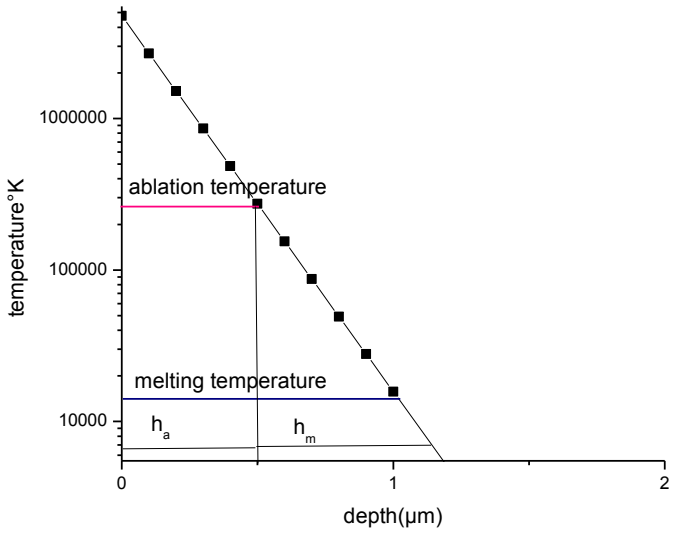

figure5. 14 Glass temperature at the end of pulse (0.8µJ).

5.10.1.1. Melting depth after heat diffusion

Taking into account the heat diffusion after the pulse duration, the initial equilibrium temperature (S. Nolte, 1997) T can then be calculated according to the optical Penetration depth l_s of the laser light and the heat penetration depth $l = \sqrt{D.t}$

$$T \approx \frac{A\,F_p}{\rho.C}\frac{1}{l^2-l_s{}^2}\left[l\exp\left(-\frac{z}{l}\right) - l_s\exp\left(-\frac{z-h}{l_s}\right)\right. \quad (5.35)$$

We have plotted the melt depth variation after different times after the pulse diration with the pulse energy of 0.8µJ as showing in the figure 5.15, we have find that After th e heat diffusion, the maximum melting depth is 70 microns before cooling (after 100 ms)

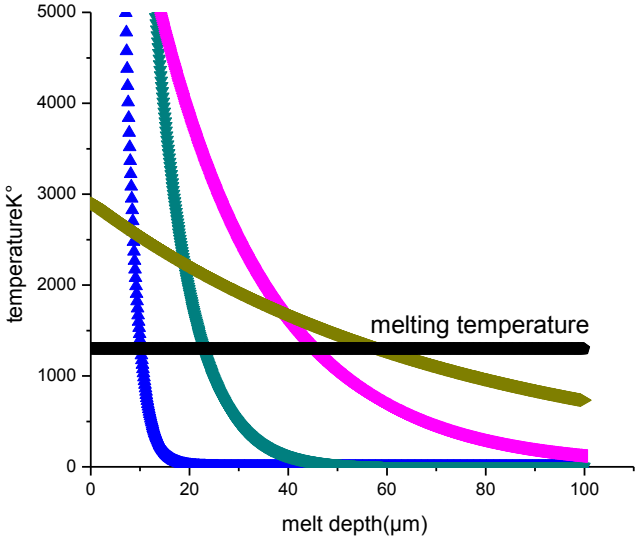

figure5. 15 the melt depth at different times(10 µs, 100 µs, 1 ms, 10 ms) after the pulse duration with taking into account the thermal diffusion.

5.10.2 Thermal effects versus material

In order to explain the thermal effects in our study, we have classified the thermal properties of the three materials in the table5.5. In our results of laser ablation of three transparent materials, we have found that the thermal effects in thermoplastic material is more evident, we can explain this because of the big thermal diffusivity in plastic materials which is about 300 times more than in the glasses materials.

Properties of materials	Borosilicate glass	BK7 glass	SBS thermoplastic
Thermal diffusivity D=K/Cρ (cm²/s)	0.0046	0.0052	1.5
$l_{het} = \sqrt{D.\tau}$ (µm)	0.017	0.012	0.2
Coefficient of thermal expansion α (20-300°C) in 10^{-6} K^{-1}	7.2	7.1	

Softening point, temperature (°C) ,	736	615	100
Young's modulus KN/mm²(Gpa)	72,9	82	0. 142

Table 5. 3 thermal properties of the studied materials

In other hand we have found that, the thermal diffusivity of the D263 borosilicate glass and BK7 glass are almost the same, whereas the thermal effects in the D263 borosilicate glass are clearer, as shown in the figure 5.16,we can also see the rim formation on the surface of D263 borosilicate glass as shown in the figure 5. 16 And 5.17, we can observe also the crater of D 263 is deeper than of BK7 at the same laser energy and the same focus conditions.

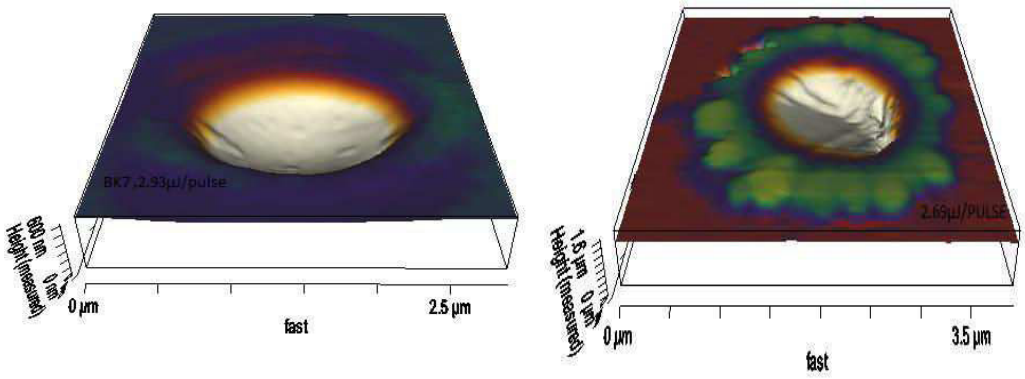

figure5. 163D image of ablated crater on each D263 borosilicate glass and BK7 glass at 2.93 µJ/pulse

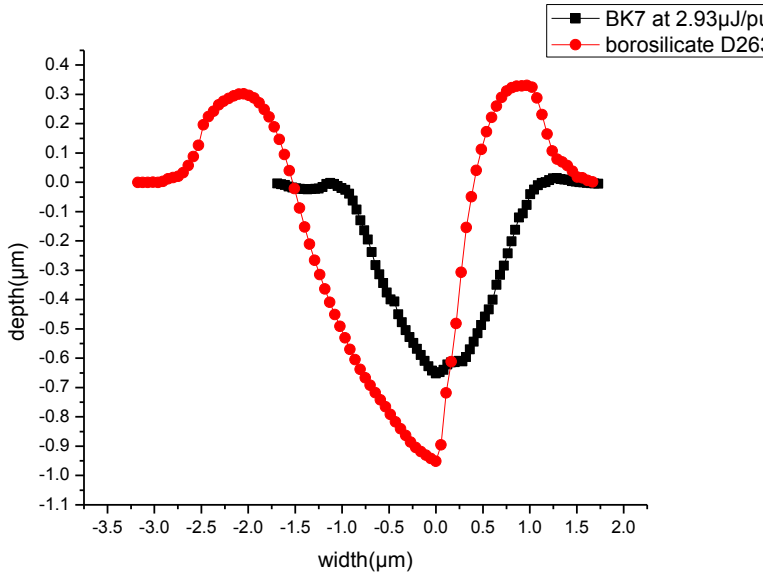

figure5. 17 Quantitative evaluation of single-shot laser ablated craters (using an atomic force microscope) for the BK7 and D263 borosilicate glass at 2.93 µJ/pulse.

We can explain these different results from the different chemical compositions of the two glasses.

The table 5.6 presents the chemical composition in the two glasses. We can see from this table the presence of AL_2O_3, TiO2, and ZnO in theD263 borosilicate glass, theses compositions present the oxide ceramics.

Composition of material	SiO_2	B_2O_3	AL_2O_3	Na_2O	K_2O	TiO_2	ZnO	Sb_2O_3	BaO
Borosilicate D263	64.1%	8.4%	4.2%	6.4%	6.9%	4.0%	5.9%	0.1%	
BK7	70%	11.5%		9.5%	7.5%				1.5%

Table 5. 4 the chemical composition of two glasses used in this thesis

The presence of the phase melting in laser ablation of AL2O3 has been achieved in (Nedialkov, et al., 2003) and the re-solidification of the melt materials leads to rime formation surround the

hole which is very clear in our experiments of laser ablation of D263 borosilicate glass, not in the Bk7 glass.

In the other hand, all the experiments of laser ablation of AL2O3 have been investigated the coulomb explosion which is an ablation mechanism alternative or additional to phase explosion. This mechanism is based on the photoemission, and the irradiated surface gains high positive charge, so the repulsive force between ions exceeds the lattice binding strength, resulting layerdisintegration.These mechanisms can be divided into two regimes (A.C. Tam, 1998; E.N. Glezer, 1995; A. Miotello and R. Kelly, 1999; K. Sokolowski-Tinten, 1999) : 1) strong ablation dominated by thermal vaporization at large laser intensities and high pulse number, where the craters areroughs and in the order of sub-micrometers, in this regime the emitted species have a similar kinetic energy and their temperature are near the vaporization temperature, and the temperature in the interface in bulk material is near the vaporization point during the ablation processes.

and 2) gentle ablation, where the craters are smooth and they are in the order of tens of nanometers, where the ions have similar momenta and they are faster than those in thermal vaporization .Stoian et al. (R. Stoian, 2006)identified that the coulomb explosion is dominated in AL2O3 by 800nm, 100fs, and at laser energy above of the threshold, where the different ions have similar momenta and high kinetic energy. At a large number of pulses, the material removal due to thermal vaporization and the different ions have similar kinetic energy as shown in the figure 5.15

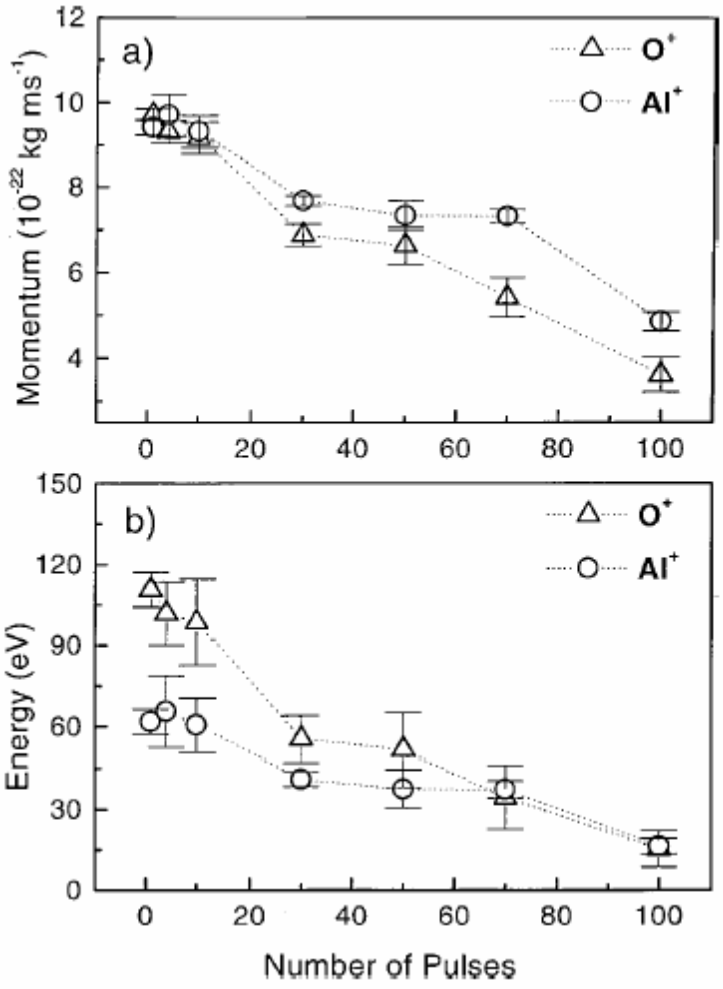

figure5. 18Momenta and energy of ions under different pulses number in AL2O3

Ladieu et al, (F. Ladieu, 2002)concluded that the thermal vaporization dominates the material removal in AL2O3 in a fluence regimes of 1-6 times of threshold by 50fs and 790 nm, and they found that the temperature is above 3000c° even at the fluence close to threshold fluence at infinitive time(several millisecond) .from these studies ,we can say that the thermal vaporization is the mechanism of laser ablation in D263 borosilicate glass and the presence of AL2O3 is the main cause of the thermal effects in D263 borosilicate glass in comparison the results of BK7 glass that doesn't has the AL2O3 in its structure .

5.10.3The thermal effects in laser ablation of transparent material versus the focal depth

In our studies we have found that, the thermal effects are more clear and evident when we have focused the laser at different focal depth in plots and lines ablated in D263 borosilicate glass as shown in the figures 5.19 and 5.20

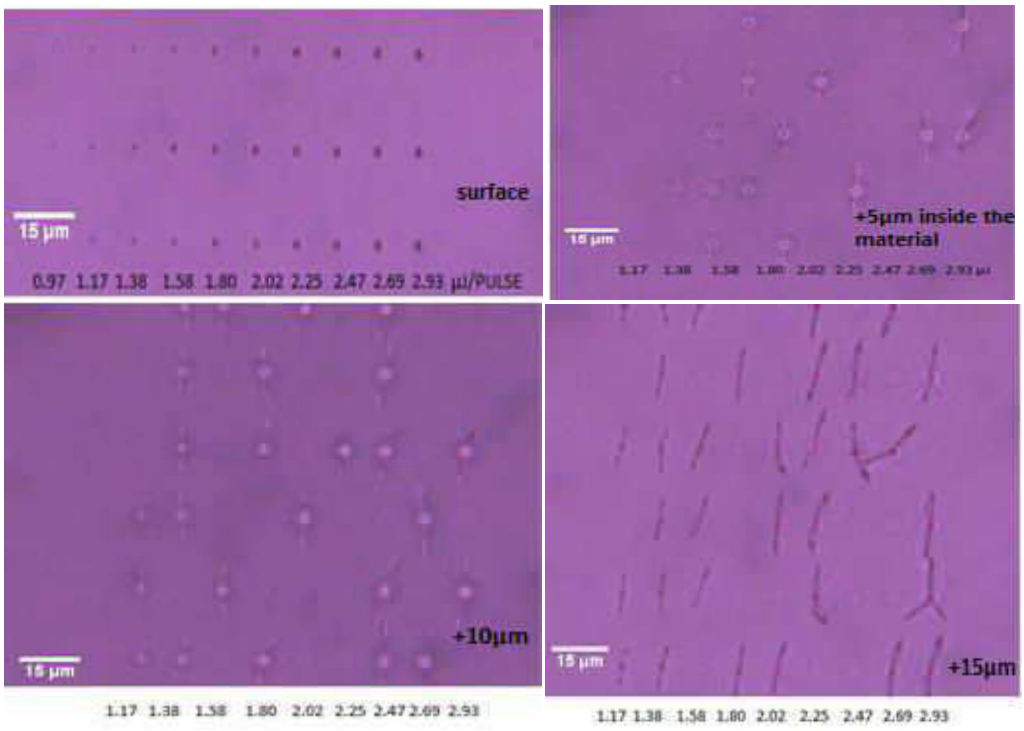

figure5. 19 the morphologies of plot fabricated on the surface of borosilicate D263 and at different focal depth(5,10,15,µm inside the material)

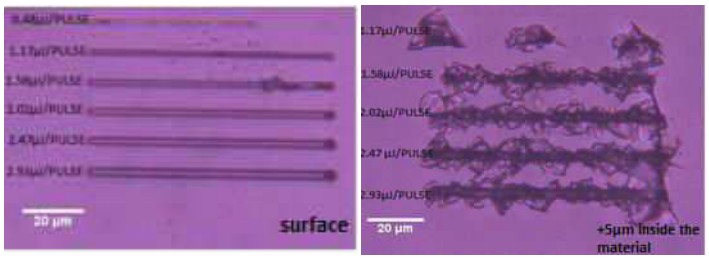

figure5. 20 lines fabricated at the point focal on the surface of borosilicate glass with one pass and at 5µm of the surface inside the glass, with an exposure time 1ms, 1 KHz repetition rate, and 0.1 µm of pulse distance

We can explain the different morphologies of ablated plots on the surface and inside the materials come from the large thermal stress induced inside the materials. There are two photomechanical stress sources which play an important role in cracking generating, the transient tensile stress produced in the heating phase and that originating from thermoplastic stress in the cooling phase of the interaction(Dyer, 2003).

5.11 Conclusion

In this chapter, the free-electron dynamics on sub nanosecond laser pulses irradiation of transparent BK7 glass have been discussed using the Kennedy approximation. We have found that the free electron generation can be affected by the recombination and diffusion effects and the electron phonon coupling coefficient,

The results of free electrons calculation using the free electron generation showed

Using the free- electron density equation we havecalculated different regime of free-electron generation for different laser intensities

- At low intensities < 0.02 TW/cm² we have only multi-photon ionization and the electron density doesn't reached the critical electron density ionization that occurs when the plasma oscillation frequency equals to the laser frequency
- At 0.08 TW/ cm² the electron density reaches the critical electron density for avalanche ionization at which the optical property change from transparent dielectric to plasma absorption
- At high densities the electron density reaches the critical density at the beginning of pulse the max electron density almost the same value of 1E22 to 1E23
- The theoretical threshold of electron plasma formation is 0.08TW/cm²

Using the Drude approximation, we have calculated the optical properties of electrons plasma (absorption length and the reflection) and the absorbed energy in plasma for different electron density, we have found that:

- At low laser intensities< 0.2 TW/cm², the absorbed energy in the plasma is 0.27% of the incident energy.
- At laser intensities> 0.2 TW/cm² the absorbed energy is almost 0.665 of the incident energy.
- The absorbed volume in plasma is $0.076\mu m^3$

Qualitative estimations of the heat and shock wave propagation, and material compression have been realized and simple hydrodynamic model used to predicate the void size at the incident laser energy of 0.8μJ:

- the max electron temperature reaches to 410 EV
- the electrons to ion energy exchange time in the plasma is 450ps> pulse duration
- the heat wave propagate outside the heated zone and travel the distance w_0 pendant 0.42PS
- shock wave emerges at $r_{shock} = 0.78\mu m$, and the shock wave converts into a sound wave, which propagates further into the material without inducing any permanent changes to a solid at rstop= 9.5μm
- This radius of a void formed immediately after the interaction is $r_v=7.5\mu m$, but the final void forms after the reverse phase transition and cooling.

The results of threshold of laser ablation from the ablation model via D² and the depth (h) of the materials have been discussed in this chapter,

- We find that there is a thermal factor that affects the crater diameters, and this factor is more evident the thermoplastic sample.
- If we assumed that the ablation is complete at the free electron density reaches to E22 cm^{-3} comparable to ion density, we find that our ablation threshold in BK7 glass (0.4TW/cm²) has a good agreement with the first laser intensity (0.5TW/cm²) that leads to generation this amount of free electrons.

The thermal effects in laser ablation of these materials versus the properties of materials and the focal depth, we find that:

- the mechanism of thermal vaporization laser ablation in D263 borosilicate glass is dominated because of the presence of AL2O3 in its structure
- The cracks generation with the laser focused inside the material is due to the thermal stress induced inside the materials.

Chapter6
General Conclusion and prospects:

In this thesis, we have investigated the microchip sub-nanosecond pulsed laser ablation of three types of transparent materials D263 borosilicate glass,BK7 glass, and SBS thermoplastic, The results show that this type of laser is capable to fabricate Sub-micron resolution embedded marking is demonstrated inside borosilicate glass. Micro fluidic channels for optical sensor are engraved on BK-7 glass with ion-doped waveguides. Arrays of dense micro channels are fabricated at the surface of thermoplastics with a zone affected by thermal effects limited to the micron range.

In this study a sub-nanosecond microchip laser has been focused on the surface of transparent material into a focal volume of $1.37\mu m^3$. during the laser matter interaction, the transparent material convert into plasma by the action of multi-photon absorption and avalanche ionization, which lead to strong laser absorption and high concentration of energy in the absorption volume of $0.076\mu m^3$. When the pressure in the absorption volume is higher than the strengths in the material, a strong expanding shock wave will generate to compress the material surrounding the absorption volume resulting in the micrometer-sized void formation in the material

We have predicated the steps of laser-induced plasma ablation of transparent materials:

1) Free-electron generation by two-photon laser absorption
2) Weak free-electron absorption and avalanche ionization
3) Electron plasma generation and 30% laser reflection, and strong laser absorption
4) Energy transfert to ions by e-p coupling (3 ps) during the pulse duration
5) Ion plasma generation ($T°=10^6$ °K, P=4 Gpa) and explosion

6) Heat diffusion and melting zone

7) Crater cooling and resolidification

The residual thermal effects affects in laser ablation of the three materials have been studied, we find that:

- Residual heat comes from the absorption gradient outside of the plasma region (micron size during pulse duration)
- Only a few % of input energy, proportional to pulse duration
- Melting region up to tens of microns during 100 ms before resolidification , thus the line ablation have been effected in the molten material
- Near threshold: small effects (X2 size with glass, X5 size with thermal plastics)

The thermal effects in laser ablation of three materials versus the material properties and the focal depth have been studied:

- Mechanisms of strong ablation with thermal vaporization due to the presence of AL2O3 in the structure of D263 borosilicate glass have been found.
- The processing parameters to fabricate good structure without thermal effect in the SBS thermoplastics can be controlled by increasing the time between the pulses to 0.5s and the distance between the structures until 8µm.
- The cracks generation with the laser focused inside the material is due to the thermal stress induced inside the materials

In prospects , we will study the laser ablation with a new laser which is fabricated par team photonics, this new laser give more pulse energy, larger laser spot -> 5 microns, and we can do Parallel fabrication with 100 laser spots at the same time

figure 7. 1 New PicoSpark laser: 100 µJ at 500 kHz and 550 psececond

In the other hand we will study another laser which is developed in laboratory LIPHY with shorter pulse duration (100ps). This laser generate higher peak powers and 4 times lower of residual thermal energy

Bibliography

[] // Appl Phys Lett80

[Journal].

[Online] // Micromachining Handbook, http://www.cmxr.com/Industrial/Handbook/Index.htm. - march 2010.

[Journal]. - [s.l.] : computer chem. - 3 : Vol. 21. - 129-142.

1 SteenW M (ed.) Laser material processing [Journal]. - NewYork : Springer Verlag, 1991.

A. Ben-Yakar A. Harkin, J. Ashmore, M. Shen, E. Mazur, R.L. Byer, and H.A. Stone Thermal and Fluid Process of a Thin Melt Zone during Femtosecond Laser Ablation of Glass [Journal] // SPIE . - 2003. - Vol. 335. - p. 4977.

A. Miotello and R. Kelly Laser-induced phase explosion: new physical problems when acondensed phase approaches the thermodynamic critical temperature [Journal]. - [s.l.] : Appl. Phys. A Supp, 1999. - S67-S73. : Vol. 69.

A.C. Tam H.K. Park, and C.P. Grigoropoulos, Laser cleaning of surface contaminants,. [Journal]. - [s.l.] : Appl Surf. Sci., 1998. - 721-725 : Vols. 127- 128.

A.Einstein On the quantum theory of radiation [Journal]. - 1917.

A.V. Lugovskoy and I. Bray " Ultrafast electrondynamics in metals under laser irradiation [Journal]. - [s.l.] : Phys.Rev. B, 1999. - 3279-3288 : Vol. 60.

Adela Ben-Yakar and Robert L. Byer Anthony Harkin Jacqueline Ashmore, and Howard A. Stone Mengyan Shen and Eric Mazur Morphology of Femtosecond Laser Ablated Borosilicate Glass Surfaces [Journal]. - [s.l.] : Appl. Phys. Lett. , 2003. - 3030 : Vol. 83.

Adela Ben-Yakara Robert L. Byer Femtosecond laser ablation properties of borosilicate glass [Journal]. - [s.l.] : APPLIED PHYSICS, 2004. - 9 : Vol. 96.

AMPONSAH-MANAGER KWABENA MICROCHIP LASERS AS SOURCES FOR LASER-INDUCED BREAKDOWN SPECTROSCOPY: PLASMA CHARACTERISTICS AND ANALYTICAL PERFORMANCE [Report]. - [s.l.] : UNIVERSITY OF FLORIDA, 2005.

B. C. Stuart M. D. Feit, S. Herman, A. M. Rubenchik, B. W. Shore, and M. D. Perry Nanosecond-to-femtosecond laser-induced breakdown in dielectrics [Journal]. - [s.l.] : Phys. Rev. B , 1996. - 1749 : Vol. 53 .

B. C. Stuart M. D. Feit, S. Herman, A. M. Rubenchik, B. W. Shore,and M. D. Perry, Optical ablation by high power short-pulse lasers [Journal]. - [s.l.] : J. Opt. Soc. Amer. B, , 1996.. - 459-468 : Vol. 13.

b. rethfeld1 k. sokolowski-tinten, d. von der linde,s.i. anisimov Timescales in the response of materials to femtosecond laser excitation [Journal] // Appl. Phys. A . - 2004. - Vol. 79. - pp. 767-769.

B.C. Stuart M. D. Feit, A. M. Rubenchik, B.W. Shore, and M. D. Perry Laser-Induced Damage in Dielectrics with Nanosecond to Subpicosecond Pulses [Journal]. - [s.l.] : PH YS ICAL REVIEW LETTERS, 1995. - Vol. 74.

B.C. Stuart M.D. Feit, A.M. Rubenchik, B.W.Shore, and M.D. Perry, Laser-induced damagein dielectrics with nanosecond to subpicosecond pulses [Journal]. - [s.l.] : Phys. Rev. Lett., 1995. - 2248- 2251 : Vol. 74.

Bauerle D laser processing and chemistry [Journal]. - berlin : spring, 1996.

Buerhop B. Blumenthal, R. Weissmann, N. Lutz, and S. Biermann, Glass surface treatment with excimer and CO2 lasers [Journal]. - [s.l.] : Appl. Surf. Sci, 1990. - 430–434 : Vol. 46.

C. B. Schaffer A. Brodeur, and E. Mazur, laser-induced breakdown and damage in bulk transparent materials induced by tightly focused femtosecond laser pulses [Journal] // meas.Sci. Technol. - 2001. - Vol. 12. - pp. 1784- 1794.

D. Arnold and E. Cartier Theory of laserinduced free-electron heating and impact ionization in wide-band-gap solids. [Journal]. - [s.l.] : PRB 46, 1992. - 15102–15115 : Vol. 23.

D. von der Linde K. Sokolowski-Tinten, and J. Bialkowski, Lasersolid interaction in the femtosecond time [Journal] // Appl. Surf. Sci. . - 1997. - Vol. 1. - pp. 109-110.

D.Bauerle laser processing and chemistry [Journal]. - [s.l.] : spring verlag, 1996.

David Go´mez Igor Goenaga On the incubation effect on two thermoplastics when irradiated with ultrashort laser pulses: Broadening effects when machining microchannels [Journal]. - [s.l.] : Applied Surface Science , 2006. - 2230–2236 : Vol. 253.

Docchio F., Regondi, P., Capon, M. R. C., and Mellerio, J. Study of the Temporal and Spatial Dynamics of Plasmas Induced in Liquids by Nano- second Nd:YAG Laser Pulses. 1. Analysis of the Plasma Starting Times [Journal] // Appl. Opt.. - 1988. - Vols. 27, pp. - pp. 3661–3668.

DU D LIU X,KRON G,Squier J,Mourou G [Journal] // appl phy lett. - 1994. - Vol. 3071. - p. 64.

Dyer Günther Paltauf and Peter E. Photomechanical Processes and Effects in Ablation [Journal]. - [s.l.] : Chem. Rev, 2003. - 487-518 : Vol. 103.

E. G. Gamaly A. V. Rode, B. Luther-Davies, and V. T. Tikhonchuk Ablation of solids by femtosecond lasers: Ablation mechanism and ablation thresholds for metals and dielectrics [Journal]. - [s.l.] : AIP physics of plasmas, (2002). - 949 : Vol. 9.

E. G. Gamaly A. V. Rode, B. Luther-Davies, and V. T. Tikhonchuk Ablation of solids by femtosecond lasers: Ablation mechanism and ablationthresholds for metals and dielectrics [Journal]. - [s.l.] : PHYSICS OF PLASMAS, 2002. - 3 : Vol. 9.

E.N. Glezer M. Milosavljevic, L. HuangR.J. Finlay, T.-H. Her, J.P. Callan andE. Mazur, Three-dimensional optical storage inside transparent materials, [Journal]. - [s.l.] : Opt.Lett., 1996. - 2013- 2015 : Vol. 21.

E.N. Glezer Y. Siegal, L. Huang, and E. Mazur, Behavior of ?(2) during a laser-induced phasetransition in GaAs, [Journal]. - [s.l.] : Phys. Rev. B, 1995. - 9589-9596 : Vols. 51,15.

F. Ladieu P. Martin, and S. Guizard, Measuring thermal effects in femtosecond laser-induced breakdown of dielectrics [Journal]. - [s.l.] : Appl. Phys. Lett, 2002. - 957-959. : Vol. 81.

F. Vidal S. Laville, B. Le Drogoff, T. W.Johnston, M. Chaker, O. Barthélemy,J. Margot, and M. Sabsabi [Journal] // Optical Society of America. - 2001.

G. Allcock P. E. Dyer, G. Elliner and H. V. Snelling Experimental observations and analysis of CO2 laser-induced microcracking of glass [Journal]. - [s.l.] : Appl. Phys. , 1995. - 7295 : Vol. 78.

G. Herbst M. Steiner, G. Marowsky, and E.Matthias, Ablation of Si and Ge using UVfemtosecond laser pulses [Journal]. - [s.l.] : Mater. Res. Soc. Symp. Proc, 1996. - 69-74 : Vol. 397.

G. J. Dixon L. S. Lingvay, and R. H. Jarman, Properties of close coupled monolithic, lithium neodymium,tetraphosphate lasers, [Journal]. - [s.l.] : Proc. SPIE 1104, 1989. - Vol. 107.

Ihlemann P. Simon and J. Machining of submicron structures on metals and semiconductors by ultrashort UV-lase pulses [Journal]. - [s.l.] : Appl.Phys.A, 1995. - 505-508 : Vols. 63,5.

J. Ihlemann B. Wolff, and P. Simon Nanosecond and Femtosecond Excimer Laser Ablation of Fused Silica [Journal]. - Verlag : Appl. Phys. A, 1992. - 363-368 : Vol. 54.

J. Krüger S. Martin , H. Ma¨debach , L. Urech ,T. Lippert , A. Wokaun , W. Kautek Femto- and nanosecond laser treatment of doped polymethylmethacrylate [Journal]. - [s.l.] : Applied Surface Science , 2005. - 406–411 : Vol. 247.

J.C.Miller Laser Ablation [Journal]. - Berlin : spring material science, 1994. - Vol. 28.

Jin Yu Qianli Ma, Vincent Motto-Ros, Wenqi Lei Generation and expansion of laser-induced plasma as a spectroscopic emission source [Journal] // Front. Phys.. - 2012. - Vol. 7(6). - p. 649669.

JM Liu [Journal] // opt Lett. - 1982. - Vol. 196. - p. 7.

Juodkazis Hiroaki Misawa and Saulius 3D Laser Microfabrication Principles and Applications [Book]. - [s.l.] : WILEY-VCH Verlag GmbH & Co. KGaA,, 2006.

K. Furusawa K. Takahashi, H. Kumagai, K. Midorikawa, and M. Obara, Ablation characteristics of Au, Ag, and Cu metals using a femtosecond Ti:sapphire laser [Journal]. - [s.l.] : Appl. Phys. A, 1999. - 659-366 : Vols. 69,7.

K. Sokolowski-Tinten J. Bialkowski, A. Cavalieri, M. Boing, H. Schuler, and D. von der Linde Dynamics of femtosecond laser-induced ablation from solid surfaces [Journal]. - [s.l.] : SPIE , 1998. - PP, 47 - 57 : Vols. 3343 Ed. C. Phipps, Part One,.

K. Sokolowski-Tinten J. Bialkowski, M. Boing and A. Cavalleri, D. von der Linde, Thermal and nonthermal melting of gallium arsenide afterfemtosecond laser excitation, [Journal]. - [s.l.] : Phys. Rev. B, 1999. - R11805-R11808. : Vol. 58.

Kautek Kru¨ger and W. Femtosecond-pulse visible laser processing of transparent materials [Journal]. - [s.l.] : Appl. Surf. Sc, 1996. - 96-98 : Vol. 430.

Kautek Wolfgang and Krueger Joerg Femtosecond pulse laser ablation of metallic, semiconducting, ceramic, and biological materials [Journal]. - Vienna, Austria : Proc. SPIE 2207, 1994. - Vol. 600.

Kautek. J. Kruger and W. The femtosecond pulse laser: a new tool for micromachining. [Journal] // Laser Physics. - 1999.. - Vol. 9(1). - pp. 30 - 40.

Keldysh L. V. Ionization in the field of a strong electromagnetic wave [Journal] // Phys. JETP. - 1965. - 1314 : Vol. 1307. - p. 20.

Keldysh Yu.A. Il'inski and L.V. Electromagnetic response of Material Media, [Journal]. - [s.l.] : Plenum press, 1994.

Kennedy P. K. A first-order model for computation of laser-induced breakdown thresholds in ocular and aqueous media part 1: theory [Journal]. - [s.l.] : IEEE J. Quantum electron, 1995. - 2241-2249 : Vol. 31.

Kennedy P. K. A first-order model for computation of laser-induced breakdown thresholds in ocular and aqueous media—Part I: Theory [Journal]. - [s.l.] : IEEE J. Quantum Electron., 1995. - 2241-2249 : Vol. 31.

L.D. Landau and E.M. Lifshitz Electrodynamics of Continuous Media [Book]. - [s.l.] : Pergamon Press, Oxford,, 1984.

Lenznar M krugerJ,Sartania S,Cheng Z, Spielmann C, Mourou G,Kautek W,Krausz F [Journal] // Phys Rev Lett. - 1998. - Vol. 353. - p. 80.

Longtin C. H. Fan.J. Sun.J. P. Plasma Absorption of Femtosecond Laser Pulses in Dielectrics [Journal] // Journal of Heat Transfer. - 2002. - Vol. 124. - pp. 275- 283.

M. Lenzner J. Krüger, W.Kautek, F. Krausz Precision laser ablation of dielectrics in the 10-fs regime [Journal]. - [s.l.] : Appl Phys A, (1999) . - 369 : Vol. 68.

M.D.Perry B.C.Stuart,P.S.Banks,M.D.Feit, V. Yanovsky,and A.M. Rubenchik Ultrashort-pulse laser machining of dielectric materials [Journal] // Appl.Phys. - 1999. - Vol. 6803. - p. 85.

Maiman T. H. Stimulated optical radiation in ruby. [Journal]. - London : Nature, , 1960. - Vols. 187: 493, .

MANNA J DUTTA MAJUDAMAR and I laser processing of materials [Journal]. - india : Sadhana, 2003. - Vol. 28. - part 3 and 4.

Mingying Sun Urs Eppeltb, Simone Russe, Claudia Hartmannb,Christof Siebertf, Jianqiang Zhua, Wolfgang Schulz, Laser ablation mechanism of transparent dielectrics with picosecond laser pulses [Journal]. - [s.l.] : SPIE , Laser-Induced Damage in Optical Materials, 2012. - Vols. 8530 853007-1.

Molva Engin Microchip lasers and their applications in optical microsystems [Journal]. - [s.l.] : Optical Materials , 1999. - 289-299 : Vol. 11.

Mooradian J. J. Zayhowski and A. Frequency-modulated Nd:YAG microchip lasers [Journal]. - [s.l.] : OPTICS LETTERS , 1989. - 12 : Vol. 14.

N Bloembergen [Journal] // IEEE J QUANT Electron. - Vol. 10:375. - p. 1974.

Nahen K., and Vogel, A. Plasma Formation in Water by Picosecond and Nanosecond Nd:YAG Laser Pulses—Part II: Transmission, Scattering, and reflection [Journal] // IEEE J. Sel. Top. Quantum Electron.. - 1996. - pp. pp. 861–871..

Nedialkov Nikolay N. [et al.] Ablation of ceramics with ultraviolet, visible and infrared nanosecond laser pulse [Conference]. - [s.l.] : Proc. SPIE 5120, XIV International Symposium on Gas Flow, Chemical Lasers, and High-Power Lasers, , 2003. - doi:10.1117/12.515847.

P.S. Banks M.D. Feit, A.M. Rubenchik, B.C.Sturt, and M.D.Perry Material effect in ultrashort pulse laser drilling of metal [Journal]. - [s.l.] : Appl.phys.A, 1999. - 377-380 : Vols. 69,7.

Peatman Bill All-Laser Precision Manufacturing Solutions Why a femtosecond laser is more precise [Article] // Raudiance. - 2013.

Physics of Laser Plasma Interaction [Journal]. - New York : Addison Wesley, 1988.

R. Stoian H. Varel, A. Rosenfeld, D. Ashkenasi R. Kelly, and E.E.B. Campbell, Ion time-of flight analysis of ultrashort pulsed laser-induced processing of Al2O3, [Journal]. - : Appl, SURF.Sci, 2006. - . 44-55 : Vol. 165.

R.Ladenburg research on the anomalous dispersion of gazes [Journal]. - [s.l.] : Z.phys, 1928.

Raizer Y. P. Breakdown and Heating of Gases Under the Influence of a Laser Beam [Journal] // Sov. Phys. Usp,. - 1966. - Vols. 8, pp.. - pp. 650–673..

Raizer Ya.B. Zel'dovich and Yu.P. Physics of Shock Waves and High-Temperature Hydrodynamic Phenomena, [Book]. - Dover, New york : [s.n.], 2002.

S. Nolte C. Momma, H. Jacobs, A. Tunnermann, B. N. Chichkov, B. Wellegehausen, and H. Welling, Ablation ofmetals by ultrashort laser pulsesl [Journal]. - [s.l.] : J. Opt. Soc. Am.), 1997. - 2716-2722 : Vol. B 14 (10.

S. Preuss A. Demchuk, and M. Stuke, SubpicosecondUV laser ablation of metals [Journal]. - [s.l.] : Appl.Phys ,A,, 1995,. - pp.33-37 : Vols. 61, 1, .

Satuart BC feit MD,Herman S,Rubenchik Am,Shore BW,PerryMD [Journal] // opt soc AMB. - 1996. - Vol. 459. - p. 13.

T. Schwarz- Selinger D.G. Cahill, S. C. Chen, S. J. Moon,and C.P. Grigoropoulos Micron scale modification of Si surface morphology by pulsed- laser texturing [Journal] // physical review B. - 1999. - Vol. PP 155323. - p. 64.

The effect of laser pulse duration on ICP-MS signal intensity, elemental fractionation, and detection limits in fs-LA-ICP-MS [Journal] // Nicole L. LaHaye, Sivanandan S. Harilal, Prasoon K. Diwakar and Ahmed Hassanein. - 2013.

Tikhonchuk E. G. Gamaly and V. T. [Journal]. - [s.l.] : JETP lett, 1988. - 452 : Vol. 48.

Tünnermann A. Ancona · D. Nodop · J. Limpert · S. Nolte ·A. Microdrilling of metals with an inexpensive and compactultra-short-pulse fiber amplified microchip laser [Journal]. - [s.l.] : Appl Phys A , 2009. - 19-24 : Vol. 94.

Vladimir N Tokarev , and Alexander F H Kaplan Suppression of melt flows in laser ablation: application to clean laser processing [Journal] // J. Phys. D: Appl. Phys. - 1999. - Vol. 32.

von vorgelet ultrafast dynamics of melting and ablation at large intensities [Report]. - [s.l.] : phd thesis, 2009.

X. Liu and G.Mourou laser ablation and micromachining with ultrashort laser pulse [Journal].

Y. R. Shen The Principles of Nonlinear Optics [Book]. - New York : Wiley, 1984.

Ya.B. Zel'dovich and Yu.P. Raizer Physics of Shock Waves and High-Temperature Hydrodynamic Phenomena, [Journal]. - Dover, New york : [s.n.], 2002.

Zayhowski John J. Passively Q-switched Nd:YAG microchip lasers and applications [Journal]. - [s.l.] : Journal of Alloys and Compounds , 2000. - 393-400.

: